PHOTOELASTIC TENSOR ELEMENTS OF OPTICAL GLASSES: DISPERSION AND RELATION TO STRUCTURE

by

Abby Jenkins

Submitted in partial fulfillment of the requirements
for the degree of Master of Science

at

Dalhousie University
Halifax, Nova Scotia
April 2023

© Copyright by Abby Jenkins, 2023

To my wonderful husband Shawn,

for this is another step towards our next adventure together.

...

In loving memory of Mocha.

Table of Contents

List of Tables

List of Figures

Abstract

Photoelasticity refers to the change in index of refraction of a material due to applied stress or strain, and in glass, results in birefringence. Understanding and controlling this effect is an important aspect in the design and technological application of glass. Further complicating the issue is that photoelasticity shows a complicated dispersive behaviour, which has been very little studied. In this thesis, the dispersion of the photoelastic response of a set of CDGM commercial glasses was investigated using a modified acousto-optic technique. Electron microprobe analysis paired with Raman and solid-state nuclear magnetic resonance spectroscopy proved the importance of verifying the compositional discrepancies that may occur when acquiring samples from commercial suppliers. The structural insight provided by these techniques was used to understand trends in the photoelastic data. This understanding was contextualized based on the calculated parameters of the bond polarizability model for the first time for these glasses.

Chapter 1

Introduction

Although the dispersion of the stress-optic coefficient has been previously studied in literature, focused research on measuring the dispersion of the individual photoelastic tensor elements p_{11} and p_{12} is lacking [1, 2, 3, 4]. Structural knowledge of how these elements change with composition can aid in the design of optical devices with specific photoelastic response. Some examples include but are not limited to, fiber optic cables with low p_{12} to suppresses the undesirable phenomenon of stimulated Brillouin scattering that limits signal transmission, and zero-stress optic glasses whose optical properties remain isotropic with applied stress. This thesis describes modification of the acousto-optic Dixon-Cohen method to investigate the dispersion of the photoelastic tensor elements. In addition, the relation of structural network features on the photoelastic response is investigated on a set of commercial optical quality glasses.

The content of this thesis is divided into five chapters. Chapter 2 briefly introduces the important theoretical background information on the three main topics of this thesis. The first topic defines glass formation along with the structural tendencies and theories that surround the subject. The next topic centers around photoelasticity and outlines several theories which try to relate structure to photoelastic response. Lastly, the subsection of photoelasticity being acousto-optics is described.

Experimental methods to determine the mechanical, optical, structural and photoelastic properties are given in Chapter 3. The mechanical properties, *ie*, the elastic moduli are calculated from the measured density and sound velocity of samples. The

structural properties are measured using X-ray diffraction, electron microprobe analysis, Raman spectroscopy and nuclear magnetic resonance spectroscopy. A description of the Dixon-Cohen method for determining the magnitude of the individual photoelastic tensor elements is also provided.

Chapter 4 presents the experimental data measured using the aforementioned techniques. This chapter further discusses the results that surround the structural and photoelastic trends that are recognized between samples.

Finally, the prominent results are summarized in Chapter 5 along with future suggestions to improve our understanding in this line of research.

Chapter 2

Background

This chapter briefly explains the background concerning the three main components that make up this dissertation. The first topic is glass. This exposition comprehensively explains glass formation, including its structural tendencies, typical glass-forming materials, and relevant glass properties. The next topic is that of photoelasticity. Stress can induce changes in the optical properties of materials. This section provides background on the phenomenon and outlines the major models of it in the literature. Finally, the last topic is that of acousto-optics. This is a technique used to measure the photoelastic tensor elements from sound-induced density perturbations in samples. Notably, glasses can be structurally tuned to design a wide variety of devices with specific photoelastic behaviour, which will be discussed.

2.1 Glass

Though easily overlooked in daily life, the success of glass as a material is significant. On the macroscopic scale, glass is a brittle, transparent and lustrous solid that is widely used for practical, decorative and technological applications. Whereas, microscopically, the structure of glass shows no long-range periodicity and has all the mechanical properties expected of a solid. Glasses are most commonly manufactured using high amounts of silica. As a consequence, it forms naturally from volcanic magma (obsidian) and from lighting striking sand (fulgurite) amongst others [5]. For which there is archaeological evidence, natural glass such as obsidian have been used by man since the Stone Age as sharp cutting and projectile objects [6]. The origin

of man-made glass is not certain. Yet, the earliest known glass glaze on stone beads date back to 12000 B.C. and the oldest pure glass item is an amulet from 7000 B.C. [6]. Glass was mainly used for decoration until the invention of glass blowing during the first century B.C., then the production of household items with this material had accelerated. Amidst the nineteenth century, high-precision optical glasses had been developed and used in instruments. This lead to a systematic approach to developing glasses with varied optical properties by altering the glass recipe.

2.1.1 Glass Formation

The formation of glass is most simply described using a volume (V) versus temperature (T) diagram. On the right side of the V-T diagram of Figure 2.1 is a liquid held at a temperature above its melting point T_m. As this liquid cools, it will typically undergo a sudden decrease in volume resulting from a phase change into its crystalline state where the atoms rearrange into a more condensed periodic structure. However, if the liquid is cooled at a considerably higher rate where the viscosity of the cooling liquid becomes so high and that there is not enough kinetic energy for the atoms to rearrange to their crystal lattice sites, the liquid is described to be super-cooled. The product of the super-cooled liquid is an meta-stable solid material in the glassy state that has a higher volume than its crystalline counterpart [7].

Although glass transformation occurs over a range of temperatures, it is convenient to refer the fictive temperature T_f as a single temperature at which a liquid steadily transforms from a super-cooled liquid state to a glassy state [5]. It is also important to note that T_f is a material property and can vary significantly between different glasses, and moreover, in a single glass as a function of cooling rate. It is also often referred to as the glass transition temperature T_g in literature.

Additionally, the free volume V_F of a material defines the temperature dependent volume difference between the non-crystalline $V(T)$ and crystalline solid $V_0(T)$. Below

T_f, the free volume is roughly constant and above T_f the free volume is a function depending on temperature. Cooling a material at different rates will result in a different free volume.

$$V_F(t) = V(T) - V_0(T) \tag{2.1}$$

It is worth mentioning without going into detail that other methods can be used to form a glass which do not utilize cooling such as the sol-gel process as well as chemical vapor deposition [5].

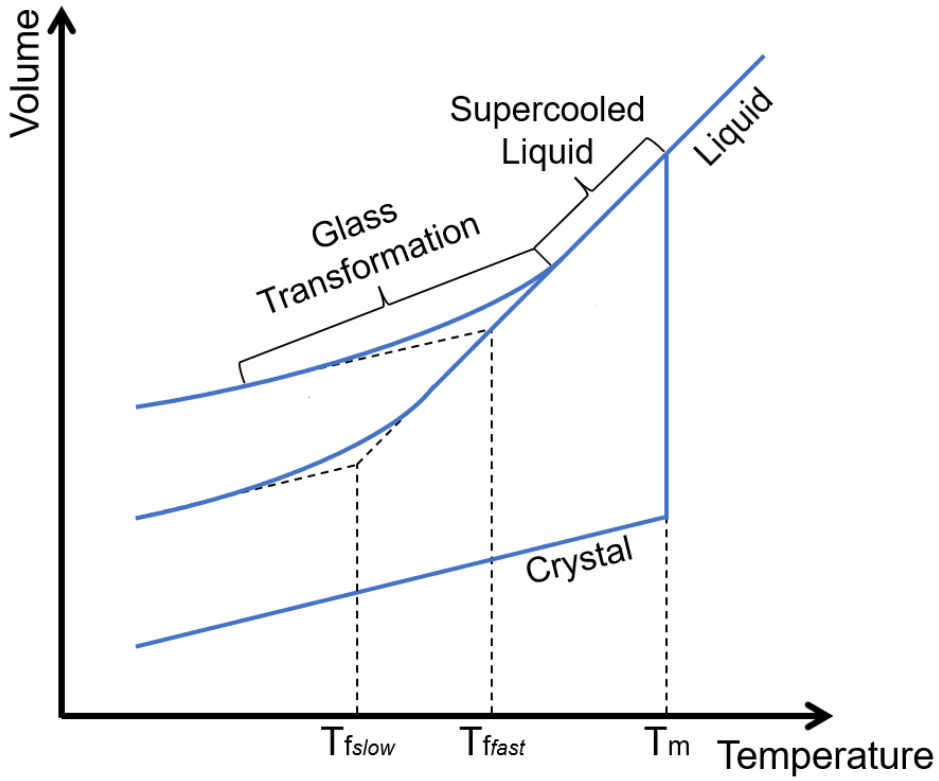

Figure 2.1: V-T diagram demonstrating the conventional glass formation from a liquid state. The volume of the glassy state being higher than that of the crystalline state

Pair Distribution Function of Glass

The pair distribution function (PDF) is often used to conceptualize the average distribution of atoms within amorphous materials from the local density around a

typical atom, and is given by Equation 2.2.

$$g(r) = \frac{1}{\langle\rho\rangle}\frac{dn(r, r+dr)}{dV(r, r+dr)} \tag{2.2}$$

Consider a sphere of radius r centralized around an arbitrary atom with a shell with a thickness dr and volume dV surrounding it. dn is the number is atoms within the shell and $\langle\rho\rangle$ is the average particle density. Namely, this is the probability of finding an atom at a certain distance r from an atom within the material that is normalized to the overall density of the material.

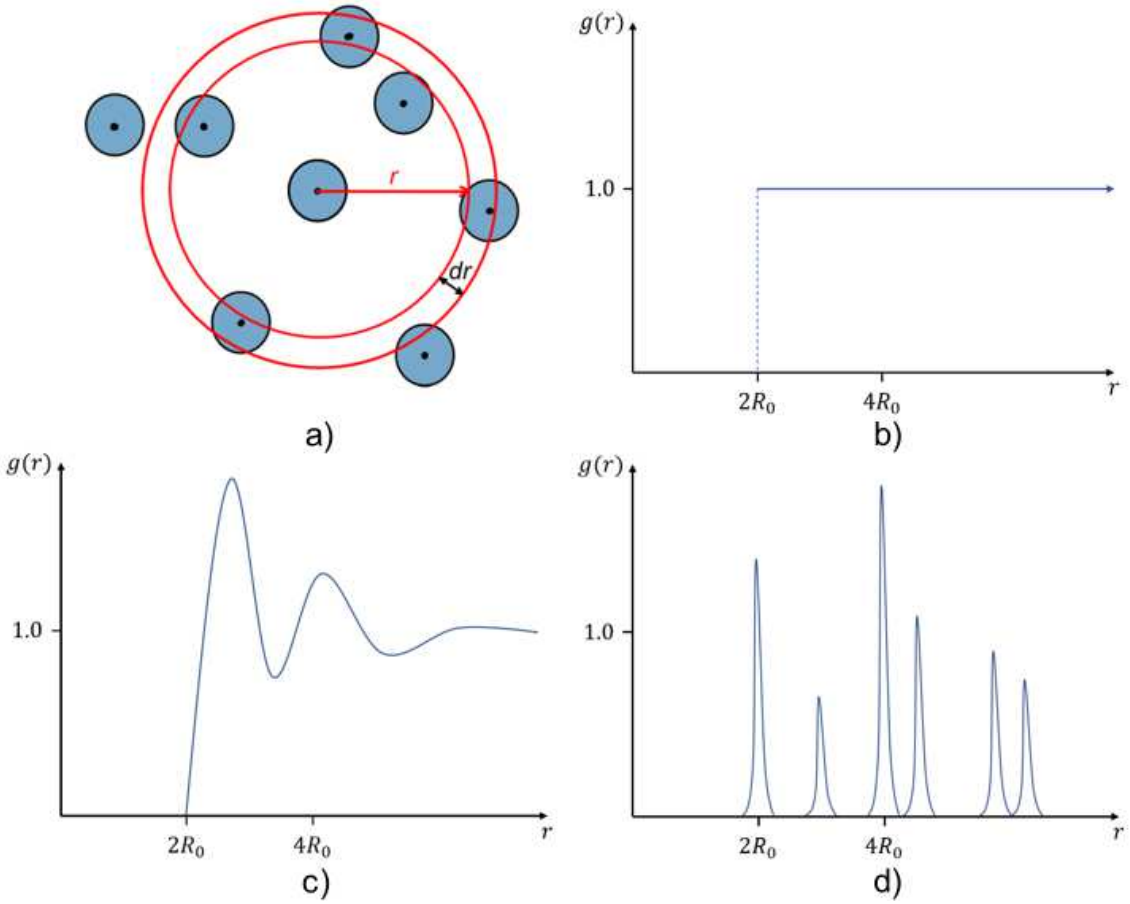

Figure 2.2: a) Example of pair distribution around a central atom, b) PDF of a gas, c) PDF of an amorphous solid or a liquid and d) PDF of a crystal

The PDF of a crystal is a set of discrete peaks at certain distances from the atom,

showing long-range order and is dependent on the crystal structure of the material. The PDF of a non-crystalline material shows broad features that eventually reach an asymptotic value of 1, demonstrating only short range order [5, 8].

2.1.2 Structural Theory of Glass: Zachariasen's Random Network

In 1932, Zachariasen publicized an empirical theory relating oxide glass formation and the structural tendencies of the glasses that is now widely used as a foundation for glass models. His initial intrigue sparked when Goldschmidt observed how oxide systems A_mO_n which have a radius ratio R_A/R_O between 0.2-0.4 form a glass [9]. This radius ratio corresponds to a tetrahedral arrangement of O anions around the A cation. Though this was a good starting point for predicting glass formation, it is not a universal fit. Zachariasen expanded on Goldschmidt's concept and stated that the silica glass structure is formed by a random network of tetrahedron that contrasts that of a periodic crystal structure [7]. The three-dimensional network must obey four rules:

1. The oxygen atoms cannot be linked to more than two cations

2. The cation coordination number must be small at either 3 or 4

3. The oxygen polyhedron cannot share edges or faces, only corners

4. The network can only be 3-D if the oxygen polyhedra share at least three corners

For instance, oxides of the formulas AO and A_2O do not fit the criteria that favors glass formation as they are not flexible enough to form a random network. The oxide glass network must have a connectivity balance in order to satisfy glass formation. The network must be flexible enough but not too flexible in order to avoid induction of crystallization.

Though the network of a glass is described in three dimensions, it is conventional to represent the structure in two dimensions. Both the crystalline and glass structures shown in Figure 2.3 are comprised of triangles of open circle anions connected to black dot cations, showing they have identical short-range connectivity. The disordered character of the glass network arises from the diverse A–O–A bond angles, as well as minute changes in anion-cation bond length compared to that of the crystal.

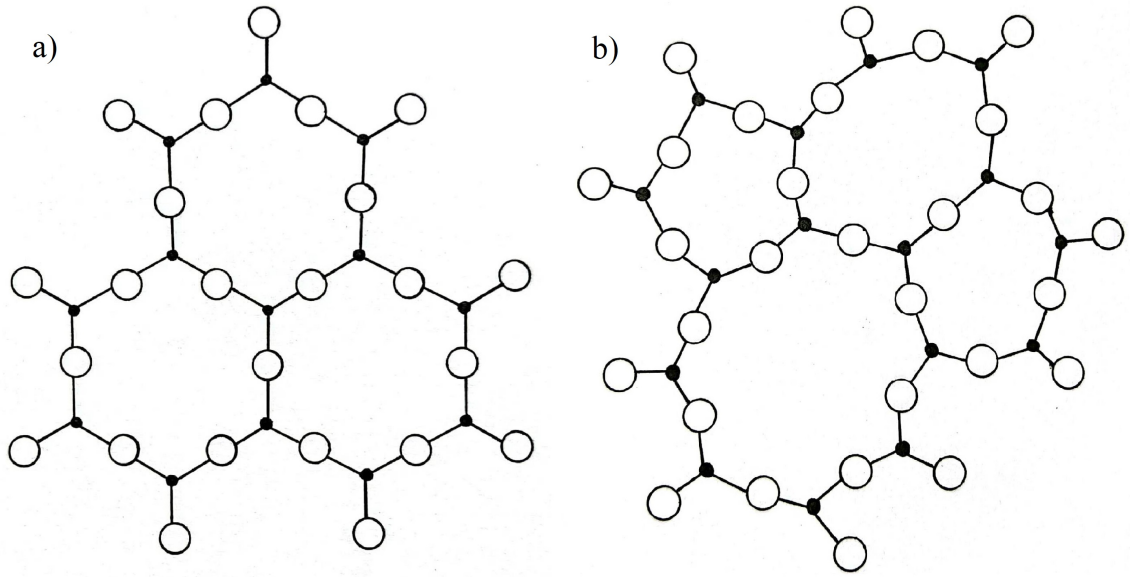

Figure 2.3: a) 2-D tetrahedral arrangement of atoms [eg. SiO_2 where the black dots are Si and the open circles are O] and b) 2-D amorphous arrangement of atoms of the same system

2.1.3 Glass Formers, Modifiers and Intermediates

Zachariasen's theory applies to glass network formers, which are oxide compounds capable of forming glass networks on their own. At the same time, the connectivity of glass networks can be greatly influenced by the introduction of network modifiers and intermediates to the system. Modifiers and intermediates are oxide compounds that are mixed with a network former to alter the physical properties of the glass. Modifiers are not able to form a glass network on their own, while intermediates can have

characteristics of both formers or modifiers. For example, when the modifier Na_2O is added to the network former SiO_2, several Si–O bonds are broken, creating non-bridging oxygens (NBOs) in the system [7]. Structures with less network connectivity are more pliable and will therefore have lower melting temperatures than a highly connected pure SiO_2 network.

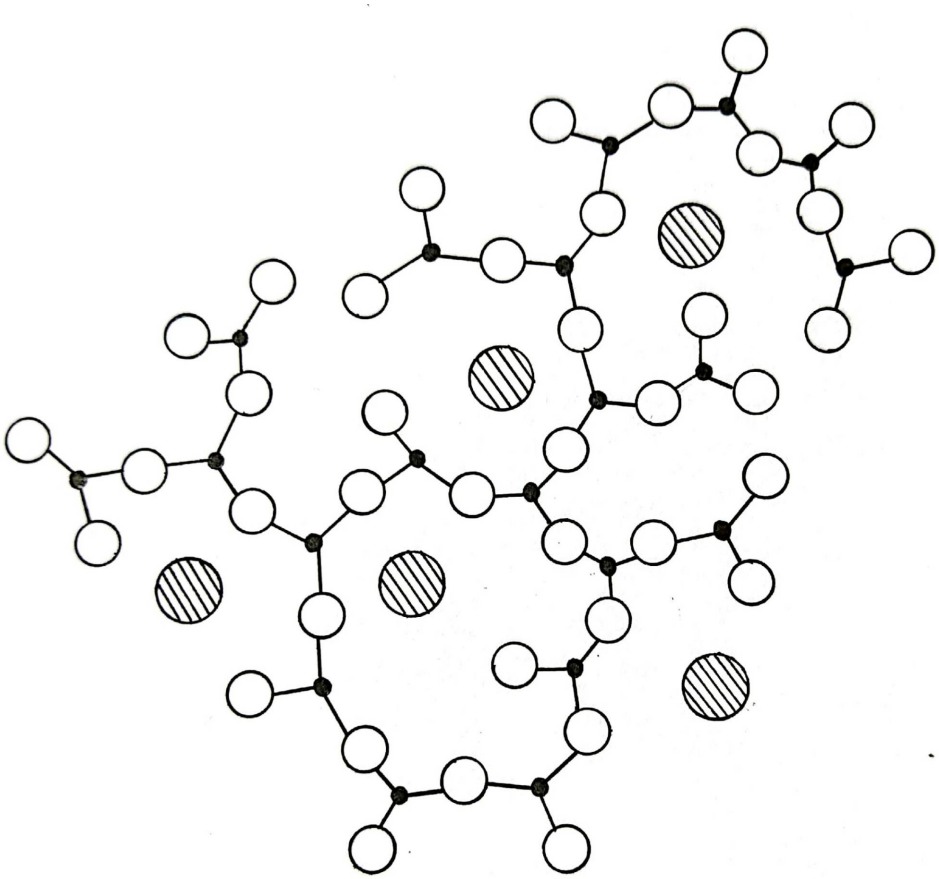

Figure 2.4: The connectivity of a silica glass network [black dots are Si and the open circles are O] is broken down by the addition of a Na_2O modifier [represented by the striped circles], increasing the number of NBOs

2.1.4 Silica Structures in Glass

As previously established, silica tetrahedrons may have different degrees of connectivity within a glass network. This depends on how many vertices of a silicon

tetrahedron are shared with other structures. They are classified as Q^n units, where n is the number of vertices shared [7]. This is often envisioned as the number of NBO atoms connected to the silicon atom. When all four vertices of a tetrahedron are connected to other polyhedrons, there are no NBOs, thus these structures are classified as Q^4 units. Q^3 units occur when three vertices are shared with one NBO, Q^2 when two vertices are shared and two are not, and finally Q^0 are isolated units that share no vertices and have all four NBOs.

2.1.5 Optical Properties of Glass

A key element to what makes glass an extensively important material is how it interacts with light. The optical properties of glass are crucial to the many design and technological applications that they are used for. One of the most measured optical properties of glass is the index of refraction n and is defined by a materials ability to refract light. Microscopically, light interacts with the electron density (polarizability) of a material. Glasses that contain atoms high atomic number (lead, bismuth, thallium) will generally have a higher index of refraction than those with lighter elements (silicon, boron, phosphorus) [7]. Additionally, NBOs in a glass network are more polarizable than bridging oxygens (BO), thus modifiers that form more NBO will also increase the refractive index.

Another feature of the index of refraction is its dependence on the wavelength of light. The variation of n with respect to λ determines a materials optical dispersion. Glasses are commonly classified by the Abbe number ν_d, which is a measure of the dispersion and is defined by Equation 2.3.

$$\nu_d = \frac{n_d - 1}{n_F - n_C} \tag{2.3}$$

where n_d, n_F and n_C are the refractive indices measured at the d, F and C emission

lines of hydrogen (587.56, 486.13 and 656.27 nm respectively) [7]. Glass manufacturers often have an Abbe diagram of their sample catalogue, which plots n_d with respect to ν_d. Crown glasses are traditionally categorized as having high Abbe number ($\nu_d > 50$) and generally have small indices of refraction, whilst flint glasses have a small Abbe number ($\nu_d < 50$) and usually have large indices of refraction [10]. That is to say crown glass has relatively low dispersion in comparison to flint glass which has relatively high dispersion. Figure 2.5 shows the Abbe diagram of CDGM Inc. glasses (K for crown and F for flint).

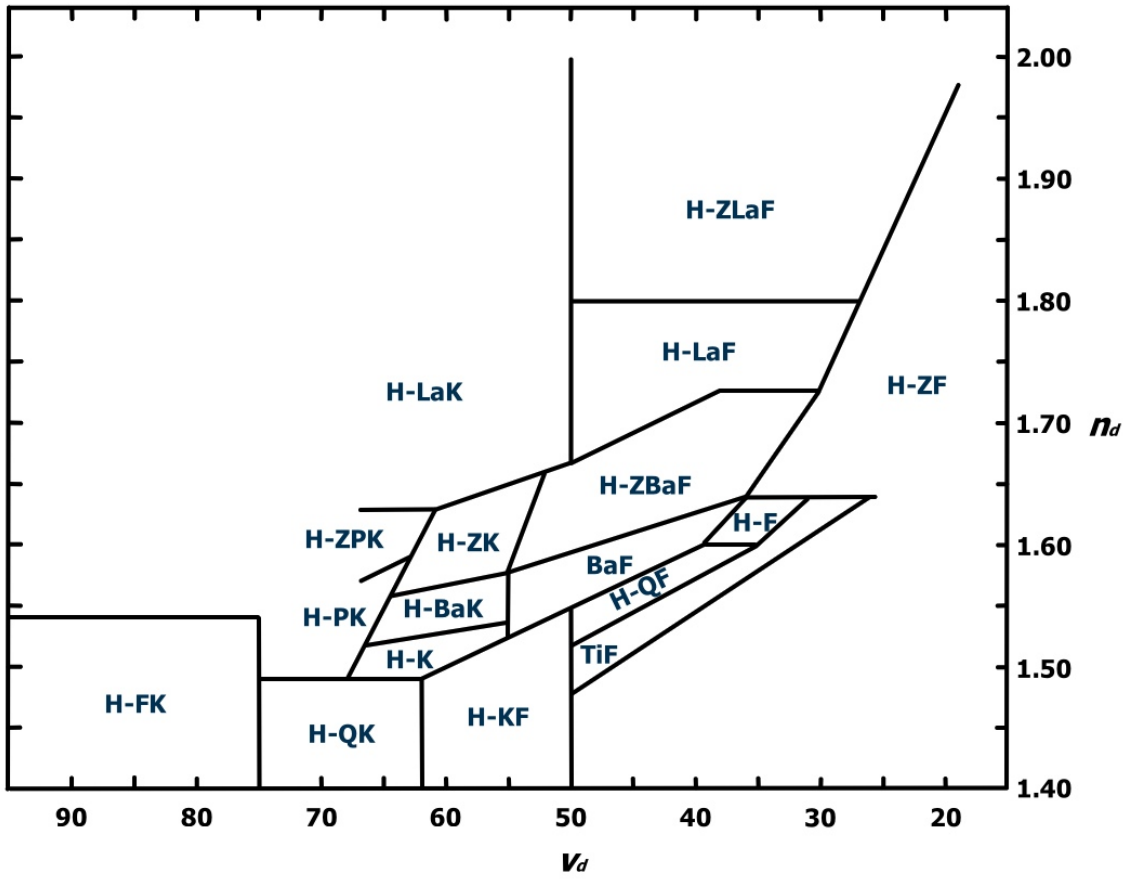

Figure 2.5: Abbe diagram of CDGM Inc. glasses

2.2 Photoelasticity

The term "photoelastic" can be interpreted in a literal sense: *photo-* being the optical properties of a material and *-elastic* being a materials ability to return to its original shape after being deformed. Thus, photoelasticity describes how a material under mechanical stress within the elastic limit will exhibit changes in its optical properties. Before elaborating on photoelasticity, it is reasonable to start by defining stress and strain.

2.2.1 Stress and Strain in the Elastic Region

Stress is a measure of a materials internal resistance to an applied force, and within the elastic limit, the internal resistance is equal to the external force. Consider a cubic volume as shown in Figure 2.6, where the stress is decomposed into three normal components and six shear components that form the stress tensor.

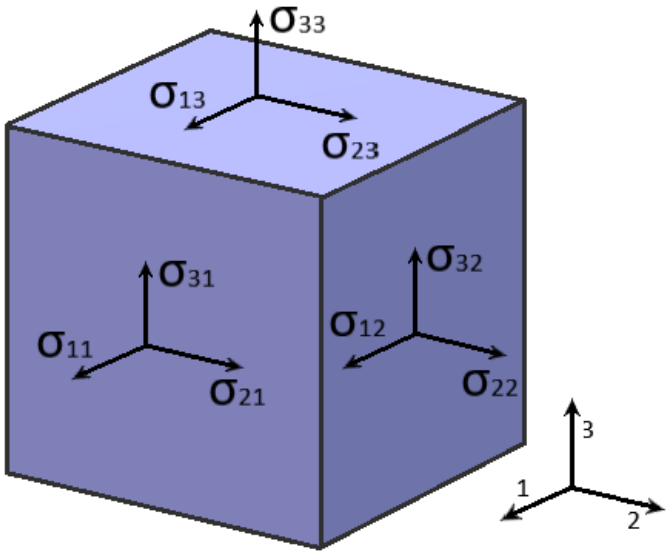

Figure 2.6: Directions of stress of a cubic volume

$$\sigma_{ij} = \begin{bmatrix} \sigma_{11} & \sigma_{12} & \sigma_{13} \\ \sigma_{21} & \sigma_{22} & \sigma_{23} \\ \sigma_{31} & \sigma_{32} & \sigma_{33} \end{bmatrix} \tag{2.4}$$

With any applied stress σ there is strain ϵ, since stress is what is done to a material and strain is what happens to the material as a result. Strain is a measure of the deformation undergone by the material. In the elastic region, these two mechanical properties are related to one-another by way of the elastic compliance constant s, where this linear relationship is known as Hooke's law [11, 12].

$$\epsilon = s\sigma \tag{2.5}$$

This can also be written in terms of the elastic stiffness constant, or Young's modulus E, where $E = 1/s$.

$$\sigma = E\epsilon \tag{2.6}$$

and the generalized form of Equations 2.5 and 2.6 may be written as

$$\epsilon_{ij} = s_{ijkl}\sigma_{kl} \qquad \sigma_{ij} = E_{ijkl}\epsilon_{kl} \tag{2.7}$$

In order to meet the requirement of static equilibrium, the cross-diagonal shear components of stress and strain are equal.

$$\sigma_{ij} = \sigma_{ji}, \qquad \epsilon_{ij} = \epsilon_{ji}$$

The elastic compliance and the elastic stiffness constants have 81 coefficients each, forming fourth-rank tensors. They also have symmetry conditions that reduce the

number of independent coefficients from 81 to 36.

$$s_{ijkl} = s_{jikl} = s_{ijlk}, \qquad E_{ijkl} = E_{jikl} = E_{ijlk}$$

An abbreviated notation may also be used for these terms

11	22	33	23, 32	13, 31	12, 21
1	2	3	4	5	6

Therefore Equation 2.7 shortens to

$$\epsilon_i = s_{ij}\sigma_j \quad \sigma_i = E_{ij}\epsilon_j \quad (i,j = 1,2,...6) \tag{2.8}$$

For isotropic materials, the s_{ij} and E_{ij} matrices have only two independent coefficients and have the form

$$\begin{bmatrix} \bullet & \bigstar & \bigstar & 0 & 0 & 0 \\ \bigstar & \bullet & \bigstar & 0 & 0 & 0 \\ \bigstar & \bigstar & \bullet & 0 & 0 & 0 \\ 0 & 0 & 0 & \blacktriangledown & 0 & 0 \\ 0 & 0 & 0 & 0 & \blacktriangledown & 0 \\ 0 & 0 & 0 & 0 & 0 & \blacktriangledown \end{bmatrix} \tag{2.9}$$

where $\blacktriangledown = 2(s_{11} - s_{12})$ for s and $\blacktriangledown = \frac{1}{2}(E_{11} - E_{12})$ for E.

2.2.2 Photoelastic Effect

Annealed glass is an example of a solid that is optically isotropic, a term used to describe uniform index of refraction in all directions. The *photoelastic effect* or the *acousto-optic effect* is the change in the optical properties when a material in under mechanical stress. We can depict the the index of refraction as an ellipsoid with the

following constraint equation called the optical indicatrix:

$$\frac{x_1^2}{n_1^2} + \frac{x_2^2}{n_2^2} + \frac{x_3^2}{n_3^2} = 1 \tag{2.10}$$

An unstrained isotropic material has a spherical optical indicatrix. Upon application of uniaxial strain, two of the indices would be equal, while one would be different along the stress axis. For convenience, the impermeability tensor $\sum_{ij} B_{ij} x_i x_j = 1$ is often called in to replace $1/n_i^2$. Thus Equation 2.10 is now:

$$B_{11}x_1^2 + B_{22}x_2^2 + B_{33}x_3^2 = 1 \tag{2.11}$$

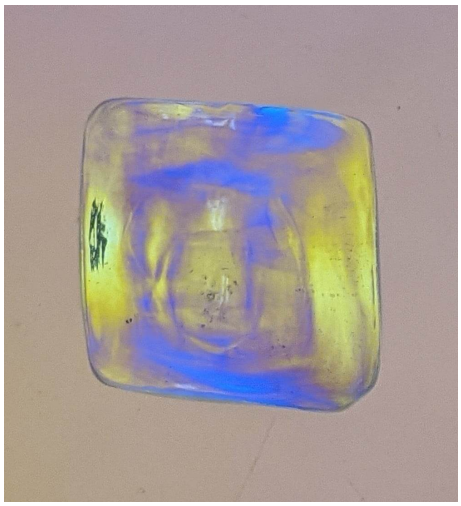

Figure 2.7: Glass sample with residual internal stress viewed from a polariscope (table top instrument where a light source travels through a sample, a polarizer, a quarter-wave plate and an adjustable analyzing polarizer to detect internal stress birefringence).

One can assume the change in B_{ij} between the strained and unstrained (superscript 0) states is a linear function of stress and strain in the elastic regime.

$$B_{ij} - B_{ij}^0 = -q_{ijkl}\sigma_{kl} = p_{ijkl}\epsilon_{kl} \tag{2.12}$$

where q_{ijkl} and p_{ijkl} are the piezo-optic and photoelastic tensors, respectively. This photoelastic effect may be written with abbreviated Voigt notation as:

$$\Delta B_i = \frac{1}{\Delta n_i^2} = p_{ij}\epsilon_k \tag{2.13}$$

For isotropic materials, the tensor takes the same form as Equation 2.9.

$$p_{ij} = \begin{bmatrix} p_{11} & p_{12} & p_{12} & 0 & 0 & 0 \\ p_{12} & p_{11} & p_{12} & 0 & 0 & 0 \\ p_{12} & p_{12} & p_{11} & 0 & 0 & 0 \\ 0 & 0 & 0 & p_{44} & 0 & 0 \\ 0 & 0 & 0 & 0 & p_{44} & 0 \\ 0 & 0 & 0 & 0 & 0 & p_{44} \end{bmatrix} \tag{2.14}$$

Where p_{11} is related to the change in the index of refraction along the extraordinary direction, p_{12} is related to the change in the index of refraction along the ordinary direction and the shear element p_{44} depends on p_{11} and p_{12}.

$$2p_{44} = p_{11} - p_{12} \tag{2.15}$$

Moreover, *birefringence* b refers to the difference between the index of refraction along the direction of stress n_e (extraordinary axis) and the index of refraction perpendicular to the direction of stress n_o (ordinary axis). Birefringence varies linearly with applied stress, and the constant of proportionality is the stress-optic coefficient C.

$$b = n_e - n_o = C\sigma \tag{2.16}$$

2.2.3 Mueller's Theory of Photoelasticity in Amorphous Solids

In order to explain photoelasticity at an atomistic scale, Hans Mueller considered how the deformation of a solid affects the Lorentz-Lorentz field and the Coulomb field from the ions within a strained boundary. However, there was a discrepancy between the calculated value of the refractive index and what was measured experimentally [13]. He thus introduced a correction factor from the optical anisotropy of the atoms. When the atomic structure of a solid is deformed under stress, the distance between atoms parallel to the stress decrease, and the distance between atoms perpendicular to the stress increase, causing anisotropic strain. As a result, the physical properties that depend on the atomic arrangement of the atoms must also account for the anisotropy of the strain, such as the polarizability of the ions [14].

Consider the displacement of an arbitrary electron from an applied electric field. The Coulomb fields from the other surrounding ions will affect the electron and the Lorentz-Lorentz force from the induced polarization from the external field must also be considered. This gives rise to an induced dipole moment, $\boldsymbol{\mu}_j$,

$$\boldsymbol{\mu}_j = \alpha_j \boldsymbol{E}_{eff} \tag{2.17}$$

where α_j is the polarizability of the ion and $\boldsymbol{E}_{eff}$ is the effective electric field. The applied electric field causes dielectric displacement $\boldsymbol{D}$, thus from Maxwell's equations,

$$\boldsymbol{D} = \varepsilon \boldsymbol{E} \tag{2.18}$$

$$\boldsymbol{D} = \boldsymbol{E} + 4\pi \boldsymbol{P} \tag{2.19}$$

where $\boldsymbol{P}$ is the polarization which can be described as the density of dipole moments

within a volume.

$$\boldsymbol{P} = \sum_j N_j \boldsymbol{\mu}_j = \sum_j N_j \alpha_j \boldsymbol{E}_{eff} \tag{2.20}$$

where N_j is the number of oscillators per unit volume of type j. For non-magnetic materials, the dielectric constant is directly related to the index of refraction via the relation $\varepsilon = n^2$. Combining Equations 2.18, 2.19 and 2.20 yields

$$(n^2 - 1)\boldsymbol{E} = 4\pi \boldsymbol{P} = 4\pi \sum_j N_j \alpha_j \boldsymbol{E}_{eff} \tag{2.21}$$

Finally, apply strain to the index of refraction by differentiating Equation 2.21 with respect to strain ϵ to obtain an equation that represents the three constituents that make up Mueller's theory of photoelasticity.

$$2n\frac{dn}{d\epsilon}\boldsymbol{E} = 4\pi \sum_j \left(\frac{dN_j}{d\epsilon}\alpha_j \boldsymbol{E}_{eff} + N_j \frac{d\alpha_j}{d\epsilon}\boldsymbol{E}_{eff} + N_j \alpha_j \frac{d\boldsymbol{E}_{eff}}{d\epsilon} \right) \tag{2.22}$$

The first term within the brackets is the change in number density of atomic sites as a function of strain. The third term within the brackets is the change in the effective field as a function of applied strain. These two terms were previously determined from earlier works, but alone did not correlate well with experimental data. The second term within the brackets describes the change in the polarizability of the ions with applied strain and is Mueller's contribution to the atomistic theory of photoelasticity [13].

For the sake of deriving expressions with respect to the photoelastic tensor elements, Mueller proved that for an amorphous solid, an ellipsoidal boundary must be considered in the deformation state [14]. When a strain z occurs in the z-direction the axial ratio is 1:1:1+z. Now, the effective field components outside the boundary are:

$$
\begin{aligned}
E_{eff,x} &= E_x + 4\pi P_x\left(\frac{1}{3} + \frac{2}{15}z\right) \\
E_{eff,y} &= E_y + 4\pi P_y\left(\frac{1}{3} + \frac{2}{15}z\right) \\
E_{eff,z} &= E_z + 4\pi P_z\left(\frac{1}{3} - \frac{4}{15}z\right)
\end{aligned}
\tag{2.23}
$$

Substituting in Equation 2.21, Equation 2.23 can be written in terms of the indices of refraction. The following equation only shows the x-component. However the y- and z-components also have corresponding equations for n_y and n_z.

$$
n_x^2 - 1 = 4\pi \sum_j N_j \alpha \rho \left[1 + (n_x^2 - 1)\left(\frac{1}{3} + \frac{2}{15}z\right)\right] \tag{2.24}
$$

To obtain equations for the photoelastic tensor elements in terms of the index of refraction, Equation 2.24 is differentiated with respect to strain, keeping the polarizability α constant. In doing this Mueller had found this resulted in poor agreement with experimental p_{ij} data. This confirms the need to take the dependence of strain on the polarizability into account.

Hence the polarizability of the atoms must behave anisotropically. Since the photoelastic effect varies linearly with strain, the same assumption is made for α.

$$
\begin{aligned}
\alpha_z &= \alpha(1 + \lambda_1 z) \\
\alpha_{x,y} &= \alpha(1 + \lambda_2 z)
\end{aligned}
\tag{2.25}
$$

where λ_1 and λ_2 are the strain polarizability constants. The optical deformability constants for each atom are also defined as

$$
L_{1,2} = \frac{\sum(\lambda_{1,2} N\alpha/M)_i}{\sum(N\alpha/M)_i} \tag{2.26}
$$

where M is the molar mass. Thus, the expressions for the photoelastic tensor elements are:

$$\begin{aligned} p_{11} &= \left(\frac{n^2-1}{3n^4}\right)\left[(n^2+2) + \frac{4(n^2-1)}{5} - L_1(n^2+2)\right] \\ p_{12} &= \left(\frac{n^2-1}{3n^4}\right)\left[(n^2+2) - \frac{2(n^2-1)}{5} - L_2(n^2+2)\right] \\ 2p_{44} = p_{12} - p_{11} &= \left(\frac{n^2-1}{3n^4}\right)\left[\frac{6(n^2-1)}{5} + (L_2 - L_1)(n^2+2)\right] \end{aligned} \tag{2.27}$$

It can be concluded that experimental photoelastic data is needed in order to obtain $L_{1,2}$ as these are not known. The major gripe about Mueller's model is the fact that is does not carry much, if any, predictive value in terms of which glass compositions will have a desired effect on the photoelastic response.

2.2.4 Bond Polarizability Model of Photoelasticity

In contrast to the Mueller model described above, Cardona and colleagues developed a model of photoelasticity based on polarizability of the bonds, rather than the ions. The total crystal polarizability P_{ij} may be written as a sum of bond polarizabilities between nearest-neighbour pairs of atoms i and j [15, 16].

$$P_{ij}(R^b) = \sum_b \left[\hat{R}_i^b \hat{R}_j^b \alpha_{||}^b + (\delta_{ij} - \hat{R}_i^b \hat{R}_j^b)\alpha_{\perp}^b\right] \tag{2.28}$$

where $\alpha_{||}$ and $\alpha_{\perp}$ are the parallel and perpendicular components of the bond polarizabilities that depend on the bond length R^b. The incentive of this model stems from a history of physical chemists using bond polarizabilities to describe the polarizability of molecules [15]. In this case, crystals are assumed to be large molecules. The atomic bonds are also assumed to have cylindrical symmetry with respect to the "line" connecting two atomic centers. In the field solid-state physics, many models

are built to fit experimental first- and second-order Raman spectra with bond polarizabilities since they correlate directly with the vibrational frequencies of lattices [17, 16]. Equation 2.28 may also be written in terms of the linear susceptibility χ_{ij}, given that it is related to the total polarizability of materials ($\chi_{e,ij} = n_b/VP_{ij}$), where n_b/V is the bond density (number of bonds/unit volume).

For small strains, Equation 2.13 can be written as

$$\sum_j p_{ij}\epsilon_j = -\frac{\Delta\varepsilon_i}{\varepsilon(0)^2} \tag{2.29}$$

which can be related to the bond polarizabilities through $\varepsilon_{ij} = 1 + \chi_{e,ij}$, where $\varepsilon(0)$ is the unstrained permittivity [18]. When an isotropic cubic volume is subject to pure dilation, the strain $\epsilon_j = \epsilon$ for $j = 1, 2, 3$ and $\epsilon_j = 0$ otherwise. And since strain is the fractional change in the length of the cube ($\epsilon = 1/3\ dV/V$), Equation 2.29 yields

$$p_{11} + 2p_{12} = -\frac{3V}{\varepsilon(0)^2}\left(\frac{\partial\varepsilon_i}{\partial V}\right) \tag{2.30}$$

where

$$\frac{\partial\varepsilon_i}{\partial V} = \frac{\partial}{\partial V}\left(1 + \frac{n_b}{V}P_{ij}\right) = \frac{n_b}{V}\frac{\partial P_{ij}}{\partial V} - \frac{n_b}{V^2}P_{ij} \tag{2.31}$$

Note that the total polarizability may be written as $P = \alpha_{||} + 2\alpha_{\perp}$. Thus, Equation 2.30 can finally be written as

$$p_{11} + 2p_{12} = \frac{3n_b}{\varepsilon(0)^2}\ (\alpha_V - \alpha_1) \tag{2.32}$$

where

$$\alpha_V = \frac{n_b}{V}(\alpha_{||} + 2\alpha_{\perp}) \equiv \chi_e \equiv \varepsilon - 1 \tag{2.33}$$

$$\alpha_1 = n_b\frac{\partial}{\partial V}(\alpha_{||} + 2\alpha_{\perp}) \tag{2.34}$$

are the pure dilation polarizability parameters. α_V is essentially the permittivity and will always be positive. α_1 is less straightforward as it deals with the change in the polarization with respect to volume, thus combining changes in the structure with the electronic properties. Similarly, under anisotropic strain, the photoelastic constants may be written in terms of the anisotropy polarizability parameter α_Q.

$$p_{11} - p_{12} = -\frac{1}{\varepsilon^2}\alpha_Q \tag{2.35}$$

$$\alpha_Q = \frac{n}{V}(\alpha_\parallel - \alpha_\perp) \tag{2.36}$$

To average over all directions, the n_b/V can be replaced with $\langle\rangle$. From Equations 2.32 2.33, 2.34, 2.35, and 2.36, all average polarizability parameters can be calculated from experimental values of p_{11}, p_{12} and $\varepsilon(0) = n^2$.

2.2.5 Empirical Model of Photoelasticity

In an effort to correlate the stress-optic response to the atomic bonding of a glass, Zwanziger and Guignard noticed a trend with the sign of the stress-optic coefficient C and the bond metallicity and coordination number of common glass compounds. They approached the problem by combining first principles calculations and literature values to develop an empirical model of photoelasticity [19]. They then used this model to predict glass systems with a zero stress-optic response and confirmed their predictions by testing synthesized samples.

Bond metallicity involves the strength and type of chemical bonds between atoms. In glasses, this usually refers to a cation A bonded to an oxygen anion O. For example, due to the differences in metallicity and polarizability, a Si–O bond will exhibit an exceedingly different stress response compared to a Pb–O bond. The difference in polarizability along and perpendicular to the bonds is synonymous to the distortion in the corresponding bond directions with an applied stress. High metallicity bonds

are less directional and will exhibit distortions in both directions. The cation-anion bond length d is associated with the bond metallicity.

In addition to this, the stress response also depends on the local cation environment. The cation coordination number N_c determines the structural anisotropy. Compounds with low coordination number are more susceptible to distortions than those with high coordination number. The model concludes that the ratio of d/N_c can predict whether a compound will have a positive or negative stress-optic response. A d/N_c less than 0.5 Å was noticed to have a positive stress-optic coefficient, while a d/N_c greater than 0.5 Å had a negative stress-optic coefficient. Table 2.1 lists the ratio of d/N_c and signs of C of several common glass formers and modifiers. Since most glasses are composed of more than a single compound, the ratio is molar weighted x_i to find the average d/N_c, as Equation 2.37 demonstrates.

$$\left\langle \frac{d}{N_c} \right\rangle = \sum_i x_i \left(\frac{d}{N_c} \right)_i \approx 0.5 \text{ Å} \tag{2.37}$$

Table 2.1: Examples of d/N_c and associated sign of the stress-optic coefficient C of common glass oxide compounds from [19]

Oxide	d/N_c (Å)	sign of C
P_2O_5	0.38	+
SiO_2	0.40	+
BaO	0.46	+
B_2O_3	0.46	+
ZnO	0.50	+
PbO	0.58	−
Sb_2O_3	0.67	−

2.3 Acousto-Optic Effect

As mentioned in Section 2.2.2, the acousto-optic effect is a particular case of the photoelastic effect. What makes the acousto-optic effect unique is how mechanical

strain is applied to cause birefringence. In this circumstance, acoustic waves are used to induce molecular perturbations within the material causing variations in the index of refraction between regions of higher and lower density. There are a multitude of optical devices that are designed to take advantage of the acousto-optic effect such as switches, modulators and filters to name the least [20].

2.3.1 Bragg Diffraction

Simply put, sound acts as a diffraction grating travelling at a characteristic sound velocity dependent on the medium. When an incident optical wave with a wavelength λ interacts with the sound wave with a wavelength Λ in the medium, the optical beam is diffracted if the angle of incidence satisfies the Bragg condition θ_B for constructive interference.

$$\sin\theta_B = \frac{\lambda}{2\Lambda} \tag{2.38}$$

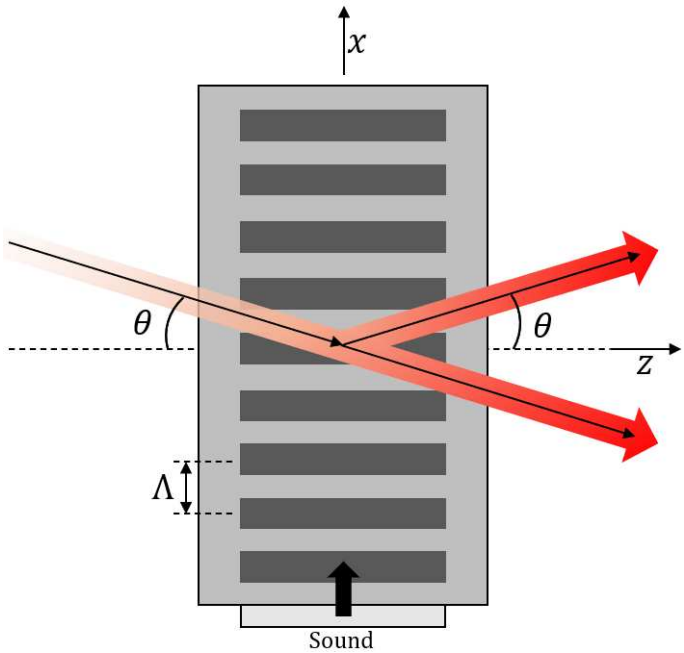

Figure 2.8: Bragg diffracting occurring when the incident light is set to the Bragg angle dependent on the medium

Acousto-Optic Figure of Merit

Suppose an acoustic plane wave travelling in the x-direction of a material with velocity v_a creates a time-dependent strain of the form of Equation 2.39.

$$\epsilon(x,t) = A\cos(\Omega t - qx) \tag{2.39}$$

where A is the amplitude, $\Omega = 2\pi f$ is the angular frequency and $q = \frac{2\pi}{\Lambda}$ is the wavenumber. As mentioned previously, strain creates a change in the index of refraction between the unperturbed and strained states of the optically transparent material. Although strain does not produce a large change in n, thus the following approximation can be made:

$$\frac{1}{\Delta n_i^2} = \frac{n^2 - n_i^2}{n^2 n_i^2} = \frac{(n - n_i)(n + n_i)}{n^4} = \frac{2\Delta n_i}{n^3} \tag{2.40}$$

as $n \approx n_i$, where n is the unstrained index of refraction. Substitution this expression for $1/\Delta n_i^2$ into Equation 2.13.

$$\Delta n(x,t) = -\frac{1}{2} p_{ij} n^3 \epsilon(x,t) \tag{2.41}$$

where the negative sign represents a reduction of n from positive strain. The resulting index of refraction can then be represented as a inhomogeneous time-dependent wave by combining Equations 2.39 and 2.41.

$$n(x,t) = n - \Delta n_0 \cos(\Omega t - qx) \tag{2.42}$$

where the amplitude Δn_0 is:

$$\Delta n_0 = \frac{1}{2} p_{ij} n^3 A \tag{2.43}$$

The acoustic intensity in a medium, $I_a = \frac{1}{2}\rho v_a^3 A^2$, may be substituted into Equation 2.43 to get an equation that shows the proportional relationship between Δn_0 and $I_a^{1/2}$.

$$\Delta n_0 = \sqrt{\frac{p_{ij}^2 n^6}{\rho v_a^3}\frac{I_a}{2}} = \sqrt{\frac{1}{2}M_a I_a} \tag{2.44}$$

The acousto-optic figure of merit M_a is a material-dependent parameter that describes the effectiveness of the acousto-optic effect (diffracted light intensity per unit of ultrasonic power) [20].

$$M_a = \frac{p_{ij}^2 n^6}{\rho v_a^3} \tag{2.45}$$

2.3.2 Stimulated Brillouin Scattering

An application of determining the individual photoelastic tensor elements is the connection between p_{12} and stimulated Brillouin scattering (SBS). SBS is a nonlinear optical photon scattering phenomenon that can limit the signal transmission in optical fibers [21]. Essentially, a portion of light travelling through an optical fiber is converted to an acoustic phonon by means of electrostriction (strain in a bulk material caused by an external electric field) [22]. The acoustic wave acts as a diffraction grading in the fiber, which scatters part of the incident photon in the backward direction, causing interference with the rest of the signal. On top of that, there is an input power threshold that once exceeded will back scatter any excess signal that could result in tremendous signal loss [23]. This threshold controls the maximum input power for fiber-optic communications.

Spontaneous Brillouin scattering can occur in optical fibers due to thermal motions of the molecules that make up the material, but is generally a very weak elastic scattering process. The problem arises when this becomes a stimulated process as the intensity of the incident (pump) wave is so high that the backscattered (Stokes) wave propagates further without significant attenuation. In turn, this causes an

intensity (thus density) modulation that amplifies the acoustic wave, which amplifies the Stokes wave, which amplifies the intensity modulation, and the process continues [23].

The intensity of the Stokes wave I_S depends on the fiber material with a specific Brillouin gain coefficient g_B, the intensity of the pump wave I_P and the signal attenuation ξ and is given by Equation 2.46. A similar relationship for the intensity of the pump wave is given by Equation 2.47.

$$\frac{dI_S}{dz} = -g_B I_P I_S + \xi I_S \tag{2.46}$$

$$\frac{dI_P}{dz} = -g_B I_P I_S - \xi I_P \tag{2.47}$$

The Brillouin gain coefficient influences the intensity of the Stokes wave and has a spectral distribution with a relatively narrow bandwidth. The peak Brillouin gain $g_{B(max)}$ depends on several material parameters and is given by Equation 2.48.

$$g_{B(max)} = \frac{4\pi n^8 p_{12}^2}{c\lambda_P^3 \rho f_A \Delta f_A} \tag{2.48}$$

where λ_P is the wavelength of the pump wave, f_A is the frequency shift between the pump and Stokes wave and Δf_A is the linewidth distribution of the Brillouin gain. Due to the dependence of the maximum Brillouin gain on the photoelastic properties of the fiber, materials that have larger p_{12} will exhibit larger SBS [24]. Consequently, having a small refractive index, small photoelastic constant, large density, and large acoustic attenuation are fitting properties when it comes to designing optical fibers with minimal Brillouin gain. Theoretically, p_{12} is the only parameter in Equation 2.48 that can have a value of zero [21].

Chapter 3

Experimental Methods

This chapter will briefly describe the techniques used to analyze the optical and structural properties of a selection of commercial glass samples studied in this thesis.

3.1 Glass Samples and Preparation

3.1.1 CDGM Commercial Glasses

All samples analyzed in this thesis were manufactured by CDGM Glass Co., Ltd. Four optical-grade glasses were chosen based on their compositional similarities reported in their MSDS sheets. The samples in question are H-BaK1, H-BaK3, H-BaK8 and H-BaF2. The prefix H- is designated for glasses that do not contain lead, arsenic, cadmium and other radioactive elements. The classification BaK is a barium crown glass and BaF is a barium flint glass. Recall that crown glasses typically have low dispersion and small index of refraction and flint glasses typically have relatively high dispersion and large index of refraction. Two additional CDGM glasses, H-ZF72A and H-ZF72AGT, were provided and prepared by Illumina, Inc. The classification ZF is for dense flint glass, the A indicates a composition improvement, and the GT suffix indicates high-transmittance. There is no difference between the optical and mechanical properties between the H-ZF72A and H-ZF72AGT other than the internal transmittance and colour code in reference to the sample catalogue.

3.1.2 Sample Preparation

Ideal sample dimensions for the Dixon-Cohen apparatus are 15-25 mm long (along the optical beam path), 10-15 mm wide and 5-7 mm high (along the acoustic beam path). Samples were cut to these dimensions with the Buehler Isomet low speed saw equipped with a diamond blade to obtain relatively parallel sides. The optical beam faces are polished to 0.06 μm, the acoustic beam faces are lapped with the Logitech PM5 machine to obtain very flat, parallel sides and polished to 1 μm, and the other two faces can be left roughly cut. These samples are also optimal for sound velocity and index of refraction measurements. The H-ZF72A and H-ZF72AGT samples provided by Illumina, Inc. have anti-reflective (AR) coatings applied to their optical faces for maximum transmission at the laser wavelengths of 405 nm, 543 nm, 594 nm, 670 nm, 785 nm, 850 nm.

Samples used for EPMA needed only to be roughly 5 x 5 x 5 mm^3 and have one face polished to 1 μm.

Samples used for X-Ray, Raman and NMR Spectroscopy were crushed to a fine powder with a mortar and pestle.

3.2 Determination of Density

Archimedes' principle was used to determine the density of the glass samples with a Mettler Toledo density kit. The weight of the sample in air w_1 is compared to the weight of the sample submerged in a liquid w_2 with a well-known density ρ_2, such as pure ethanol, in order to obtain an accurate density measurement for the glass sample ρ_1. After the sample is submerged in the liquid, the apparent weight of the sample decreases, which indicates that some amount of the liquid had been displaced. If the sample is completely immersed in the liquid, then the volume of the displaced liquid is equivalent to the volume of the sample. The density of the sample may therefore

be calculated in terms of the measured weights and the density of liquid.

$$V = \frac{w_1}{\rho_1} = \frac{w_1 - w_2}{\rho_2} \implies \rho_1 = \frac{w_1}{w_1 - w_2}\ \rho_2. \tag{3.1}$$

3.3 Sound Velocity Measurements

The longitudinal and transverse speeds of sounds of the glass samples were measured using an Olympus 45MG Ultrasonic Thickness Gauge. This instrument is normally used to measure the thickness of materials (commonly used to find corrosion and defects in walls and pipes) with known speeds of sound [25]. However, the instrument could be used the other way around. The thickness gauge measures the time, t, it takes for an ultrasonic pulse generated from a piezoelectric transducer to travel through a material with thickness T and reflect back from the far surface. The reflected signal travels back to the transducer and is detected. Hence, the speed of sound is determined as:

$$v = \frac{2T}{t} \tag{3.2}$$

A small drop of coupling fluid between the transducer and the test sample is necessary to fill in the air gap that would otherwise be enclosed by the surfaces and to enable good acoustic transmission. Sound waves do not travel as efficiently through the interface between two materials with vastly different speeds of sounds, such as air to glass. Coupling the speed of sound of a solid sample with a fluid with similar speed of sound helps to reduce the acoustic reflection at the interface between the transducer and the sample. Glycerin works well with the longitudinal transducer and Olympus SWC-2 is a high viscosity fluid that works well with the transverse transducer.

3.4 Mechanical Property Calculations

Many mechanical properties of materials can be directly calculated from the density ρ and the transverse and longitudinal speeds of sound v_T and v_L of the aforementioned material [5]. Specifically, the elasticity of a material can be determined from Poisson's ratio ν, Young's modulus E, the shear modulus G and the bulk modulus K. The elastic moduli describe how a material responds to an applied stress. In particular, the Poisson ratio is given by

$$\nu = \frac{1 - 2(v_T/v_L)^2}{2 - 2(v_T/v_L)^2}; \tag{3.3}$$

the Young's modulus by

$$E = \rho v_T^2 \ \frac{3v_L^2 - 4v_T^2}{v_L^2 - v_T^2}; \tag{3.4}$$

the shear modulus by

$$G = \rho v_T^2; \tag{3.5}$$

and the bulk modulus by

$$K = \rho(v_L^2 - 4/3v_T^2). \tag{3.6}$$

3.5 Index of Refraction Measurements

The index of refraction of the barium crown and flint (H-BaK, H-BaF) glasses were measured with the bench-top Atago DR-M4/1550 Abbe refractometer at 450, 486, 540, 656 and 700 nm. A transparent solid sample of unknown index is set on a prism with a contact liquid with a higher index of refraction than the measured sample [26]. As seen in Figure 3.1, a monochromatic light source shines through the sample (at multiple angles of incidence), then the contact fluid refracts the light into the main prism. From the prism, the light travels through a telescope from which

the user can observe the boundary line between light and shadow. The focus and location of the boundary line can be adjusted so that it lines up with the intersection point of the cross hairs seen through the eyepiece. The display panel indicates the refractive index which depends on the boundary line adjustment.

The refractometer operates on the concept of the critical angle and total internal reflection. The shadow at the boundary line is made by the critical angle of the sample, from which the index of refraction of the sample can be determined from Snell's law.

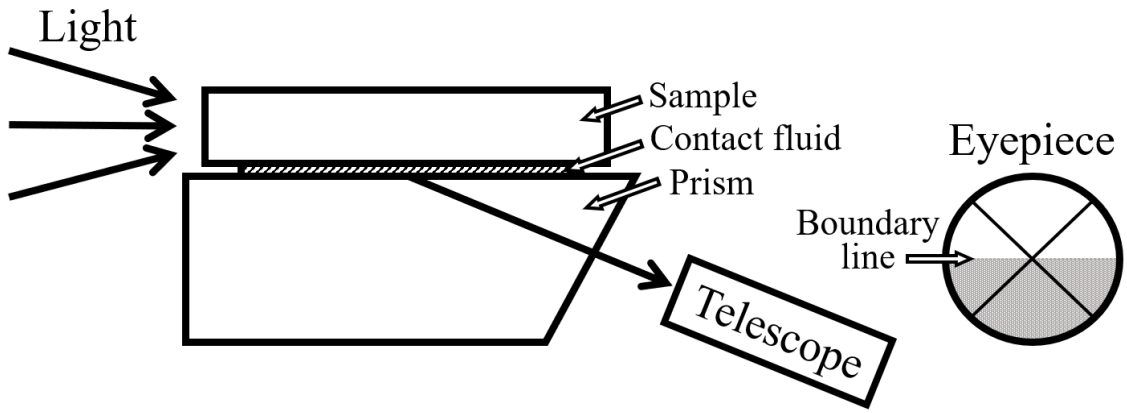

Figure 3.1: Simplified Abbe refractometer experimental geometry and the view looking through the telescope eyepiece

3.6 X-Ray Diffraction

X-ray diffraction (XRD) is a characterization technique traditionally used to determine crystalline phases and purity of materials. Figure 3.2 demonstrates the elastic scattering interaction of an incident X-ray diffracting off the atomic planes (angle between them being θ) of a crystal lattice with spacing d. Most of the diffracted X-rays will cancel due to destructive interference, while a select few will add constructively. Bragg's law is the condition for the constructive interference and is given by Equation 3.7.

$$n\lambda = 2d\sin\theta \tag{3.7}$$

n being a positive integer and λ the X-ray wavelength. An XRD pattern of a crystalline material will be a set of sharp Bragg peaks with specific intensities and diffraction angles and can be used to identify the material. Though amorphous materials lack any long-range order, this technique is useful to confirm the absence of crystalline sites within glass samples as the pattern should show no characteristic sharp peaks. The diffraction patterns of the samples were acquired with the Proto AXRD Benchtop powder diffractometer, belonging to Dr. Dasog in Dalhousie University's Chemistry Department. The intensity of the diffracted X-rays are plotted against the diffraction angle 2θ at a step size of 0.0149° from 20° to 80°.

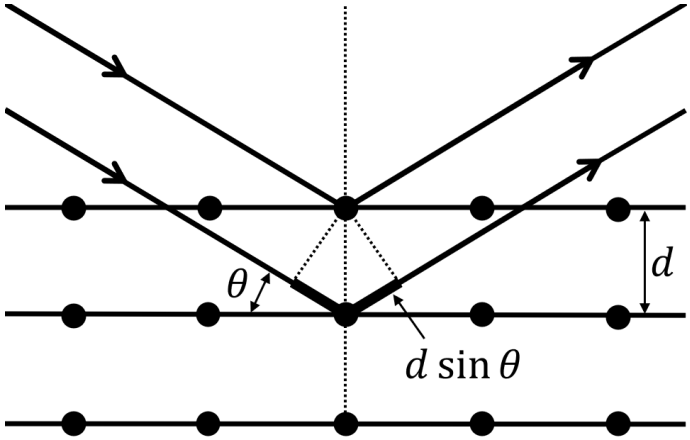

Figure 3.2: Crystalline XRD diagram

3.7 Electron Microprobe Analysis

Electron microprobe analysis (EPMA) is a technique that uses a collimated beam of electrons focused on the surface of a sample to excite characteristic X-rays so that an elemental analysis can be performed. There are two types of detection methods, one of which detects all X-ray energies simultaneously and is accordingly named

energy-dispersive spectroscopy (EDS). The later makes use of Bragg's law to separate and detect the X-rays by their wavelengths and is subsequently named wavelength-dispersive spectroscopy (WDS). Both detection methods are commonly used complementary to one another, since most electron microprobes are equipped with both, albeit they each have their advantages and disadvantages. The spectral resolution of WDS exceeds that of EDS, however an EDS spectrum is more convenient to measure and is acquired much quicker [27].

The electron source typically consists of a heated tungsten filament (2700 K), which gives the electrons enough thermal energy to overcome the potential barrier at the surface [27]. A positive voltage is applied to a metal plate with an aperture at its center to accelerate the electrons towards it. The aperture allows only the electrons with the correct alignment to pass through. Several magnetic lenses are used to focus the electron beam, making the final spot size on the order of a few μm. The important EPMA interaction between the electron beam and the sample occurs when an incident electron knocks out a core electron, leaving a vacancy. Characteristic X-rays are produced from electron transitions from higher energy shells in the atom. The photon energy is the difference in binding energy between the electron shell with the vacancy and the shell from which the electron came to fill the vacancy and is unique to the electronic structure of each atom.

ED spectrometer detectors are semiconductors with fully occupied valence bands. Incoming X-rays of all wavelengths generate electron-hole pairs by raising valence electrons to the conduction band. The spectrometer collects the entire X-ray spectrum from the sample at once in a short amount of time. However, one of the limitations of this method of detection is the use of beryllium windows that are X-ray transparent, except those from lighter elements than sodium [27]. Moreover, peak overlap between different elements is a common occurrence and some lines can go unresolved [27].

Due to the peak overlap, higher precision and peak-to-background ratio, WDS

is often used in conjunction to EDS and is preferred for lighter elements [27]. As mentioned, WDS disperses the X-rays by their wavelength in order to characterize elements in a sample. WDS functions in a similar process to X-ray diffraction by means of Bragg reflection. The X-rays emitted from the sample travel to an analytical crystal at a particular angle that satisfy Bragg's Law and reflect to the detector. Only one wavelength can be measured at a time and the position of the crystal must change to measure the X-ray wavelength of the subsequent element. Most WD spectrometers are equipped with multiple analytical crystals with different lattice spacings to cover a wide range of elemental wavelengths [27]. Since the wavelengths can only be detected one after the other, collection times for WDS far exceed those of EDS. Quantitative analysis is done by comparing the line intensities of the sample to those of standards with known compositions.

Data collection and analysis was performed by Dan MacDonald in the Earth Science Department at Dalhousie University with the JEOL JXA-8200 WD/ED combined microanalyzer. Five data points per sample were collected to account for random errors such as potential spot contaminants, Auger X-ray generation, counting errors, surface roughness, internal cracks, etc. Heavier elements within the sample can absorb the low-energy X-rays produced by lighter elements, such as boron. Matrix effect (ZAF) corrections were therefore needed to account for the effects of atomic number (Z), absorption (A) and fluorescence (F).

3.8 Raman Spectroscopy

Raman spectroscopy is a non-destructive light scattering technique used to analyze specific vibrational energies in materials. A laser is used to provide a single frequency light source, and elastically scattered light (termed Rayleigh scattering) and inelastically scattered light (Raman scattering) are produced. Most of the incident light is elastically scattered and is filtered out using a notch filter, while the Raman scattered

portion is detected and only accounts for roughly 10^{-5} of the incident light [28]. The incident light interacts with the phonons in a material, and the vibrational energy of the molecule shifts the frequency of the re-emitted photon. If the energy of the re-emitted photon is lower than the incident photon, it is considered to be Stokes (down) shifted. If the re-emitted photon is more energetic than the incident photon, then it is considered to be anti-Stokes (up) shifted. In Raman spectroscopy, it is conventional to only detect the Stokes scattering since the anti-Stokes Raman intensity is normally much smaller [28].

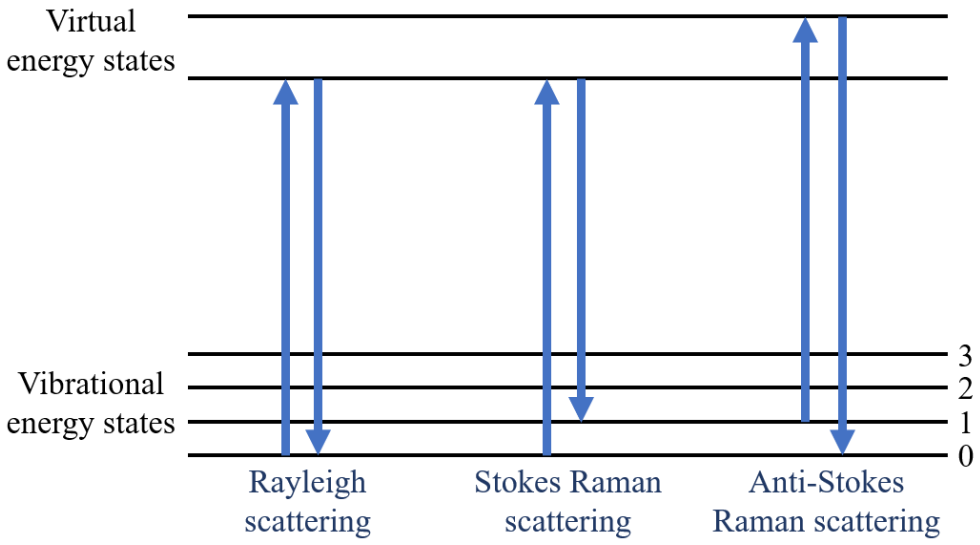

Figure 3.3: Energy-level outcomes from Rayleigh, Stokes and anti-Stokes scattering

The peaks in the Raman spectrum arise from resonances with the characteristic vibrational modes of atoms about their equilibrium positions in a material and thus can be used to fingerprint the bonding types. Vibrational modes have distinct frequencies and the intensity of the Raman effect is proportional to the polarizability of the molecules. For this reason, not all vibrational modes are Raman-active if the polarizability remained unchanged during a vibration. In the case of crystals, selection rules exist to determine whether a vibrational mode will be Raman-active based on the symmetry of the lattice [28]. Conversely, glasses lack any long-range periodicity

hence all vibrational modes appear in the Raman spectrum to some degree [29].

The high frequency region of a silicate glass sample illustrates the vibrations of NBOs about the network forming cation and has the most influence on the Raman spectrum [30]. For example, the incorporation of alkali ions to a silicate network will reduce the connectivity and increase the vibrational modes associated with NBOs in the system. It is best to systematically alter the concentration of modifier compounds in a glass network to properly analyze the Raman spectrum of a glass family. Note that glasses have broad Raman bands due to variation in bond angles and lengths, which contributes to relatively challenging analysis.

In this work, the unpolarized Raman spectra were collected using a Thermo Scientific Nicolet NXR 9650 FT-Raman Spectrometer with a 1064 nm laser. The spectra were recorded between 50 cm^{-1} and 3900 cm^{-1} and a total of 128 scans were collected per sample with a spectral resolution set to 4 cm^{-1}.

3.9 Nuclear Magnetic Resonance Spectroscopy

As the name suggests, nuclear magnetic resonance (NMR) is a spectroscopic method used to exploit nuclear magnetism to unfold local structures at given atomic sites. During an NMR experiment, a sample is subject to a strong external magnetic field, which causes the intrinsic nuclear spin energy levels to split. The separation between the spin states depends on the external applied magnetic field strength and the specific nucleus. A radio frequency (rf) pulse then excites the receptive nuclei and the resulting signal or the free-induction decay (FID) is detected. All NMR-active nuclei possess a unique resonance frequency dependant on the identity of the nucleus and its local structural environment [31]. Due to differences in experimental conditions (sensitive to the magnetic field) from laboratory to laboratory, NMR signals are recorded relative to a reference signal from a standard material [32].

The chemical shift δ is a measure of how the applied magnetic field differs from

the magnetic field that a nucleus actually experiences [33]. The electrons circulate around the nucleus, creating a small magnetic field that opposes the applied field. As such, the density of the electronic cloud dictates what is known as chemical shielding and thus demonstrates the local bonding environments [31]. The higher the electronic density, the more a nucleus is shielded from the motions of the electrons surrounding it. Stronger magnetic fields are required for nuclei with very high chemical shielding in order to have the proper energy level splitting needed to excite the nuclear spins.

The nuclear spin quantum number I is determined from the number unpaired nucleons of a given nuclide [33]. Nuclei with $I = 1/2$ have convenient magnetic properties as the charge distribution is spherical in shape and essentially behaves like a nuclear point charge [34]. On the other hand, nuclei with $I > 1/2$ have an electrical quadrupole moment from the non-spherical shape of the electrical charge distribution. Due to the lack of spherical symmetry, the electron cloud produces an electric field gradient (EFG) at the nucleus that will interact with the electric quadrupole, which is termed quadrupolar coupling. Quadrupolar nuclei have more complex NMR spectra than spin 1/2 nuclei and can cause severe line broadening and decreased resolution. There are spectroscopic techniques that improve these effects that will be discussed in the following sections.

In this dissertation, the NMR spectra were recorded with the help of Dr. Ulrike Werner-Zwanziger, solid-state NMR coordinator of the Dalhousie University NMR^3 Facility in the Chemistry Department. The Bruker Avance 16.4 T (700 MHz) and the 9.4 T (400 MHz) were the spectrometers used for the experiments.

3.9.1 Magic Angle Spinning Solid-State NMR

In order to probe the structure of glass samples, solid-state (ss) NMR procedures must be performed. Due to the inherent broadening of the NMR spectra in solids, Magic Angle Spinning (MAS) is typically employed. Powdered samples are packed

into cylindrical rotors and spun inside a superconducting magnet at the "magic angle" at varied spinning speeds. Several interactions that cause line broadening in solids are contained in the second-order Legendre polynomial $P_2(\cos\theta)$ [31].

$$P_2(\cos\theta) = \frac{1}{2}(3\cos^2\theta - 1) \tag{3.8}$$

Only when the angle between the axis of the applied magnetic field and the principle axis of the interaction θ is equal to 54.74° does this term become zero. MAS suppresses the broadening from dipole-dipole and chemical shift anisotropy, as well as first-order quadrupolar interactions from $I > 1/2$ nuclei [31].

3.9.2 Spin-Echo and CPMG Pulse Sequences

Though MAS experiments can be completed with a single rf pulse to study a material, there exist more intricate pulse sequences to further improve the resolution for nuclei with broader spectral features. Some NMR spectra are condemned with homogeneous and inhomogeneous line broadening from microscopic and macroscopic variations of the magnetic field, respectfully [34]. Spin-echo experiments were designed to overcome the distortions caused by these effects by distinguishing the homogeneous and inhomogeneous FIDs. A spin-echo pulse sequence consists of an initial $\pi/2$ excitation pulse followed by a π refocusing pulse. The time interval between the pulses and after the last pulse is denoted as τ, after which the FID is acquired.

The Carr-Purcell-Meiboom-Gill (CPMG) pulse sequence is a specific pulse-echo experiment which uses a train of π pulses to refocus the magnetization rather than a single pulse-echo. The FID is acquired over the whole train of echos, after which they are Fourier transformed and the resulting spectrum is a set of "spikelets" that resembles the ss stationary spectrum [31, 35]. This method is used to reduce significant line broadening as it improves the signal-to-noise of samples experiencing homogeneous

and inhomogeneous interactions. The lineshape of spikelets is influenced by the homogeneous interaction, and the spectral envelope is affected by the inhomogeneous interaction [31]. Shorter delay times between the π pulses may improve the overall spectral signal-to-noise but can also lead to loss of anisotropic information. That being said, longer delay times may contain the anisotropic information but will lose spectral sensitivity [36]. Thus, the spacing between echos must be chosen correctly to acquire optimal signal information and good resolution while minimizing experiment times.

WCPMG

The wideband, uniform rate and smooth truncation (WURST) CPMG pulse sequence employs the same train sequence as CPMG with the WURST pulse shape. WURST pulses have gained the acronym from their rf amplitude profiles being sausage-like in shape [37]. They were initially designed as broad-band excitation for liquid-state NMR but have been proven to have very useful applications in ss NMR. The width of the pulse can achieve fairly homogeneous excitation over a wide width, and so are typically used on nuclei with ultra-wideline NMR powder patterns. Like CPMG the resulting spectra is a set of spikelets, though due to the longer excitation pulses, a smaller number of echos is necessary, ergo shorter acquisition times.

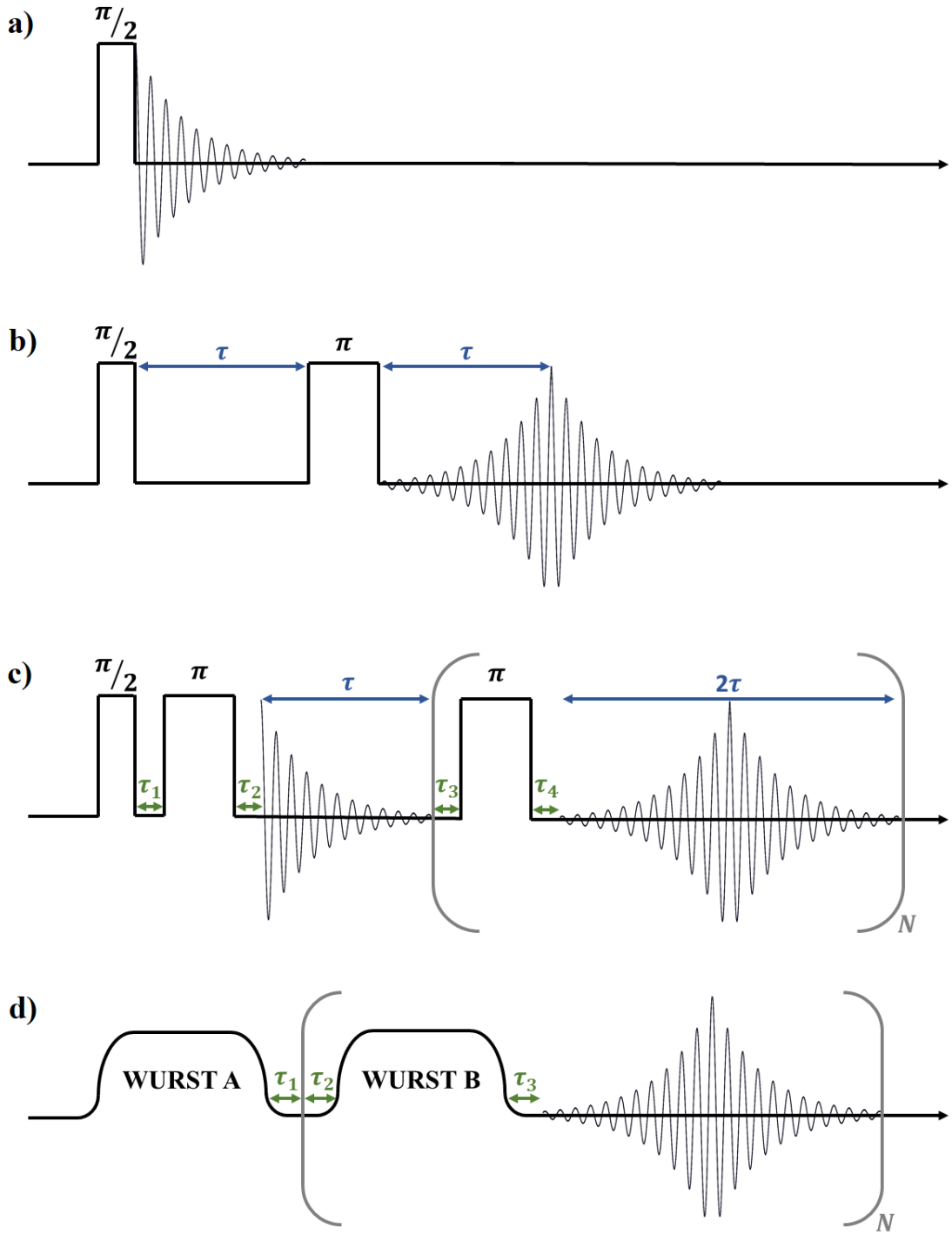

Figure 3.4: Pulse sequence diagrams for a) a simple single pulse experiment, b) a single spin-echo experiment, c) a CPMG experiment and d) a WCPMG experiment (often τ_1=τ_2=τ_3=τ_4 for CPMG and WCPMG)

3.10 Acousto-Optic Method for Measuring Photoelastic Elements

Prior to Dixon and Cohen's work, photoelastic response was routinely measured using a static stress load to induce a change in polarization of a transmitted light beam. The Dixon-Cohen method relies instead on a dynamic stress, using a transmitted acoustic wave to provide a index grating which diffracts a light beam. By varying the polarization of the incident beam relative to the propagation direction of the acoustic wave, as depicted in Figure 3.6, the independent photoelastic tensor elements can be measured.

A rf driver supplies a fixed frequency of 180 MHz to a transducer bonded to a fused quartz reference cell. The transducer uses the piezoelectric effect to convert the RF signal to eject $\sim 0.5\ \mu s$ long acoustic pulses with a repetition time of $\sim 80\ \mu s$ that diffract an optical beam incident on the reference. A sample is bonded to the reference cell using salol (phenyl salicylate) and the photoelastic tensor elements of the sample are measured relative to the reference with known tensor elements. The acoustic waves scatter the laser beam set to the Bragg angle incident on the reference or the sample. Finally, the intensity of the scattered light is detected with a photodiode connected to an oscilloscope.

Figure 3.5 a) shows the sample geometry when the optical beam traverses the reference and Figure 3.7 a) is the scattered output signal. The first pulse (I_1) in Figure 3.7 a) represents the first interaction between the optical and acoustic beams directly from the transducer. The second pulse is due to the acoustic wave being back reflected from the salol bond, and the third pulse (I_R) is due the acoustic wave travelling through the sample and reflecting from the free end of the sample and back through the bond and the quartz. Figure 3.5 b) shows the sample geometry when the optical beam traverses the sample and Figure 3.7 b) is the scattered output signal. The first pulse (I_4) in Figure 3.7 b) is due to the direct scattering from the acoustic

beam and the second pulse (I_5) is due to the acoustic beam reflecting from the free end of the sample and interacting with the optical beam. Dixon and Cohen showed that the ratio of the photoelastic tensor elements is proportional to the square root ratio of the product of the first two scattered light intensities from the sample with the product of the first pulse and the back reflected pulse from the reference.

$$\sqrt{\frac{(I_4 I_5)_{\text{Samp}}}{(I_1 I_R)_{\text{Ref}}}} = \frac{(\frac{p_{ij}^2 n^6}{\rho^2 v_a^3})_{\text{Samp}}}{(\frac{p_{ij}^2 n^6}{\rho^2 v_a^3})_{\text{Ref}}} \tag{3.9}$$

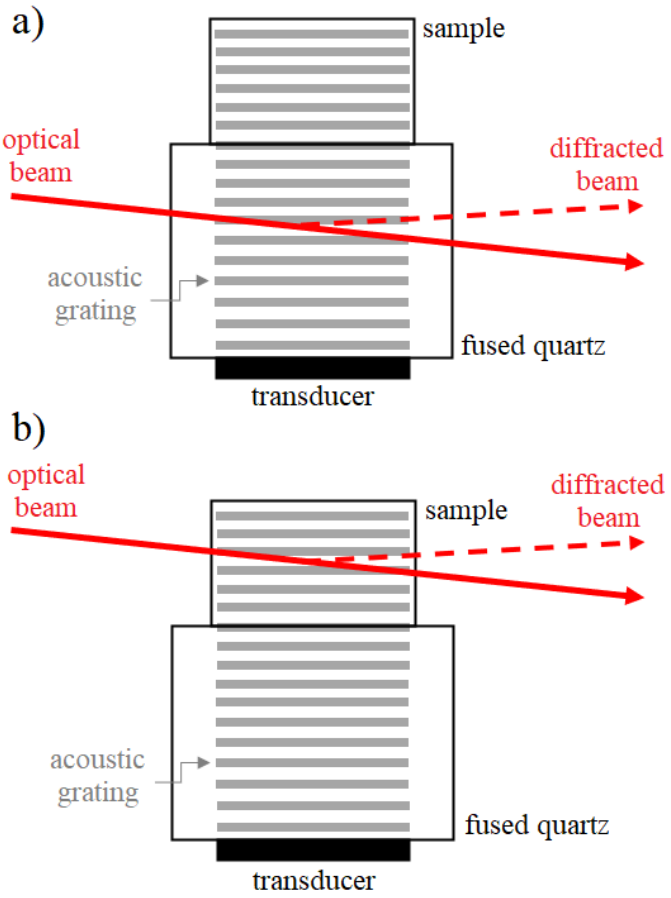

Figure 3.5: Experiment geometry for a) optical beam incident on the reference and b) optical beam incident on the sample

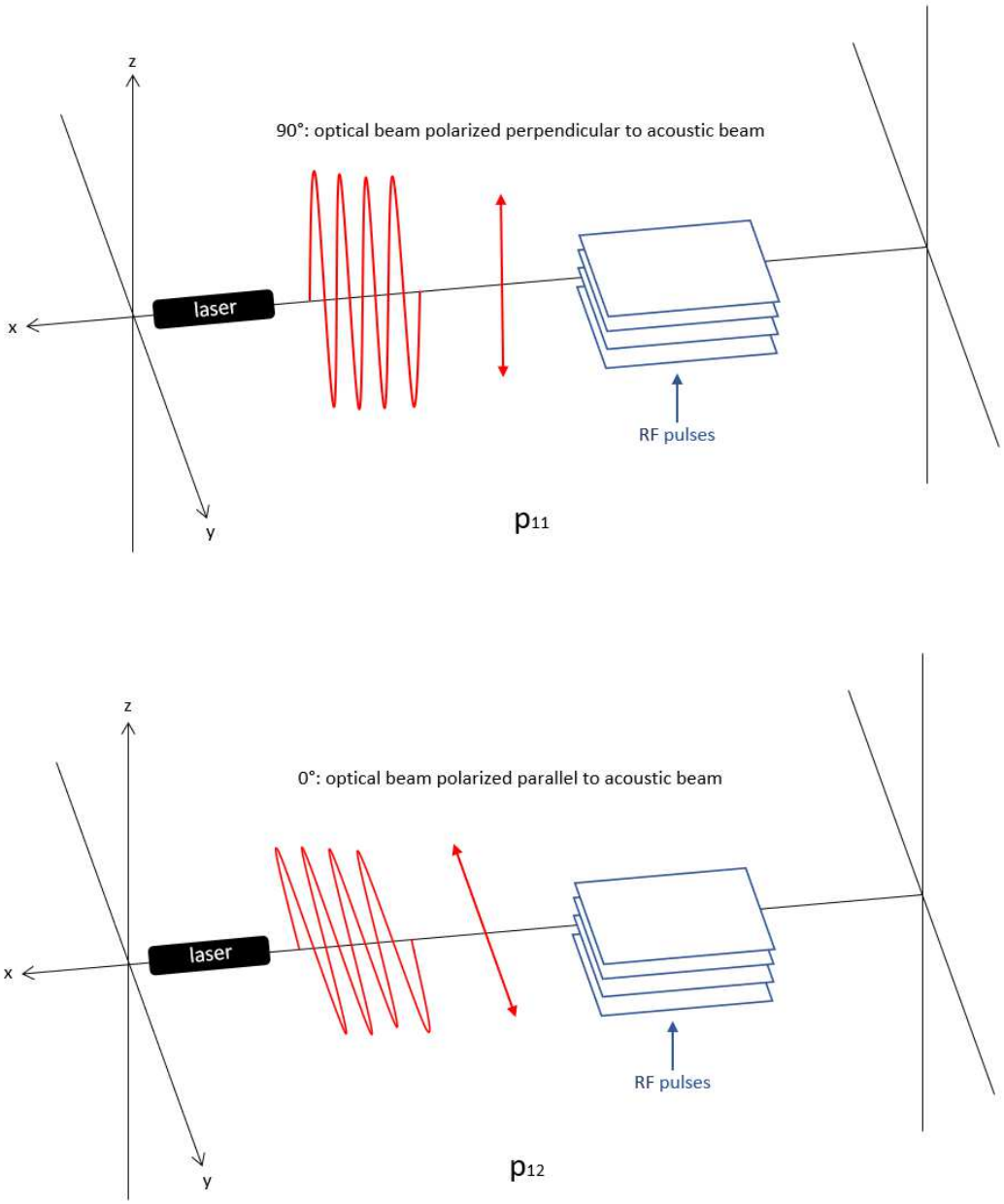

Figure 3.6: Optical polarization directions with respect to the acoustic grading to determine p_{11} and p_{12}

The acoustic pulse loses power as it travel through the solids, and it splits into transmitted and reflected parts once it reaches an interface. On account of this acoustic power loss, the intensity of the diffracted optical beam also diminishes. However, this technique eliminates the acoustic loss due to acoustic reflection (R), acoustic

transmission (T) and coupling loss from the transducer (C). Equation 3.10 lists the acoustic power loss terms as illustrated in Figure 3.8.

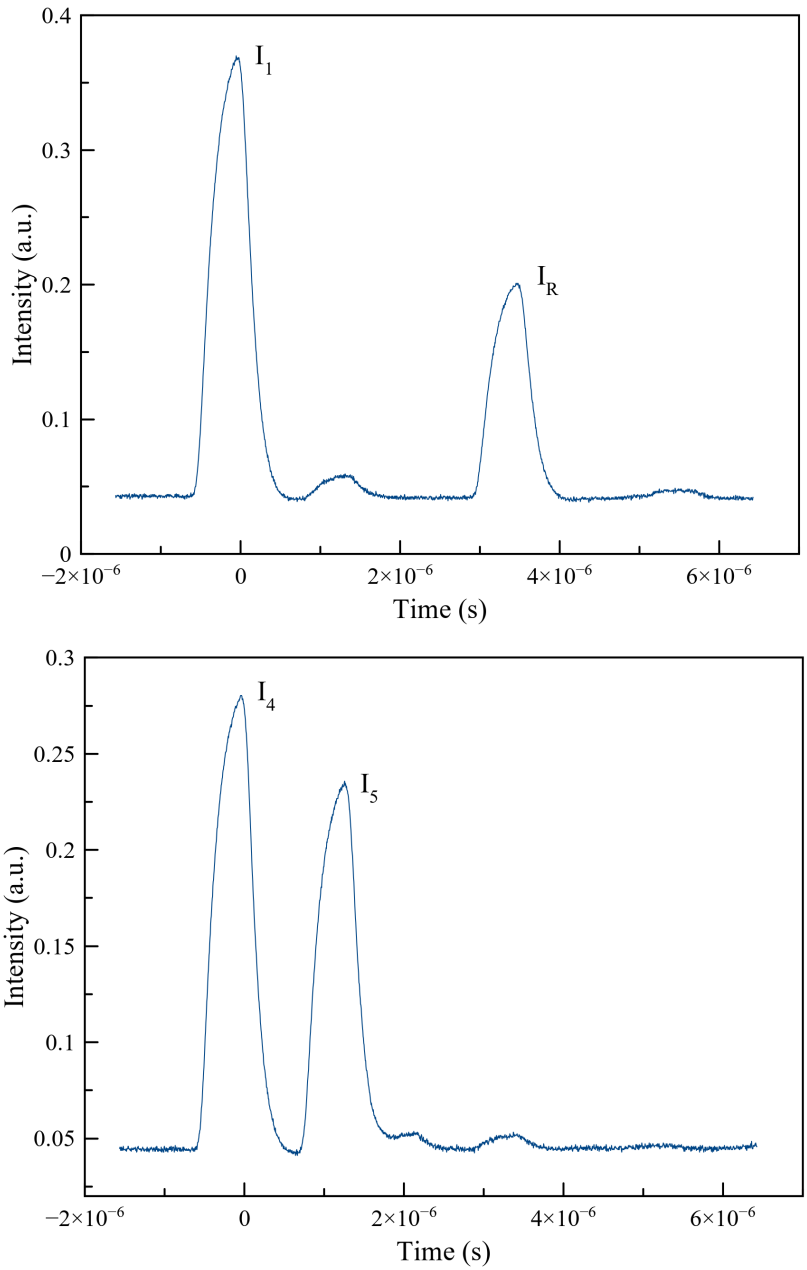

Figure 3.7: Output data example of the optical beam traversing a) the reference and b) the sample
Sample used: fused quartz

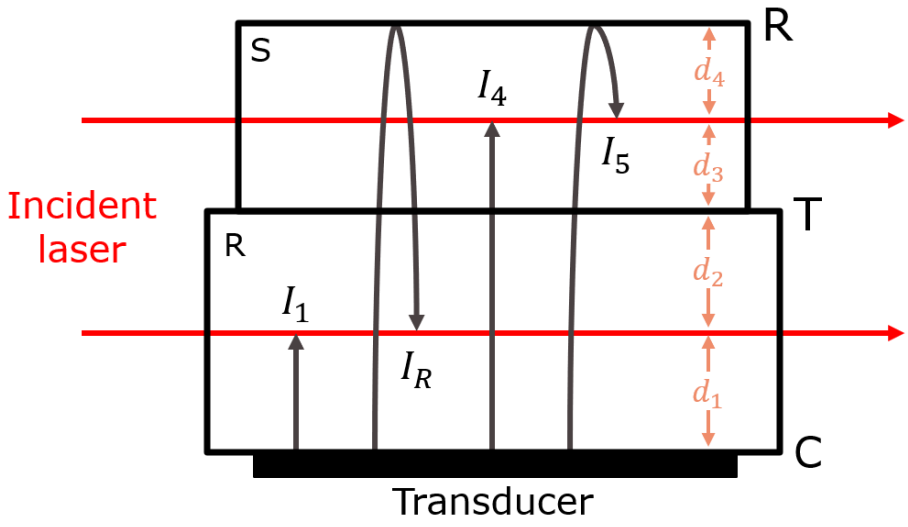

Figure 3.8: Representation of the interaction between the incident optical laser and acoustic pulse, where S is the sample and R is the reference

$$\begin{aligned} L_1 &= Cd_1 \\ L_R &= Cd_1d_2Td_3d_4Rd_4d_3Td_2 \\ L_4 &= Cd_1d_2Td_3 \\ L_5 &= Cd_1d_2Td_3d_4Rd_4 \end{aligned} \tag{3.10}$$

Taking the ratio of the product of the acoustic power loss in the sample (L_4 and L_5) with those of the reference (L_1 and L_R) yields a ratio of unity, as all the terms cancel. Thus by comparing the various signals as stated, the loss effects of transmission and the interfaces can be accounted for and the ratio expressed in Equation 3.9 used accurately to extract p_{ij} values in terms of the reference p_{ij}.

Chapter 4

Results and Discussion

4.1 Density, Sound Velocity and Mechanical Properties

The density and the longitudinal and transverse speeds of sounds were experimentally measured for the CDGM samples and are listed in Table 4.1. The table also includes the elastic moduli of the samples consisting of Poisson's ratio, Young's modulus, the shear modulus and the bulk modulus that were calculated from ρ, v_l and v_t with the Equations listed in Section 3.4.

Table 4.1: Experimentally measured and calculated mechanical properties of the CDGM samples

Sample	ρ (g/cm^3)	v_l (km/s)	v_t (km/s)	ν
H-BaK1	2.7071(8)	5.449(5)	3.243(7)	0.226(2)
H-BaK3	2.787(2)	5.827(9)	3.46(1)	0.228(2)
H-BaK8	3.1201(9)	5.31(2)	3.073(8)	0.248(3)
H-BaF2	2.772(2)	5.60(1)	3.300(8)	0.234(2)
H-ZF72A	3.5054(8)	5.829(7)	3.380(8)	0.247(2)
H-ZF72AGT	3.507(3)	5.822(4)	3.369(5)	0.248(1)

Sample	E (GPa)	G (GPa)	K (GPa)
H-BaK1	69.8(6)	28.5(1)	42.4(2)
H-BaK3	81.9(9)	33.4(2)	50.1(3)
H-BaK8	74(1)	29.5(2)	48.7(5)
H-BaF2	74.5(7)	30.2(2)	46.7(3)
H-ZF72A	99.9(9)	40.1(2)	65.7(4)
H-ZF72AGT	99.4(6)	39.8(1)	65.8(2)

There are slight variations in each of the properties between the barium crown and flint glasses. Moreover, the dense flint glasses have some interesting distinctions from

the barium samples. While the H-ZF glasses have similar speeds of sound and Poisson ratios to the H-BaK and BaF samples, the higher density largely contribute to the higher elastic moduli that these samples possess. The uncertainties of ρ, v_l and v_t were determined from standard deviation over 5 measurements and error propagation through the calculation of the elastic moduli was used for ν, E, G and K [38].

4.2 Index of Refraction

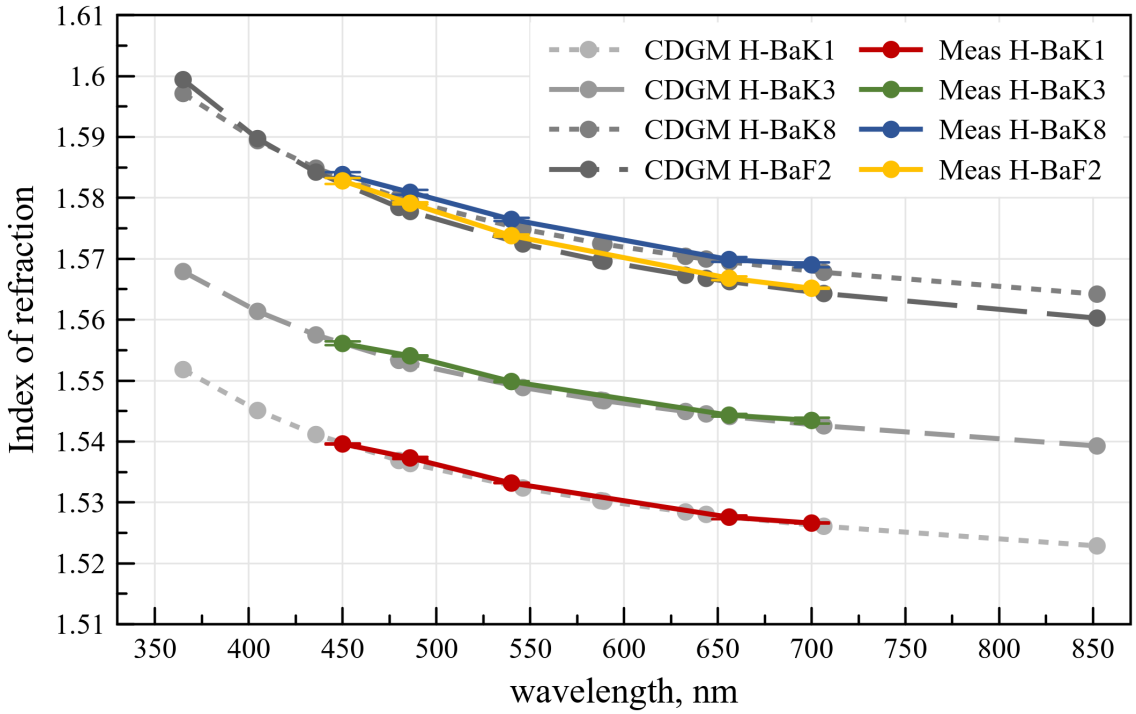

Figure 4.1: Comparing the measured (Meas) to the reported n from CDGM optical and mechanical data sheets

Figure 4.1 compares the measured refraction indices determined from the Abbe refractometer to the reported values given by CDGM. The solid coloured lines represent the collected data and the dashed grey lines represent the reported data. The measured values, which are also reported in Table 4.2, are in good agreement to those reported in the CDGM optical glass database for the H-BaK1, H-BaK3, H-BaK8 and

H-BaF2 samples [39]. The uncertainty of n was determined from standard deviation over 5 measurements at each wavelength.

Unfortunately, the index of refraction could not be measured for the H-ZF72A and H-ZF72AGT samples using the refractometer as the index of refraction of the contact fluid ($n_{589.29}$=1.8000(5)) did not surpass that of the samples (n = 1.91826 to 2.019780 from λ = 706.52 to 404.66 nm respectively). The experiment therefore did not meet the requirement of total internal reflection necessary to measure their refraction indices. The high apparent index of refraction is surprising as the MSDS reports these samples as titanium containing alkali phosphate glasses. Relatively similar glasses in literature report n in the range of 1.62-1.65 [40].

Table 4.2: Measured n of the barium crown and flint CDGM glasses at various wavelengths

Sample	λ (nm)	n	Sample	λ (nm)	n
H-BaK1	450	1.53960(7)	**H-BaK8**	450	1.5838(4)
	486	1.5373(2)		486	1.5809(4)
	540	1.53318(4)		540	1.5765(3)
	656	1.5278(3)		656	1.5699(4)
	700	1.5266(1)		700	1.5690(4)
H-BaK3	450	1.5561(3)	**H-BaF2**	450	1.5828(5)
	486	1.5541(1)		486	1.5791(2)
	540	1.5499(1)		540	1.5738(2)
	656	1.5443(2)		656	1.5668(3)
	700	1.5435(5)		700	1.5652(1)

Some information about the glasses can be extracted from the index of refraction data, by fitting them to a physically motivated model. An empirical model that is often used is the Sellmeier model, which for a single term has the form [41]

$$n(\lambda)^2 = 1 + \frac{B\lambda^2}{\lambda^2 - C}. \tag{4.1}$$

This form is essentially equivalent to the Drude-Lorentz model of a driven, harmonically bound charged particle [17, 42]. This model shows divergence at wavelength

$\lambda_0^2 = C$, with dimensionless coupling B. Wemple and DiDomenico pushed this analogy further in solids, treating an insulator or semiconductor as a collection of oscillators, with the index of refraction given by averaged constants in the following form [43]:

$$n(E)^2 - 1 = \frac{E_d/E_0}{1 - (E/E_0)^2}. \tag{4.2}$$

Here E_0 is the energy at which the index of refraction diverges, and should be roughly the band gap, while E_d encodes the intraband transition energies. Again, this form is just a recasting of the Sellmeier formula, but now with some physical significance attached to the fitting parameters.

The data for the index of refraction was fit to the Wemple-DiDomenico model in the more convenient form

$$\frac{1}{n^2 - 1} = \frac{E_0^2 - E^2}{E_d E_0} \tag{4.3}$$

as shown in Figure 4.2.

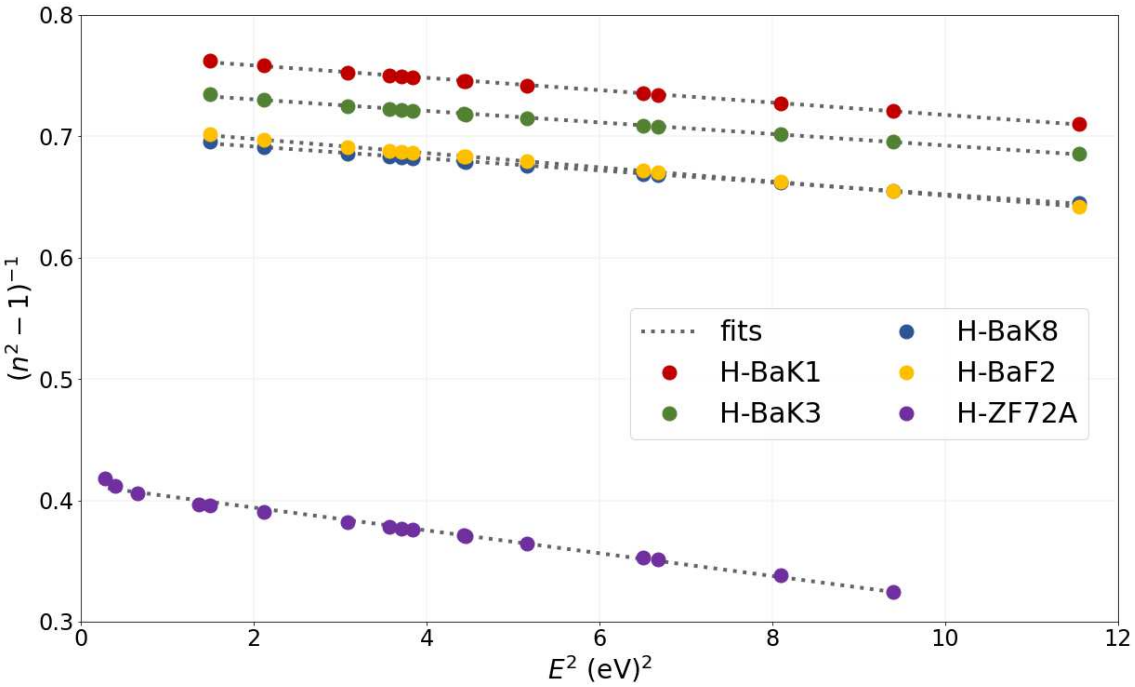

Figure 4.2: Fitted relationship of $(n^2 - 1)^{-1}$ with respect to E^2 of the CDGM glasses

Table 4.3: Wemple-DiDomenico parameters of the CDGM glasses

Sample	E_d (eV)	E_0 (eV)
H-BaK1	15.97	12.28
H-BaK3	16.87	12.48
H-BaK8	17.00	11.92
H-BaF2	15.53	11.01
H-ZF72A	16.05	6.63

The resulting coefficients for the samples are given in Table 4.3. Wemple and DiDomenico had made the empirical observation of E_d being influenced by the structure, chemistry and ionicity of the crystal and is independent of the band gap energy [43]. E_d essentially acts as an interband strength parameter and remains relatively consistent across all CDGM samples, suggesting they possess similar ionicities. In addition, the oscillator energy gives an approximation for the average energy gap. E_0 is roughly constant between the silicate H-BaK and H-BaF samples, while the E_0 of H-ZF samples is notably smaller, about half of the silicates. This model is thus useful in distinguishing a band gap difference between the CDGM samples which will prove to be beneficial in a subsequent section.

4.3 X-ray Diffraction

Figure 4.3 presents the powder XRD patterns of the CDGM samples. The plot confirms the amorphous behaviour of the glasses as the spectra lack any sharp peaks that are associated with crystalline sites.

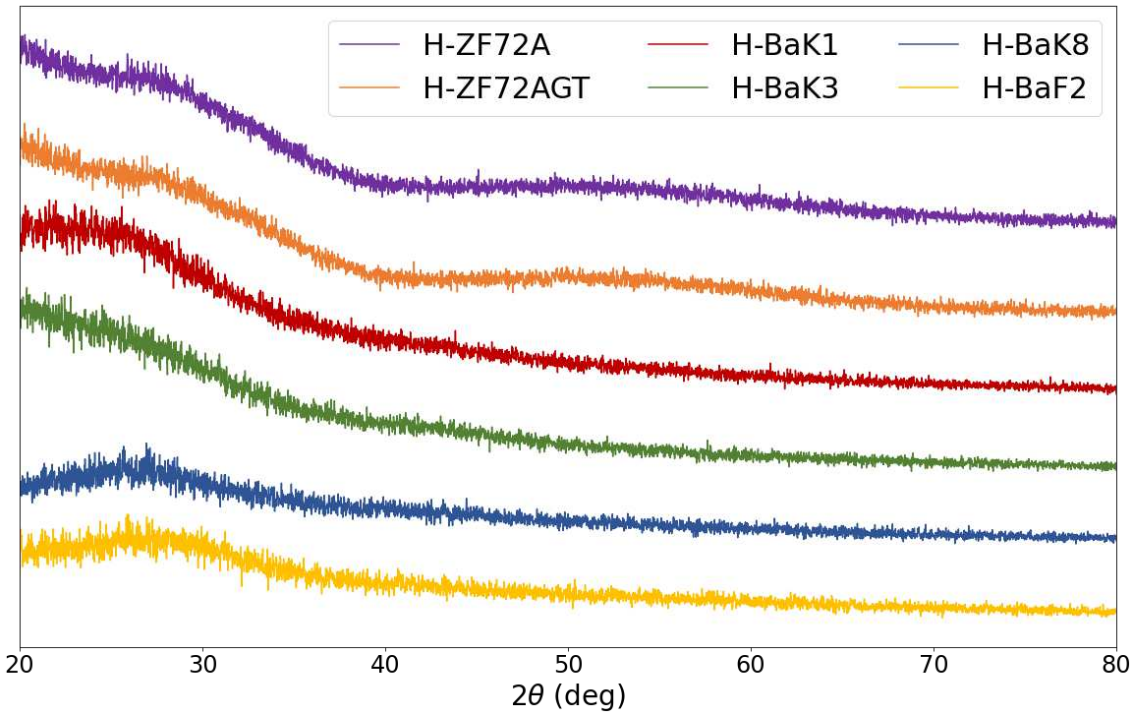

Figure 4.3: XRD patterns of the CDGM samples (using Cu K-α source)

.

4.4 Wavelength Dispersive Spectroscopy

Figure 4.4 compares the estimated weight percent compositions reported in the CDGM safety data sheets to the WDS measured compositions. Most of the CDGM values are given over a range of 10% and only the sum of the maximum values of each component results in a total of 100%. It was determined that the precision of the reports were not satisfactory for this work, hence the compositional WDS measurements.

The samples were initially analyzed with EDS as a tool to identify any elements not reported in the MSDS. Unfortunately EDS was not reliable for quantitative analysis, but it proved useful to collect elemental information before analyzing the samples

with WDS. Interestingly, Na and K were determined to be likely present in the H-BaK and H-BaF samples and Nb, K and possibly B were determined to be likely present in the H-ZF samples. These elements were therefore added to the WDS files in addition to those reported by CDGM.

The measured amounts of SiO_2 and BaO in the H-BaK and H-BaF samples from the WDS data agreed with those reported. The measured ZnO in the samples are below (1.6-8.6 wt%) what was reported. Only trace amounts of Sb_3O_3 were measured, likely due to this being a fining agent and only minute amounts (0.1-1 wt%) are generally needed for it to be effective at removing bubbles [7]. Ti was also detected in the samples that did not report it (H-BaK samples only). Falsely detected Ti is common in samples that also contain Ba as there is peak overlap between these two elements and even occurs in the barite standard. This was corrected for in post-processing. Additionally, the amount of B_2O_3 can be underestimated in the samples. As briefly mentioned in Section 3.7, the weak X-rays generated by boron are commonly absorbed by heavier elements present in the sample and by the detector window itself, resulting in low signal intensity [44]. Table 4.4 lists the total average weight % oxide that had been reported from the WDS measurements. The H-BaK samples are missing 4-5% and the H-BaF2 sample is missing 9% off of the total 100% one would expect to have. Typically, "good" agreement occurs in the range of a total of 98.5-100.5 wt% for glasses. That being said, undercounting can occur if the stoichiometry of a particular compound differs (eg.. BaO and BaO_2 are present and only BaO is accounted for) [45]. WDS confirmed the presence of K_2O and Na_2O detected from EDS. These are alkali metals that are commonly added to glasses as network modifiers. Na and K atoms can cause some trouble in WDS as they are easily ionized and can move away from the beam center. The effect of mobile alkali metal ions can cause significant reductions in the total concentrations (losses of over 50% of sodium counts have been reported for silicate glasses in literature) [46]. For these

reasons, the elemental analysis by WDS for these particular samples can be taken with a grain of salt due the experimental complications that have been discussed.

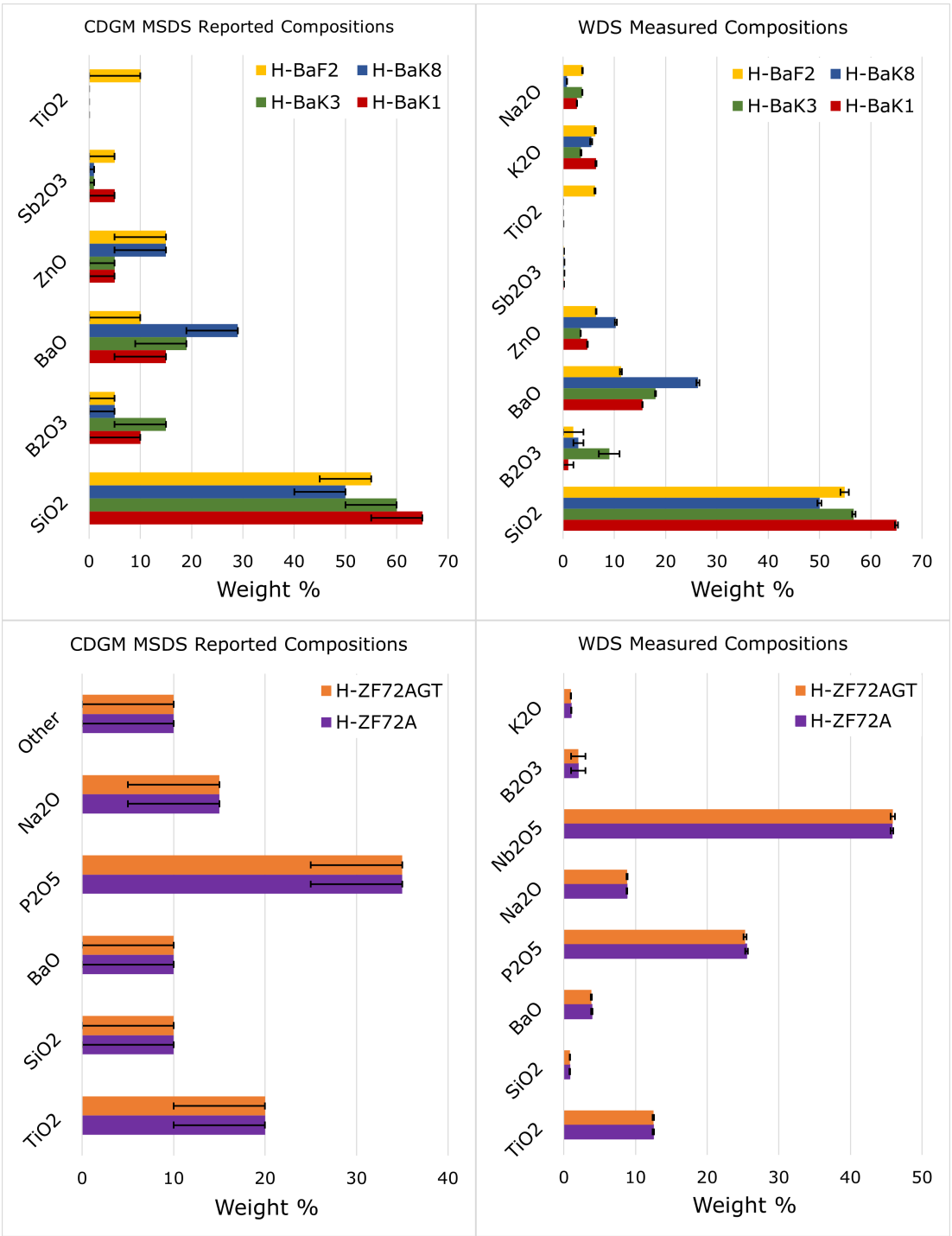

Figure 4.4: Weight percent oxide reported in the CDGM MSDS (each component with a range of 5-10%) compared to those measured with WDS

Table 4.4: Total average wt% oxide of the CDGM samples measured by WDS

Sample	Average total wt%
H-BaK1	95(1)
H-BaK3	95(2)
H-BaK8	96(1)
H-BaF2	91(2)
H-ZF72A	100(1)
H-ZF72AGT	100.5(9)

In spite of the H-BaK and H-BaF samples showing relatively comparable compositions to what was reported, the H-ZF glasses presented some wholly unexpected results. All of measured concentrations of TiO_2, SiO_2, BaO, P_2O_5 and Na_2O were well below the top of the reported range for those components. This implies a rather large portion of the sample needs to be accounted for by something else present in the samples. From the MSDS of these samples, P_2O_5 was assumed to be the main network former. Yet, the WDS data paints a different narrative. A startling ∼45 wt% of Nb_2O_5, while only ∼25 wt% P_2O_5 was measured. That being said, the total average weight percent of the H-ZF glasses are judged to be reliable, as they fall within the range of 98.5-100.5 wt% [45].

4.5 Raman Spectroscopy Results

4.5.1 H-BaK and H-BaF CDGM Samples

The Raman spectra of the glasses are divided into two regions: the low frequency (LF) region (between 400 and 700 cm^{-1}) and the high frequency (HF) region (between 800-1200 cm^{-1}). Raman bands in the LF region represent symmetric stretching modes of Si–O–Si and vibrationally isolated ring configurations in the network [47, 30]. For pure fused silica, the dominant features lie in the LF region are associated with strongly polarized vibrational modes, but these features can become difficult to discern for alkali-silicate glasses [47]. The dominant features of alkali-silicate glasses

occur in the HF region. Information on the Q-species of these glasses can be determined in this region, which represent symmetric stretching modes of O–Si–O [47, 48]. The raw Raman spectra of the H-BaK and H-BaF glasses are compared in Figure 4.5 and the associated band assignments are summarized in Table 4.5.

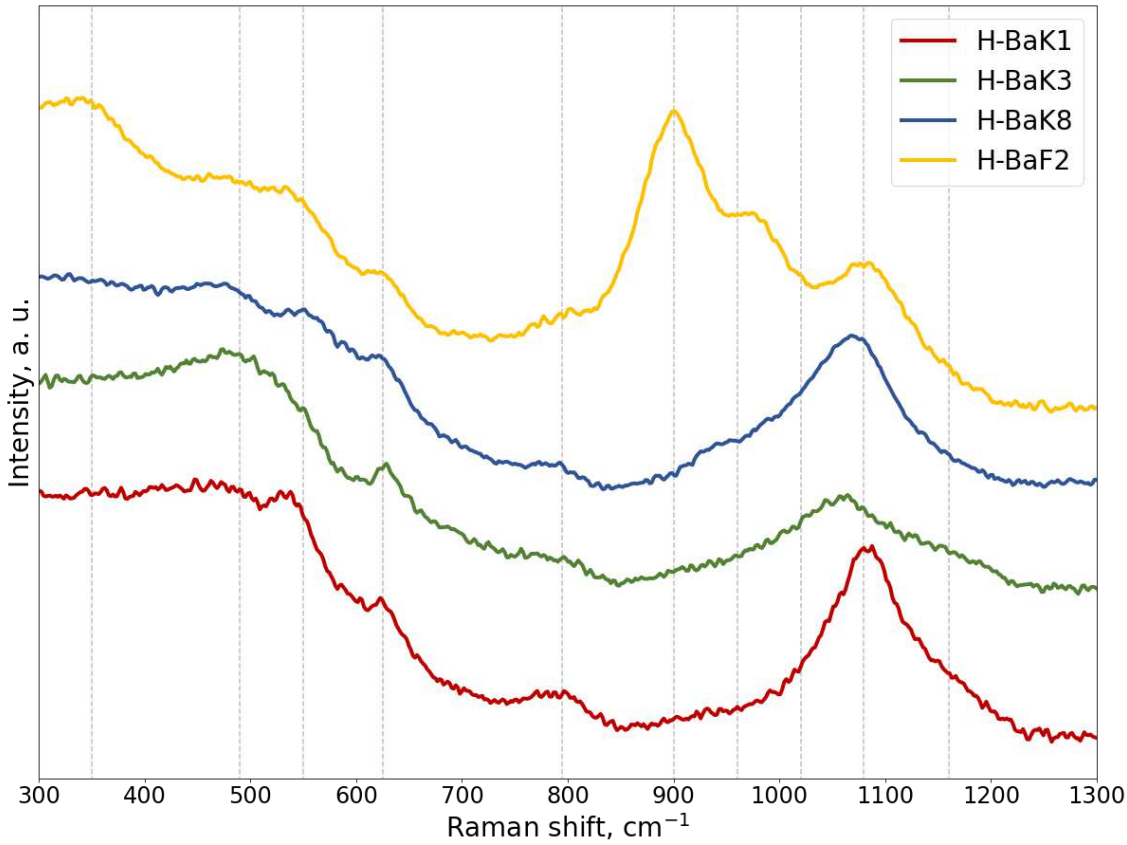

Figure 4.5: Raw Raman spectra of the H-BaK and H-BaF CDGM glasses (vertically offset for clarity)

The LF bands become difficult to distinguish with higher alkali inclusions as the sharp bands at 430, 490 and 600 cm^{-1} of pure SiO_2 shift in intensity and frequencies. The 430 cm^{-1} has been associated with the fully polymerized silica structures, which explains the decreased intensity of this band as more NBOs form [47]. The 490 cm^{-1} has been shown to migrate to higher frequencies as alkali concentrations increase [47, 49]. The frequency shift of this band has also been shown to depends on the

size of the alkali cations, as smaller cations cause higher shifts [47]. The 600 cm^{-1} band can shift to higher frequencies as more NBO per Si form in the network [48]. The intensity of this band can change significantly with the type of alkali present, as heavier alkali have stronger bands [47]. Lastly, it is not uncommon to find peaks around 350 cm^{-1} for alkali silicate glasses, although the peak assignments in literature are not well-defined [48, 50]. This is a broad feature that seems to only occur for the H-BaF2 sample.

Table 4.5: Raman shifts (RS) and peak assignments for the H-BaK and H-BaF CDGM glasses

RS (cm^{-1})	Vibrational mode	Q-species
480 - 490	$(Si–O–Si)_s$	Q^4 [47]
540 - 565	Defect & 4-membered ring structures [51]	
625 - 635	Defect & 3-membered ring structures [48, 47]	
790 - 815	Si motions in tetrahedral O cage [52]	
900	$(O\text{-}Ti\text{-}O)_s$ stretching [53]	
910 - 980	$(O–Si–O)_s$	Q^2 [52]
980 - 1020	$(O–Si–O)_s$	Q^4 [52]
1055 - 1085	$(O–Si–O)_s$	Q^3 [52]
1130 - 1155	$(O–Si–O)_s$	$Q^{3'}$ [52]

Most of the peaks found in the HF region are related to localized O–Si–O stretching modes within silica tetrahedrons. For this reason, the Q-species distribution can be identified for silicate glasses. The exception to this is the peak appearing at ~800 cm^{-1}, as this peak pertains to isolated vibrations of Si atoms in a tetrahedral cage of O atoms. The main band present in the H-BaK samples at ~1070 cm^{-1} is known to represent symmetric stretching of Q^3 units and is also accompanied by a higher frequency shoulder at around 1150 cm^{-1}. On the lower frequency side of this main peak is the symmetric stretching mode of Q^4 units at around 1000 cm^{-1}, followed by that of Q^2 units at around 930 cm^{-1} [52].

Table 4.6: Peak fitting parameters for the H-BaK and H-BaF CDGM glasses. The peak locations are given by the Raman shift (RS) along with their half-width-half-maximum (HWHM), normalized intensities and percent area of the individual peak relative to the total area of all peaks.

H-BaK1				**H-BaK3**			
RS (cm^{-1})	HWHM (cm^{-1})	Norm. Intensity	% Area	RS (cm^{-1})	HWHM (cm^{-1})	Norm. Intensity	% Area
793	27	0.12	5	791	27	0.12	4
940	45	0.14	10	913	35	0.17	7
1018	36	0.27	15	983	42	0.38	19
1081	35	0.87	46	1058	43	0.87	46
1151	46	0.34	24	1143	48	0.41	24
H-BaK8				**H-BaF2**			
789	20	0.07	2	808	39	0.13	6
-	-	-	-	900	38	0.97	43
948	50	0.31	21	976	30	0.52	18
1021	41	0.44	24	1020	30	0.21	7
1073	35	0.74	35	1084	40	0.49	23
1132	49	0.28	18	1154	31	0.08	3

The baseline were subtracted using the *UnivariateSpline* function from the *Rampy* library, and the intensities of the spectra were normalized to 1. Five Gaussians and the Levenber-Marquart algorithm are used to fit the spectra from 700 to 1300 cm^{-1}. Figure 4.6 illustrates the fits and the fitting parameters and percent area of the peaks relative to the total are given in Table 4.6. The goodness of fit were determined by $R^2 \geqslant 0.99$ (fraction of total residual variance) for each. The half-width-half-maximums (HWHM) of the peaks were constrained to be $\leqslant$50 cm^{-1} as per literature [48].

The shapes of the HF spectral envelopes are akin between the H-BaK samples with only slight differences occurring in the shift, HWHM and peak heights. The shape is also consistent with high-silica alkali-silicate glasses found in literature with 75-85 mol% SiO_2 [48, 47]. This also coincides with the measured EPMA compositions. The percent area of the H-BaK1 and H-BaK3 samples was highest for Q^3 units as they made up about 73% of the total area under the Q-species envelope, while only about

18% Q^4 and 9% Q^2 were present for both. The H-BaK8 sample had a modest change in % area distribution with about 54% Q^3, 24% Q^4 and 21% Q^2. It is important to note that the % area under the Gaussians do not directly correspond to the amount of respective Q^n units. A semi-quantitative distribution of Q^n can be determined from the spectra if the normalized Raman cross sections for each Q^n is determined.

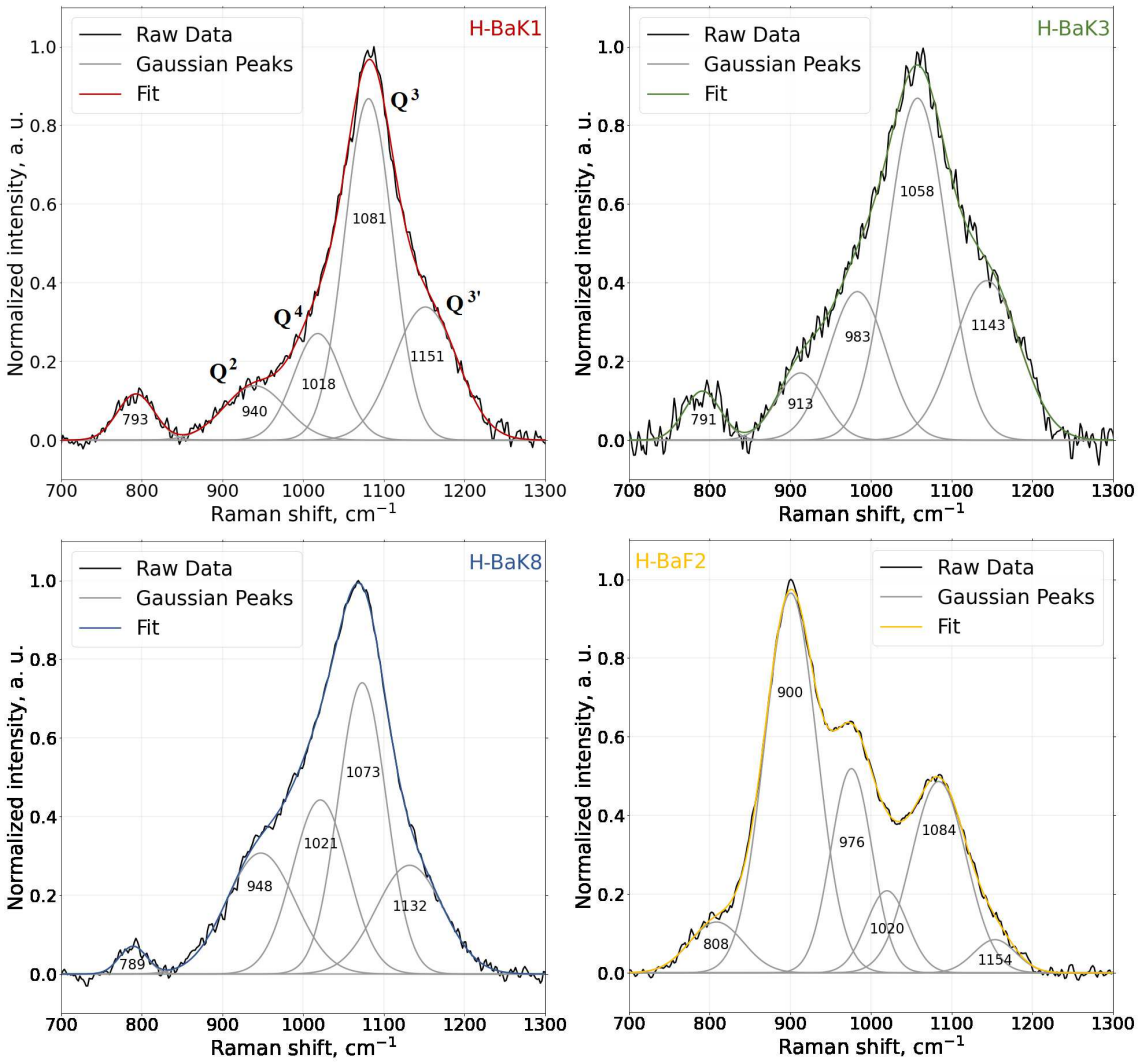

Figure 4.6: Fitted HF Raman spectra of all H-BaK and H-BaF CDGM glasses

The obvious outlier is that of the H-BaF2 sample, showing dramatic variation in peak heights compared to the H-BaK samples. The compositional EPMA data

confirms the presence of Ti in this sample, which is the primary difference distinguishing it from the crown samples. The overall shape of the HF spectrum is similar to that of an alkali-silicate glass with ∼7 wt% TiO_2 in literature [53]. Additionally, the inclusion of TiO_2 in a silicate glasses has shown evidence to decrease the degree of silicate network polymerization, as well as rapid growth in a new band at 900 cm^{-1} associated with symmetric O–Ti–O stretching [48, 53]. This would also explain the perceived decrease of the Q^4 band and increase of the Q^2 band.

4.5.2 H-ZF CDGM Samples

Table 4.7: Raman shifts (RS) and peak assignments for the H-ZF CDGM glasses

RS (cm^{-1})	Vibrational mode
260	O–P–O + O–Nb–O bending [54, 55]
440	O–P–O + O–Nb–O bending [54, 55, 56]
630	Nb–O stretching + O–P–O bending [54, 55]
730	$(P–O–P)_s$ [55]
820	Nb–O–Nb stretching or bending [55, 56]
890	isolated $(Nb–O_6)_s$ stretching and (Nb–O–P–Nb–O) bending [54, 55, 56]
985	$(O–P–O)_s$ stretching (Q^0) [54, 56]
1050	$(O–P–O)_s$ stretching (Q^1) [54, 56]
1120	$(O–P–O)_s$ [54]
1155	$(O–P–O)_s$ stretching (Q^2) [55, 56]

Figure 4.7 shows the baseline corrected Raman spectra of the H-ZF72A and H-ZF72AGT samples. Due to the immensely broad HF Raman spectra of the H-ZF samples, fits could not be completed with reasonable statistical certainty. They can, however, be compared to samples with similar composition. S. Chenu in the Zwanziger research group had studied the structure and properties using both Raman and NMR spectroscopy of $NaPO_3$0-ZnO-Nb_2O_5-Al_2O_3 glasses with varying mol% concentrations of Na_2O, P_2O_5, ZnO and Nb_2O_5 [57]. The shape of the HF spectral envelope most resembles that of the 55$NaPO_3$-20ZnO-20Nb_2O_5-5Al_2O_3 in their study. Interestingly, this sample contained the highest mol% concentration of Nb_2O_5 of these samples.

Table 4.7 summarizes the Raman mode assignments and their respective locations. The Raman bands are mostly the result of P–O and Nb–O bending and stretching vibrations.

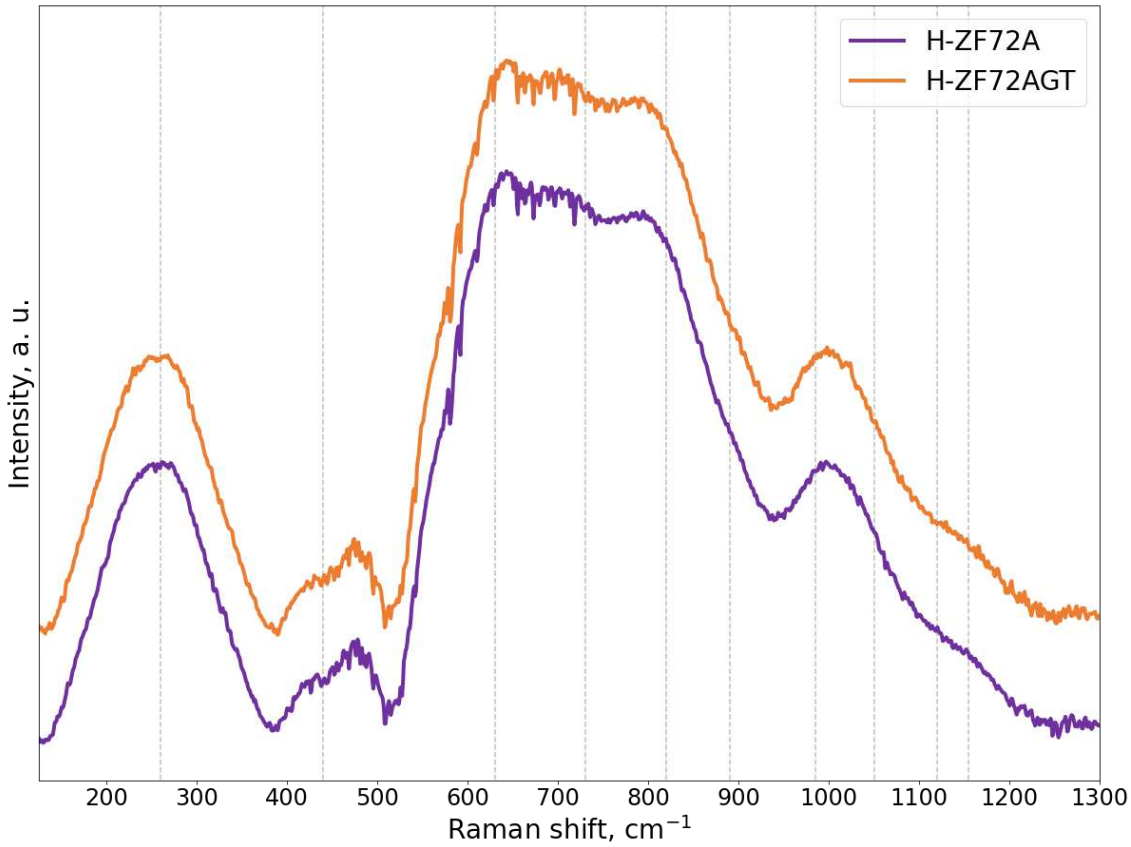

Figure 4.7: Raw Raman spectra of the H-ZF CDGM glasses (vertically offset for clarity) where the vertical lines correspond to the Raman shifts listed in Table 4.7

4.6 NMR Spectroscopy Results

4.6.1 ^{11}B NMR on H-BaK and H-BaF Glasses

Figure 4.8 show the results of single-pulse ^{11}B MAS-NMR experiments for the H-BaK and H-BaF samples, spinning at 20 kHz in a 16.4 T magnet.

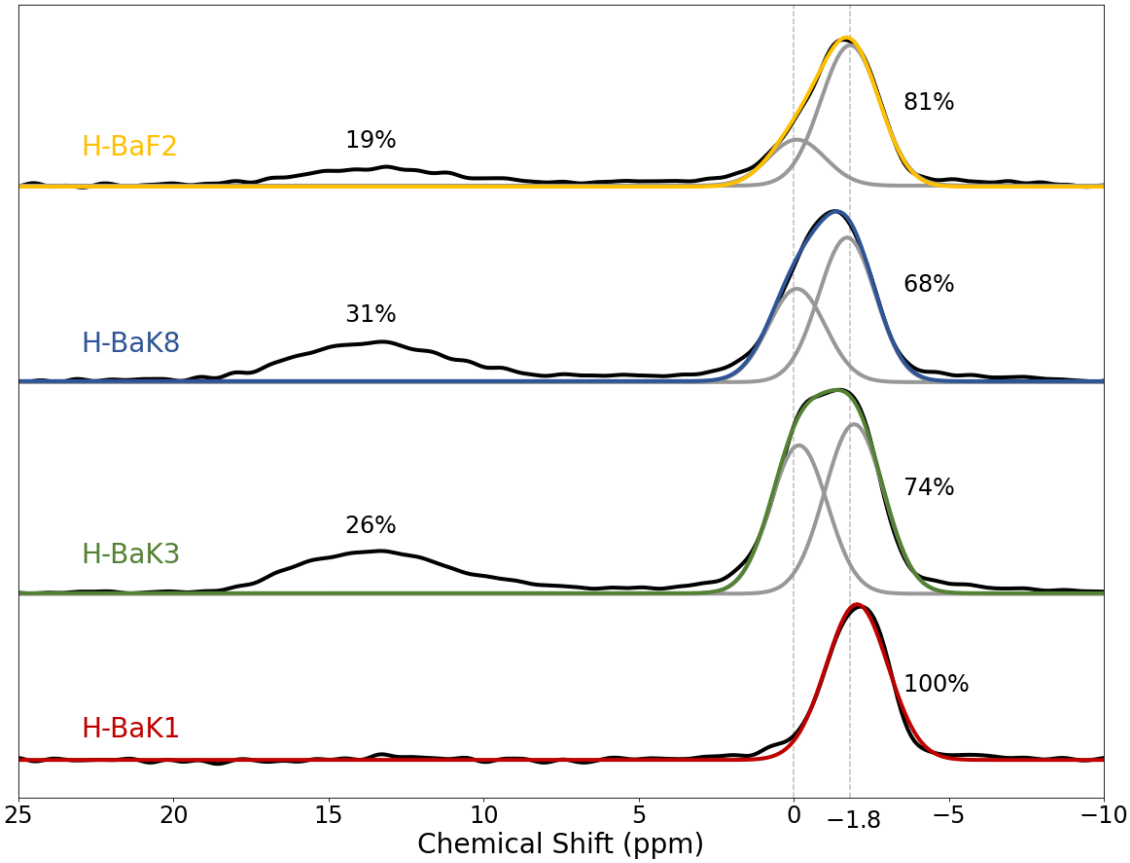

Figure 4.8: ^{11}B MAS-NMR spectra of the H-BaK and H-BaF CDGM glasses

All, but H-BaK1 exhibit the presence of two sites. The peak on the left at around 14 ppm is assigned to $^{[3]}$B due to second order quadrupolar broadening and the location of the peak agrees with literature chemical shift assignments [31, 58, 59]. The site on the right at around -1.7 ppm is assigned to $^{[4]}$B. The presence of a shoulder on the high-frequency edge of four-coordinate boron peak of H-BaK3, H-BaK8 and H-BaF2 glasses indicates that there is more than one $^{[4]}$B environment in the glass network as they were fitted with two Gaussians (using Dmfit program [60]). The spectra have been deconvoluted to find the relative concentrations of $^{[3]}$B and $^{[4]}$B in the samples. The area under each peak is proportional to the relative quantity of each species. The fraction of four-coordinate boron N_4 was determined for the samples using Equation 4.4 and is listed in Table 4.8.

$$N_4 = \frac{^{[4]}\mathrm{B}}{^{[4]}\mathrm{B} + {}^{[3]}\mathrm{B}} \tag{4.4}$$

Table 4.8: ^{11}B MAS-NMR Gaussian peak fitting parameters for the $^{[4]}$B sites, relative % area of each site to total envelope and N_4 fraction of the H-BaK and H-BaF samples

Sample	$^{[4]}$B(4Si) δ (ppm)	FWHM (ppm)	Relative % Area	$^{[4]}$B(3Si) δ (ppm)	FWHM (ppm)	Relative % Area	N_4 fraction
H-BaK1	-2.04	2.35	100	-	-	0	1
H-BaK3	-1.95	2.23	53	-0.17	2.15	47	0.74
H-BaK8	-1.72	2.15	61	-0.1	2.15	39	0.69
H-BaF2	-1.82	2.23	76	-0.1	2.15	24	0.81

Solid-state ^{11}B MAS-NMR experiments on Pyrex® glass, which typically contain a mixture of SiO_2 (in high amounts), B_2O_3, Al_2O_3 and Na_2O, have been conducted to study the structural tendencies of boron that form within the glass network. The glasses exhibit two overlapping resonances associated with the $^{[3]}$B chemical shift, as well as two additional overlapping resonances associated with the $^{[4]}$B chemical shift [58]. The $^{[3]}$B site is likely composed of symmetric ring units (around 17 ppm) and asymmetric non-ring units probably bonded to a Si neighbour (around 13 ppm). Unfortunately, these are not resolved given the low intensity of the three-coordinate B peak. The $^{[4]}$B site is likely composed of boron linked to three Si neighbours (around 0 ppm) and boron linked to four Si neighbours (around -2 ppm) [61].

Figure 4.9 plots the relationship between the measured mol% of SiO_2 to the fraction of $^{[3]}$B in the samples. H-BaK1 seemingly has no $^{[3]}$B, only $^{[4]}$B, while also being the sample with the highest mol% concentration of SiO_2 and the lowest concentration of B_2O_3. Additionally, the spectrum shows evidence of the sample having only the $^{[4]}$B site assigned to boron linked to four Si atoms.

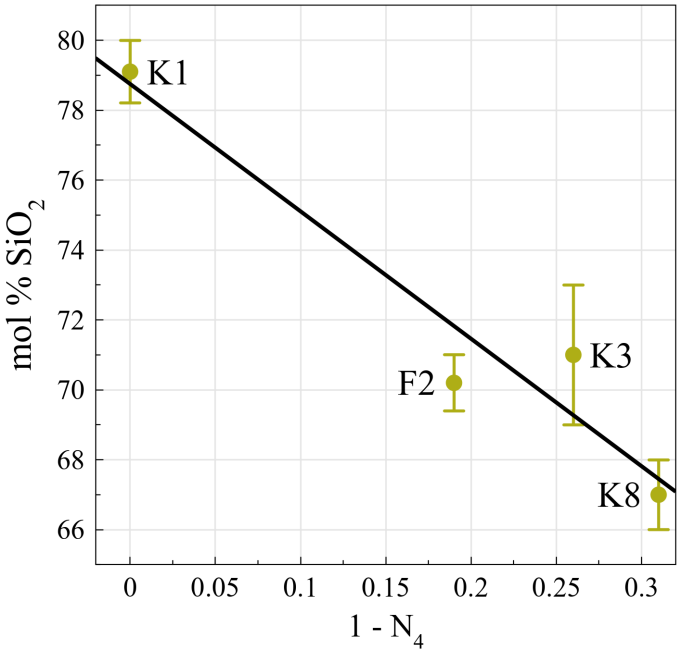

Figure 4.9: Relationship between mol% SiO_2 to 1 - N_4 (fraction of $^{[3]}B$)

4.6.2 ^{29}Si NMR on H-BaK and H-BaF Glasses

Not only does Raman spectroscopy uncover information on the distribution of Si Q-species in silicate glasses, NMR spectroscopy can do the same [62]. Figure 4.10 shows the ^{29}Si spectra obtained from MAS-NMR acquired with CPMG pulse sequence experiments of the H-BaK and H-BaF samples spinning at 5 kHz in a 9.4 T magnet. The spectra show a single broad resonance from about -72 to -120 ppm. The degree of network polymerization dictates the chemical shielding about silicate units, and therefore the chemical shift. More shielded silicate units have a higher degree of network polymerization and will have more negative chemical shifts than silicate units with less connectivity and more NBOs [31]. The range of chemical shift of Q^4, Q^3 and Q^2 units are highlighted in Figure 4.10. The strong overlap between the Q-species regions is the justification for fitting the spectra with a single Gaussian to determine the average central chemical shift of the individual samples. The fitting

parameters are listed in Table 4.9.

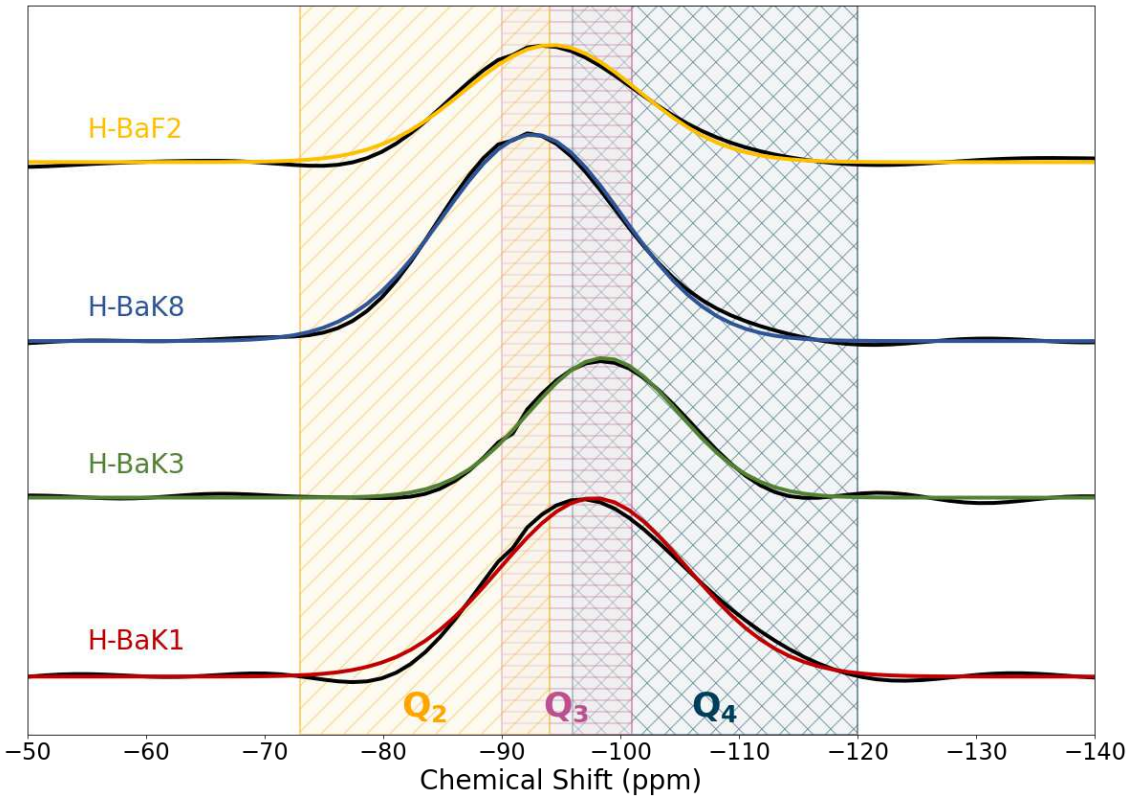

Figure 4.10: ^{29}Si MAS-NMR spectra of the H-BaK and H-BaF CDGM glasses. Shaded areas represent the chemical shift range of the Si Q-species

Table 4.9: ^{29}Si MAS-NMR Gaussian peak fitting parameters of the H-BaK and H-BaF CDGM glasses

Sample	FWHM (ppm)	δ (ppm)
H-BaK1	18.53	-97.72
H-BaK3	14.92	-98.55
H-BaK8	17.77	-92.59
H-BaF2	17.34	-94.17

Figure 4.11 confirms the above statement, as the apparent Gaussian center of gravity shifts more negative as samples become more shielded when the amount of network modifier decreases in the samples. This suggests higher network polymerization for the H-BaK1 and H-BaK3 samples (more Q^4 units) compared to the H-BaK8

and H-BaF2 samples (more Q^2 units).

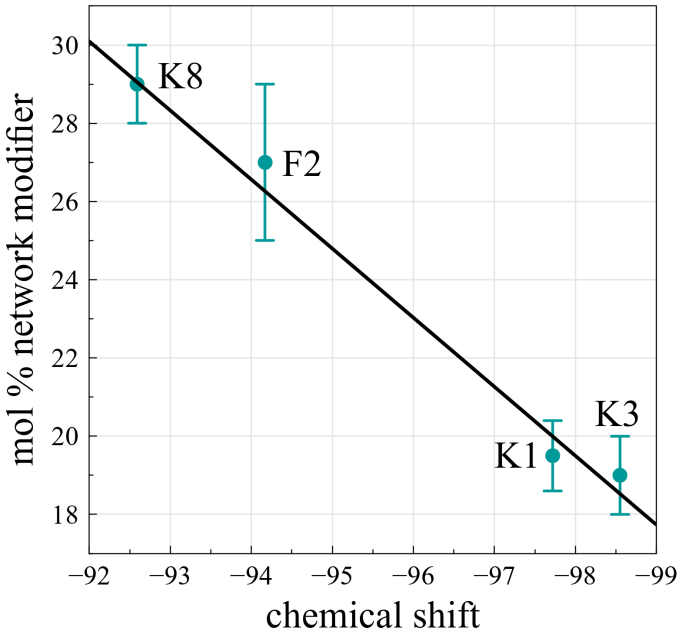

Figure 4.11: Relationship between mol % glass network modifiers (BaO, ZnO, Sb_2O_3, TiO_2, K_2O and Na_2O) to the average ^{29}Si NMR chemical shift. Higher network polymerization for more shielded chemical shifts

The Raman and NMR spectroscopy data confirm higher network polymerization for the H-BaK1 and H-BaK3 samples as these samples have a relatively higher concentration of SiO_2 Q^4 and Q^3 units compared to Q^2. They also confirm the H-BaK8 and H-BaF2 samples having more Q^2 relative to the other two samples, suggesting the glass network forms a higher degree of NBOs.

4.6.3 ^{31}P NMR on H-ZF Glasses

Figure 4.12 shows the ^{31}P single pulse MAS-NMR experiment results for the H-ZF samples spinning at 20 kHz in a 9.4 T magnet.

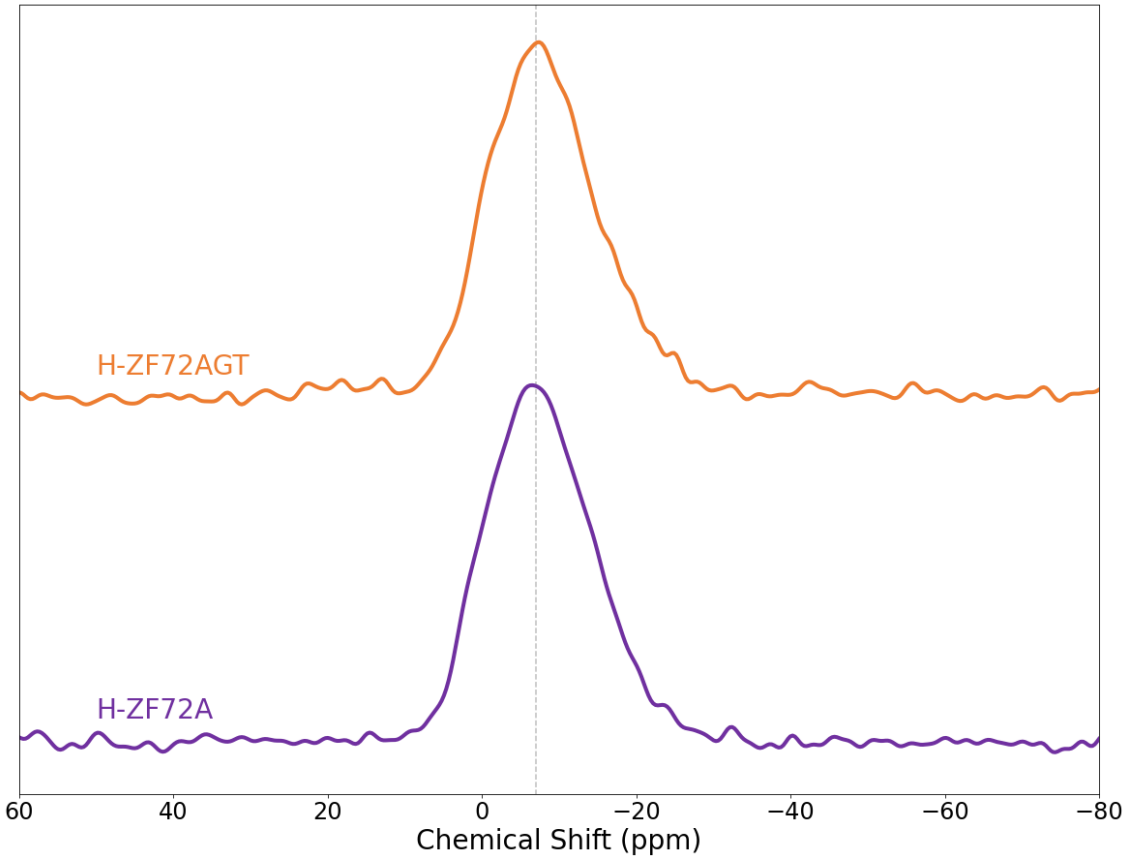

Figure 4.12: ^{31}P MAS-NMR spectra of the H-ZF CDGM glasses, normalized peak heights

The spectra show evidence of the existence of phosphorus linked to one (Q^1[Nb, Na], -9 ppm) and perhaps two (Q^2[Na], -20 ppm) additional phosphorus [63, 31, 57]. The shoulder on the left side (-3 ppm) of the main band could be attributed to Q^0[Nb, Na] [63]. Resolving the individual species are not feasible for this spectra due to strong overlap of the Q-species and their dependence on the mix of other cations present in the sample [57]. The chemical shift of the spectra suggest the inclusion of Nb in the samples affects the shielding. Samples of the composition $x$$Nb_2O_5$-(100-$x$)$NaPO_3$ with higher mol % concentration of Nb_2O_5 have been shown to be less shielded than samples with higher mol % concentration of $NaPO_3$ [63]. Niobium seems to decrease the network polymerization of the phosphorus units. Moreover,

there is no distinguishable difference between the shape of the ^{31}P NMR spectra of the H-ZF72A and H-ZF72AGT samples. The band intensity of the H-ZF72AGT was, however, about 40% less than that of the H-ZF72A sample (despite the rotors having similar weights) for reasons unknown (See Appendix A).

4.6.4 ^{93}Nb NMR on H-ZF Glasses

Lastly the ^{93}Nb NMR spectra of the H-ZF samples are given in Figure 4.13.

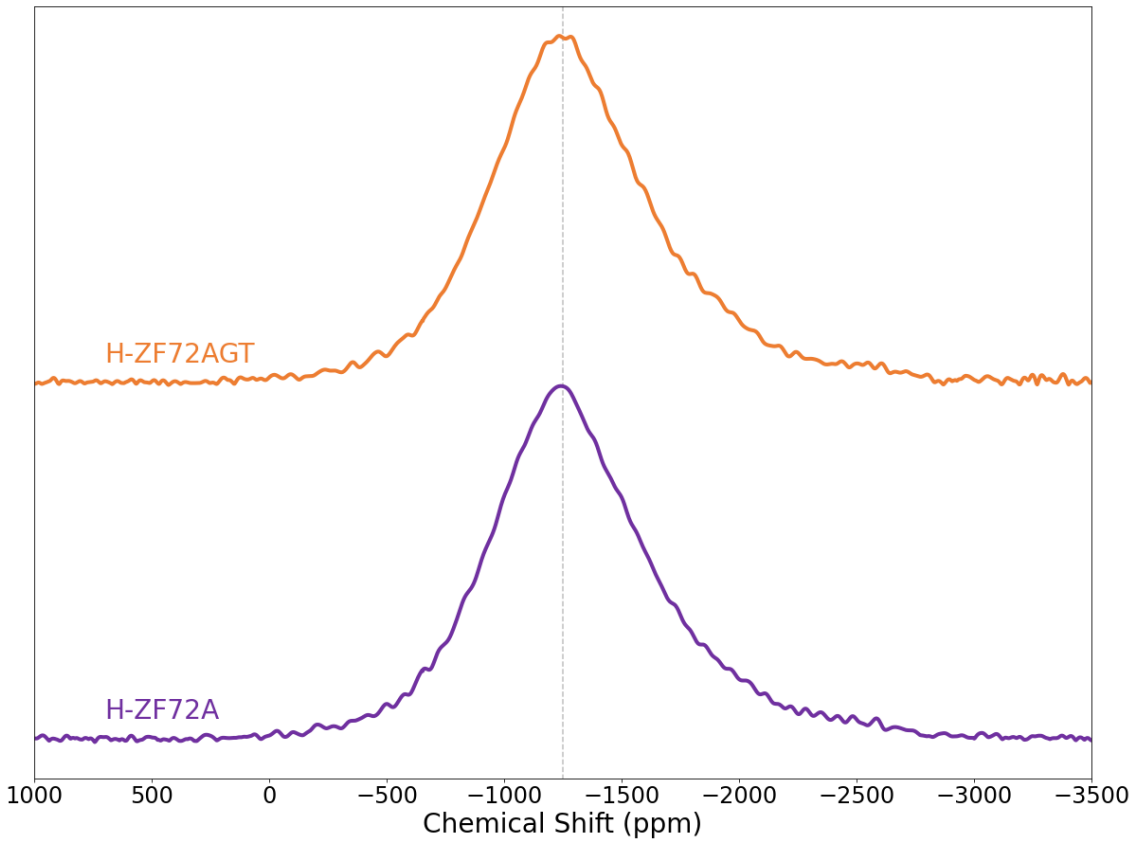

Figure 4.13: ^{93}Nb NMR spectra of the H-ZF CDGM glasses

The spectra were obtained from static WCPMG experiments in a 16.4 T magnet as MAS did not improve spectral resolution. ^{93}Nb is a I = 9/2 nucleus and is subject to second-order quadrupolar broadening. The chemical shift of crystalline references is found to be between -1000 to -1250 ppm for $Nb(ONb)_6$ and -1300 to -1650 ppm

for $Nb(OP)_{6-y}(ONb)_y$ with $1 \leqslant y \leqslant 5$ [64]. The peak maxima of the CDGM samples are located at -1250 ppm is consistent in location and shape with (30/40)Nb_2O_5-(70/60)$NaPO_3$ and 55$NaPO_3$-20ZnO-20Nb_2O_5-5Al_2O_3 glass samples [63, 57]. The Raman spectra and the ^{31}P and the ^{93}Nb NMR spectra show evidence of the glass network containing a mixture of Nb–O–Nb, P–O–P and Nb–O–P bonds.

4.7 Acousto-Optic Results

Previous work in this group utilized the Dixon-Cohen (DC) technique to measure the individual photoelastic tensor elements of a set of optical glasses [65]. The reliability of the setup was tested using an anti-reflective coated fused quartz sample bonded to the fused quartz (FQ) reference cell at an optical wavelength of 670 nm. The reported magnitude of p_{11} and p_{12} were within 1-2% of the accepted value [65].

4.7.1 Extending Measurements to Different Wavelengths

Two methods to measure the dispersion of the photoelastic tensor elements were tested with a FQ sample to find one that had the most suitable results. The first was to use a fixed optical wavelength of 670 nm through the reference and only change the optical wavelength through the sample. This way only the p_{ij} of the reference at 670 nm was needed to measure the p_{ij} of the sample at other wavelengths as they are predonimantly reported at an optical wavelength of 632.8 nm in literature [66, 67, 68]. This method has already been used in literature to measure the dispersion of the photoelastic coefficients in ZnSe [69].

The second method could only be accomplished if the dispersion of p_{11} and p_{12} of FQ was known. Thankfully, a report published by D. K. Biegelsen and J. C. Zesch (B-Z) in 1976 had performed these measurements of FQ using a similar technique to the DC method [4]. Their data (measured from 457.9 - 676.4 nm) was an integral part in measuring the dispersion of the photoelastic tensor elements using this method

as the DC technique can only measure them relative to a reference with a known response. Linear fits were applied to the B-Z data to approximate the p_{ij} for our laser wavelengths (405, 440, 543, 594, 670, 785, 850 nm). Incorporating these corrections into Equation 3.9 to account for the difference in wavelength between the sample λ_S and the reference λ_R as well as the difference in the unperturbed optical intensities which may occur in changing the lasers through the sample $\Im_{\text{samp}}$ and through the reference $\Im_{\text{ref}}$ yields Equation 4.5. In theory, this would eliminate the need for anti-reflective coatings on the samples to obtain better results, making this technique more convenient and affordable.

$$p_{ij(\text{samp})} = \sqrt{\left(\frac{\lambda_S}{\lambda_R}\right)\left(\frac{\Im_{\text{FQ}}}{\Im_{\text{samp}}}\right)\sqrt{\frac{I_4 I_5}{I_1 I_R}}\left(\frac{p_{ij}^2 n^6}{\rho v_a^3}\right)_{\text{FQ}}\left(\frac{\rho v_a^3}{n^6}\right)_{\text{samp}}} \tag{4.5}$$

The dispersion results of both methods are directly compared to those obtained by Biegelsen and Zesch in Figure 4.14. The dispersion of the stress optic coefficient C of FQ has been largely studied in literature compared to that of the individual stress optic elements as mentioned previously. As a result, the two DC methods were used to calculate C of FQ and compared to literature values in Figure 4.15. Comparing the dispersion of C to other sources of literature affirms the legitimacy of the second method since there is the concern that calculating the dispersion p_{ij} using the B-Z results and then directly comparing to the B-Z data is circular.

Using the same wavelength through the reference and the sample is the clear winner for which method agrees more to literature values for both the p_{ij} and C of FQ. While the fixed reference wavelength has tolerable agreement for p_{11} from 543 nm onward, it does a poor job at predicting p_{12} and p_{44} in the high and low wavelength domains. This disagreement is further amplified in the plot of C, as there is a large discrepancy between the measured and expected C. As a consequence, the dispersion of the photoelastic tensor elements of the CDGM samples were measured using the

second method of having the same optical wavelength pass through the sample and the reference.

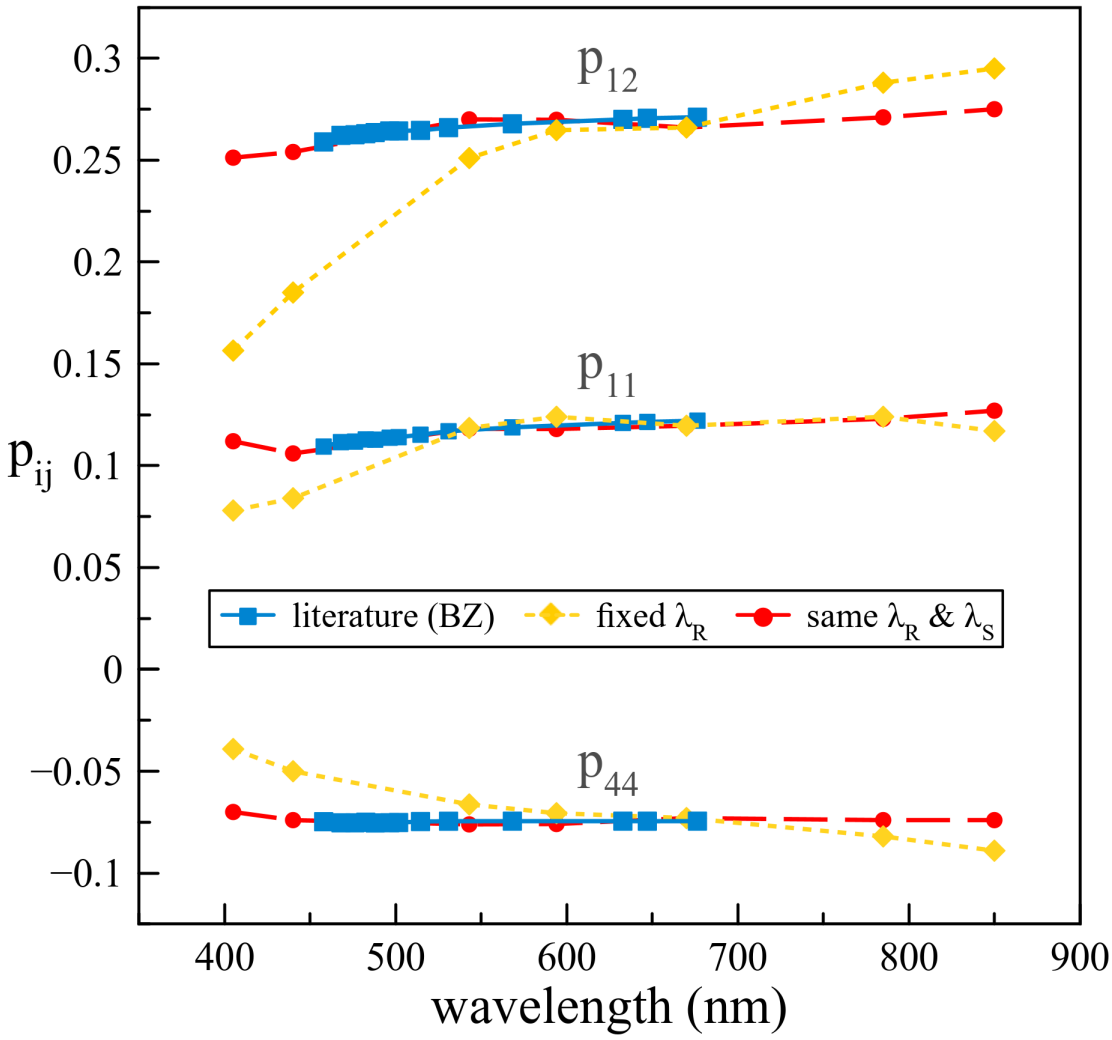

Figure 4.14: Comparing methods for measuring the dispersion of p_{ij} of a FQ sample to those measured by Biegelsen and Zesch (B-Z) represented by the blue squares [4]. The yellow diamonds represent the results obtained using a fixed wavelength of 670 nm through the reference, changing only the wavelength through the sample. The red circles represent the results obtained setting the same wavelength through as the reference and sample.

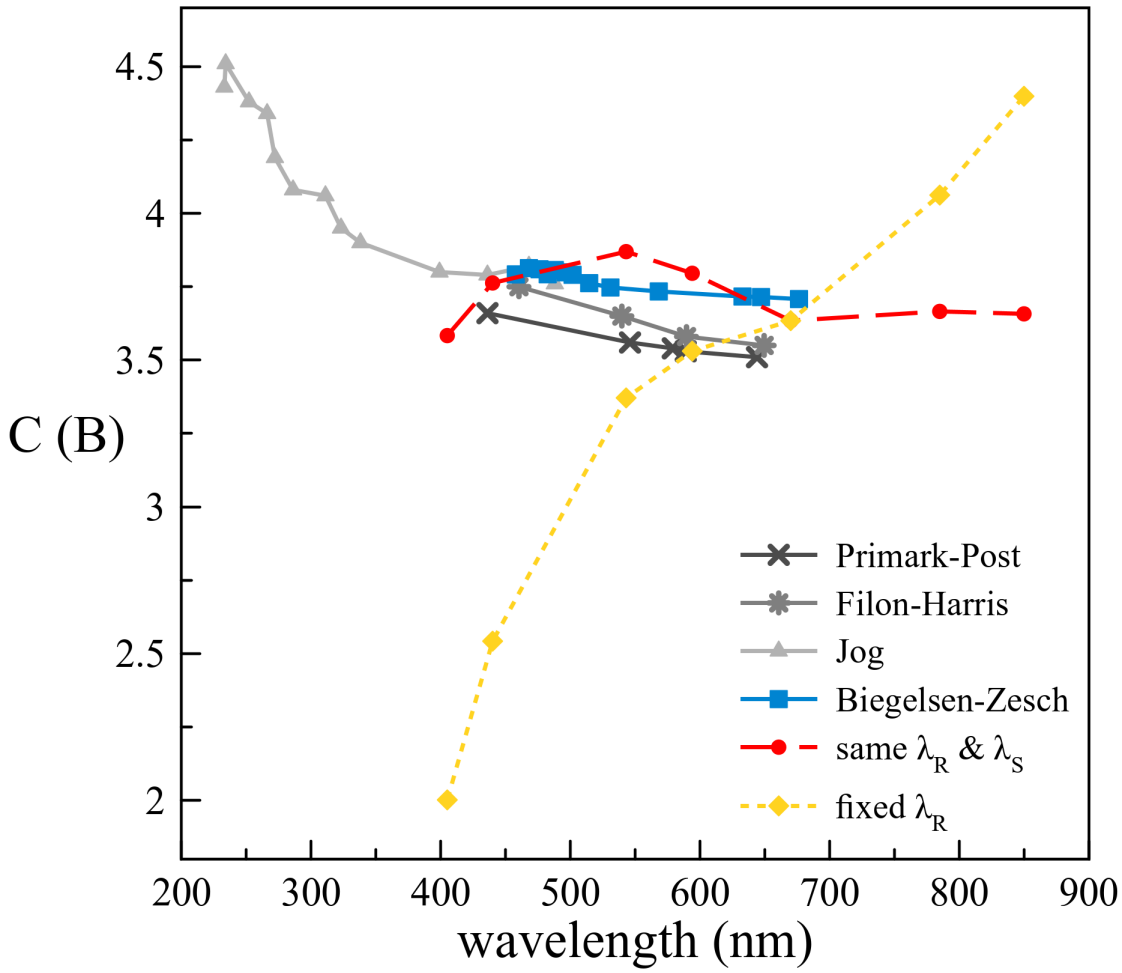

Figure 4.15: Comparing the measured dispersion of C of FQ to those measured in literature (grey and blue) [1, 2, 3, 4]. The yellow diamonds represent the results obtained using a fixed wavelength of 670 nm through the reference, changing only the wavelength through the sample. The red circles represent the results obtained setting the same wavelength through as the reference and sample.

4.7.2 CDGM Glasses

The measured dispersion of p_{11}, p_{12} and p_{44} of the CDGM samples are plotted in Figures 4.16, 4.17 and 4.18, respectively, and summarized in Table 4.10. All samples do not show a significant difference in p_{11}. The H-ZF samples do, however, show quite a difference in p_{12} compared to the silicate samples. As a result of p_{12} being larger, p_{44} is thusly more negative for the H-ZF samples. Additionally, the photoelastic dispersion of the H-ZF samples starts to diverge at the lower wavelengths as the absorption edge is in close proximity. The uncertainty of the p_{ij} are determined from the method described in Appendix C.

Figure 4.19 plots the relationship between the p_{ij} and the measure mol % SiO_2 in the samples including that of pure fused silica. As the modifier content in the glass increases, p_{12} and decreases, p_{44} increases and p_{11} does not seem to have a clear trend. These findings are consistent with previous composition analysis performed in the Zwanziger group [70].

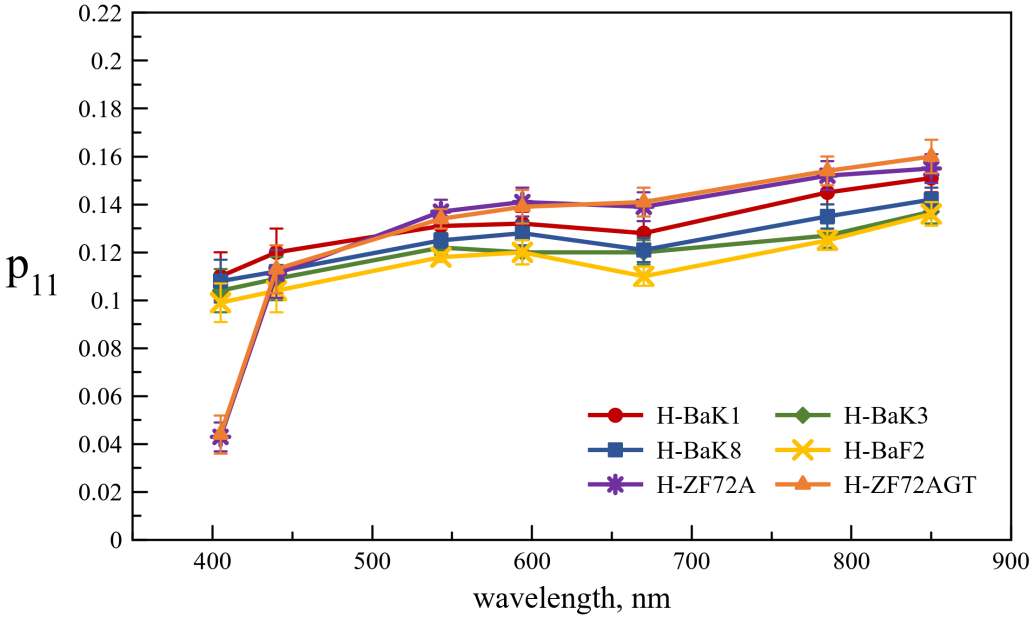

Figure 4.16: Wavelength dispersion of p_{11} of the CDGM glasses

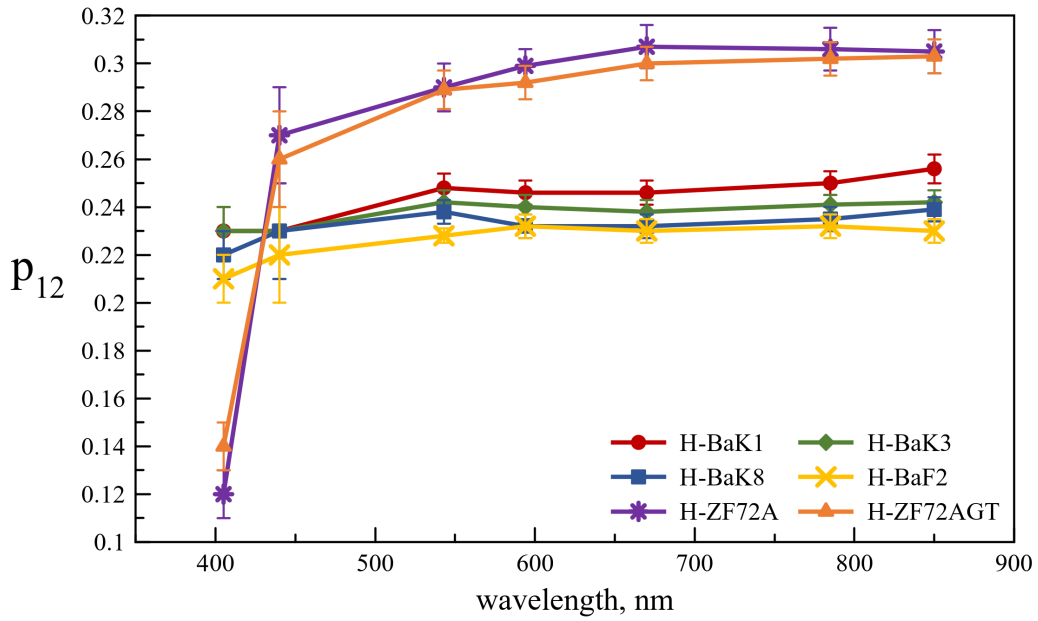

Figure 4.17: Wavelength dispersion of p_{12} of the the CDGM glasses

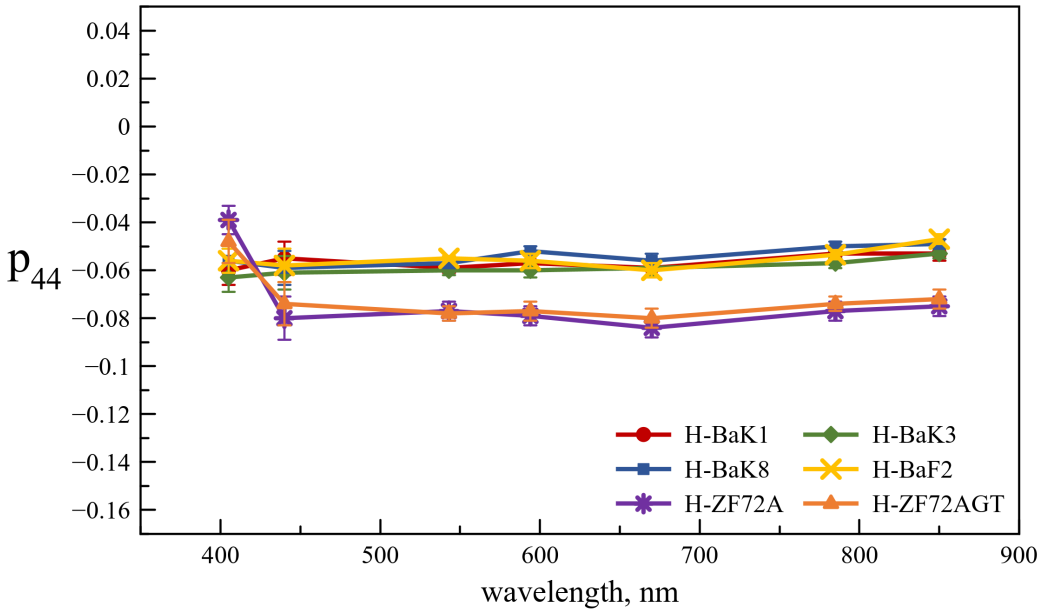

Figure 4.18: Wavelength dispersion of p_{44} of the the CDGM glasses

Table 4.10: Photoelastic data of the CDGM glasses at various wavelength measured using the Dixon-Cohen method

Sample	λ (nm)	p_{11}	p_{12}	p_{44}
H-BaK1	405	0.11(1)	0.23(1)	-0.060(6)
	440	0.12(1)	0.23(2)	-0.055(7)
	543	0.131(3)	0.248(5)	-0.059(2)
	594	0.132(5)	0.246(5)	-0.057(3)
	670	0.128(5)	0.246(5)	-0.059(3)
	785	0.145(5)	0.250(5)	-0.053(2)
	850	0.150(6)	0.256(6)	-0.053(3)
H-BaK3	405	0.104(9)	0.23(1)	-0.063(6)
	440	0.109(9)	0.23(1)	-0.061(7)
	543	0.122(3)	0.242(5)	-0.060(2)
	594	0.120(5)	0.240(5)	-0.060(3)
	670	0.120(5)	0.238(5)	-0.059(3)
	785	0.127(5)	0.241(4)	-0.057(2)
	850	0.137(5)	0.242(5)	-0.053(2)
H-BaK8	405	0.108(9)	0.22(1)	-0.056(5)
	440	0.112(9)	0.23(2)	-0.059(7)
	543	0.125(3)	0.238(4)	-0.057(2)
	594	0.128(5)	0.232(4)	-0.052(2)
	670	0.121(5)	0.232(5)	-0.056(3)
	785	0.135(5)	0.235(4)	-0.050(2)
	850	0.142(5)	0.239(4)	-0.049(2)
H-BaF2	405	0.099(8)	0.21(1)	-0.056(5)
	440	0.104(9)	0.22(2)	-0.058(7)
	543	0.118(2)	0.228(2)	-0.055(1)
	594	0.120(5)	0.232(5)	-0.056(3)
	670	0.110(4)	0.230(4)	-0.060(3)
	785	0.125(4)	0.232(4)	-0.054(2)
	850	0.136(5)	0.230(4)	-0.047(2)
H-ZF72A	405	0.043(6)	0.12(1)	-0.039(6)
	440	0.11(1)	0.27(2)	-0.080(9)
	543	0.137(5)	0.29(1)	-0.077(4)
	594	0.141(6)	0.299(7)	-0.079(4)
	670	0.139(6)	0.307(9)	-0.084(4)
	785	0.152(6)	0.306(9)	-0.077(4)
	850	0.155(6)	0.305(9)	-0.075(4)
H-ZF72AGT	405	0.044(8)	0.14(1)	-0.048(9)
	440	0.11(1)	0.26(1)	-0.074(9)
	543	0.134(4)	0.289(8)	-0.078(3)
	594	0.139(7)	0.291(7)	-0.077(4)
	670	0.141(6)	0.300(7)	-0.080(4)
	785	0.154(6)	0.302(7)	-0.074(3)
	850	0.160(7)	0.303(7)	-0.072(4)

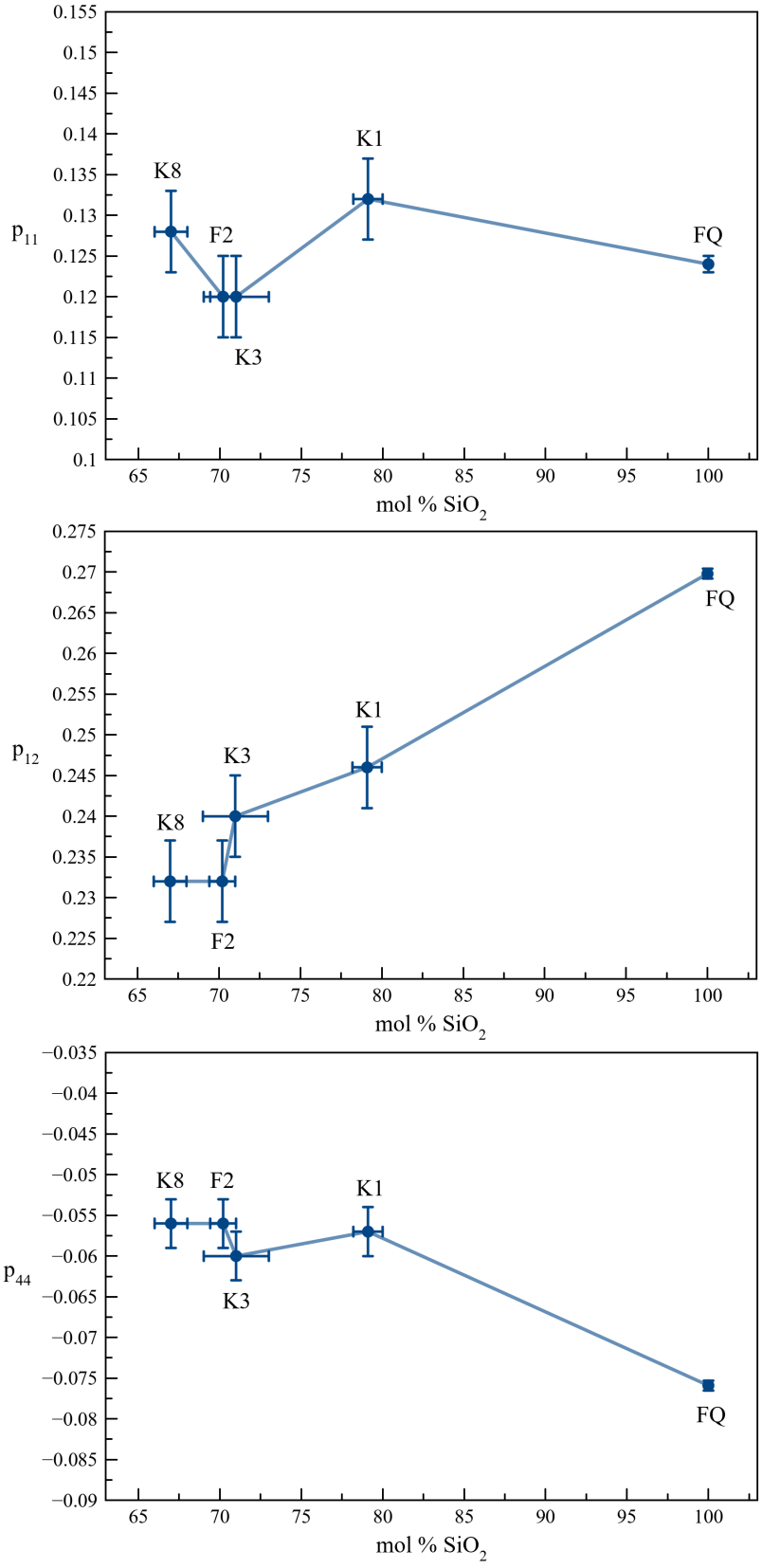

Figure 4.19: p_{ij} of H-BaK and H-BaF CDGM glasses and pure FQ with respect to mol % SiO_2 at an optical wavelength of 594 nm

4.8 Bond Polarizabilities

The average bond polarizability parameters were calculated for the CDGM glasses using the equations expressed in Section 2.2.4 from the measured p_{11}, p_{12} and n. Figure 4.20 shows the pure dilation and anisotropy terms $\langle\alpha_V\rangle$, $\langle\alpha_1\rangle$ and $\langle\alpha_Q\rangle$. The longitudinal and transverse bond polarizabilities $\langle\alpha_{||}\rangle$ and $\langle\alpha_{\perp}\rangle$ are given in Figure 4.21. H-ZF72A displays such a large $\langle\alpha_Q\rangle$ compared to the other samples due to the large difference between $\langle\alpha_{||}\rangle$ and $\langle\alpha_{\perp}\rangle$. Note that only the H-ZF72A sample is present in the figures, as the H-ZF72A and H-ZF72AGT samples had practically identical polarizability parameters.

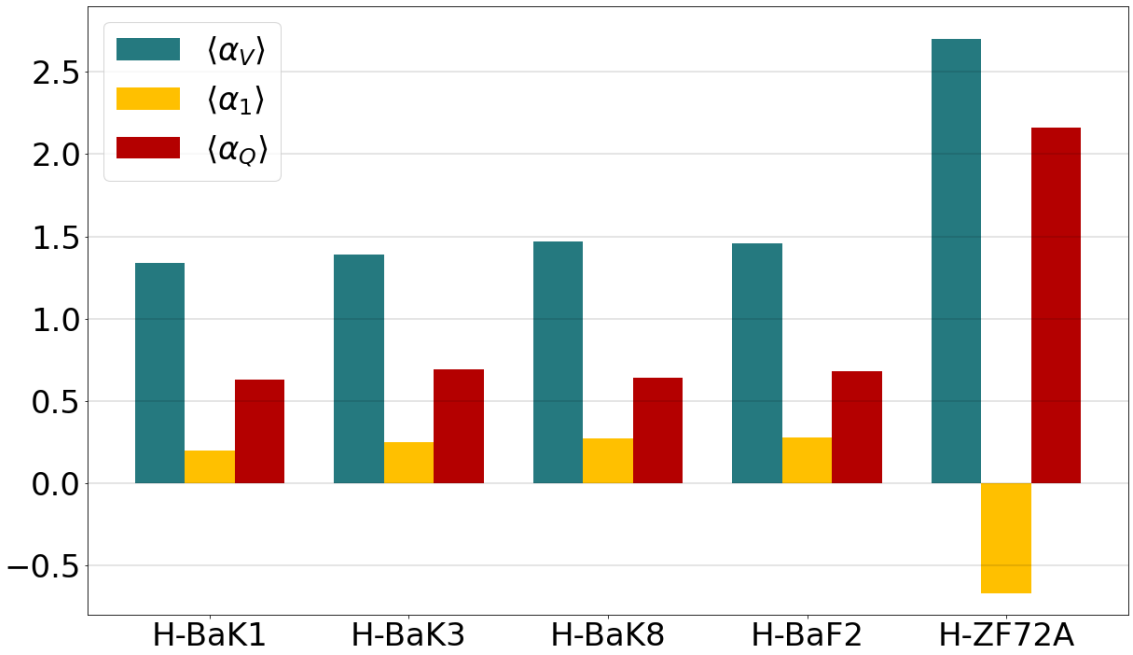

Figure 4.20: Pure dilation ($\langle\alpha_V\rangle$ & $\langle\alpha_1\rangle$) and anisotropic stress ($\langle\alpha_Q\rangle$) average bond polarizability parameters at an optical wavelength of 594 nm

The H-BaK and H-BaF have comparable bond polarizabilities since they have very similar photoelastic response and refractive indices. The anisotropy term is approximately half of that of the volume term for those samples. The H-ZF samples are the clear outlier. While both $\langle\alpha_V\rangle$ and $\langle\alpha_Q\rangle$ are scaled by the magnitude of the

index of refraction, the larger p_{44} of the H-ZF samples causes $\langle \alpha_Q \rangle$ to be even larger, making the relative difference between the volume and anisotropy terms smaller. No known trend between the photoelastic and structural data was established for $\langle \alpha_1 \rangle$.

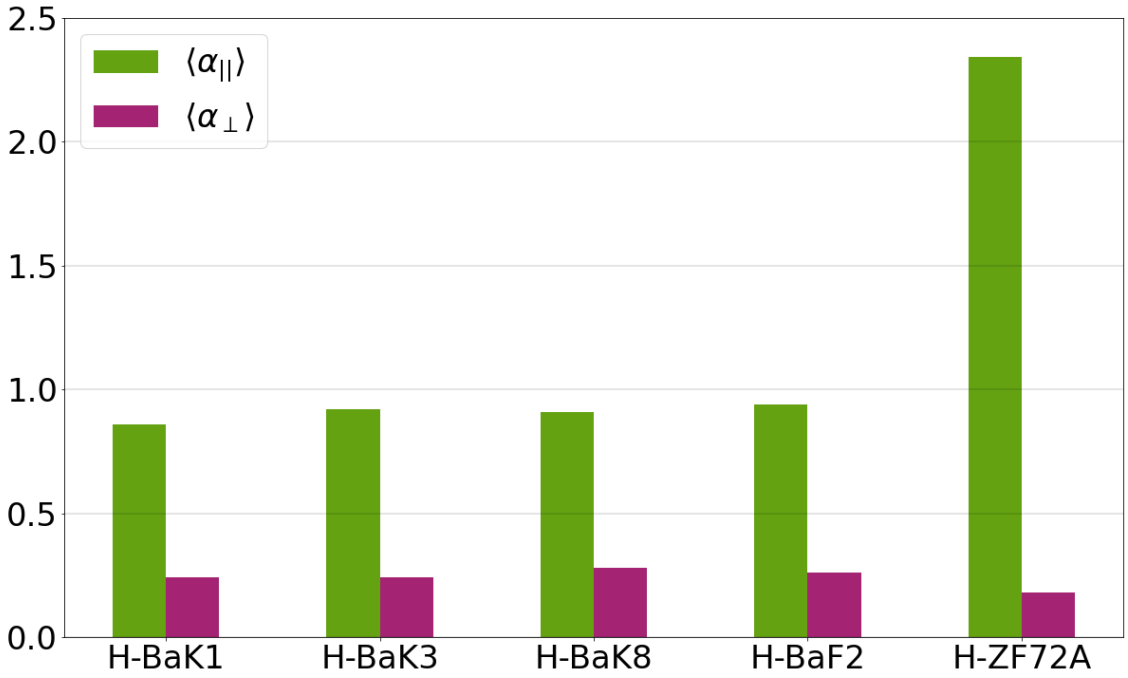

Figure 4.21: Longitudinal ($\langle \alpha_{||} \rangle$) and transverse ($\langle \alpha_{\perp} \rangle$) average bond polarizability parameters at an optical wavelength of 594 nm

As established in Figure 4.4, the H-BaK and H-BaF samples are silicates, while the H-ZF samples are niobiophosphates. One would expect the bonding of these network formers to behave quite differently. As a general rule of thumb, the band gap energy decreases with increasing bond length. Shorter bonds with large band gaps such as Si–O in pure SiO_2 have strong directive bonds (covalent), meaning the total polarizablity is relatively small, but highly directional as the metallicity is low. With the addition of network modifiers, the bonding type becomes increasingly ionic as more NBOs form, causing the total polarizability to increase. The polarizability would now be expected to become less directional than that of pure SiO_2 and more isotropic. This would explain why $\langle \alpha_{\perp} \rangle$ is non-zero. The P–O bond is assumed to

behave quite similarly to Si–O, as they have similar bond lengths and similar the band gaps between SiO_2 and P_2O_5. The bond length of Nb–O is larger than those of P–O and Si–O and the band gap is roughly a third smaller. One would anticipate the addition of Nb_2O_5 to P_2O_5 will increase the metallicity of the system, causing the total polarizability to increase, while also increasing the isotropic polarizability. Section 4.2 confirms these approximations as the apparent average band gap E_0, obtained from the dispersion of the index of refraction, of the H-ZF samples were roughly half of that of the silicate CDGM samples.

Chapter 5

Conclusions

The results of this thesis present the dispersion of the photoelastic elements of a set of commercial CDGM optical glasses using the Dixon-Cohen acousto-optic technique [66]. The success of this method would not be attainable if it were not for the dispersion p_{11} and p_{12} data reported by Bielgelsen and Zesch for fused quartz [4]. A FQ sample was used to test the validity of this method by first measuring p_{11} and p_{12} to calculate C and compare the results to various literature sources.

Four alkali silicate samples (H-BaK1, H-BaK3, H-BaK8 and H-BaF2) were chosen for their compositional similarity reported in the sample MSDS, with slight changes in SiO_2 and modifier content. An additional two samples (H-ZF72A and H-ZF72AGT) were acquired from Illumina, Inc. The weight % compositions of all six samples were measured with WDS. While the silicate samples had reasonable elemental analysis results compared to those expected from the MSDS, the H-ZF samples had a staggering amount of Nb_2O_5 present despite it not being reported. This was later confirmed with Raman and NMR spectroscopy. Furthermore, the total average weight percent oxide of the H-BaK and H-BaF samples were missing 4-9% (from 100%) of the total average weight%. They therefore do not satisfy the condition for typical "good" agreement in the range of 98.5-100.5%.

The distribution of silicate Q-species in the H-BaK and H-BaF samples were determined from Raman and ^{29}Si ss-NMR spectroscopy. The data suggests a higher degree of network polymerization from the larger distribution of Q^4 units in the

H-BaK1 and H-BaK3 samples relative to the higher distribution of Q^2 units in the H-BaK8 and H-BaF2 samples, implying a larger degree of NBOs in the silicate network. This would also conclude that the degree of network polymerization weakens as more network modifiers are introduced into the samples, as expected. The photoelastic data suggests a positive/negative correlation between network polymerization and p_{12}/p_{44}, respectively.

The Raman, ^{31}P and ^{93}Nb ss-NMR spectroscopy of the H-ZF samples indicate a mixture of Nb–O–Nb, P–O–P and Nb–O–P bonds are present in the glass network. A prominent photoelastic feature of these samples is how the magnitude of p_{11} is quite comparable to those of the silicate samples, yet p_{12} is found to be 130% larger, making the anisoptic term p_{44} larger as a result.

The average bond polarizability parameters is a postulatory means of inspecting the bulk polarizability from a bonding perspective. The silicate samples had practically identical parameters across the board. This indicates the polarizability parameters are relatively insensitive to next nearest-neighbours for these samples. Fundamentally, the silicate network does not change with degree of network polymerization. It is worth noting that this study was not comprehensive enough to set this conclusion in stone for all glass systems. Additionally, the inclusion of alkali modifiers to a silicate network causes $\langle\alpha_\perp\rangle$ to be non-zero as the NBOs induces less directional polarizability compared to the average bonding in pure SiO_2.

The addition of Nb_2O_5 to P_2O_5 in the H-ZF samples increases the metallicity of the system, thus increasing the overall polarizability, as was clearly depicted in the results. This result is supported by the Wemple-DiDomenico model to estimate the bandgap from the dispersion of the index of refraction. The bandgap H-ZF sample was approximated to be roughly half of that of the silicate samples. Larger bandgaps suggests electrons are more tightly bound to the atom, requiring more energy to remove the electron, thus increasing the bandgap. This would also imply a material

with a smaller bandgap, such as the H-ZF samples are more polarizable than the silicate samples.

An in depth analysis of the $\langle\alpha_1\rangle$ parameter and its role merging the electronic and structural properties would be practical as it is currently non-trivial. Further investigation of the average bond polarizability parameters and how they behave as a function of network former and modifiers types may assist to advance our understanding of the tunablility of p_{11} and p_{12}. A systematic approach in changing the quantity of network modifiers within simpler glass systems would be best to analyze the effects.

Bibliography

[1] W. Primak and D. Post. Photoelastic constants of vitreous silica and its elastic coefficient of refractive index. *Journal of Applied Physics*, 30(5):779–788, 1959.

[2] L. N. G. Filon and F. C. Harris. The photo-elastic dispersion of vitreous silica. *Proceedings of the Royal Society of London. Series A, Containing Papers of a Mathematical and Physical Character*, 130(813):410–431, 1931.

[3] E. S. Jog. The dispersion of the stress optical coefficient of vitreous silica. *Journal of the Indian Institute of Science*, 39(2):93–100, 1957.

[4] D. K. Biegelsen and J. C. Zesch. Optical frequency dependence of the photoelastic coefficients of fused silica. *Journal of Applied Physics*, 47:4024–4025, 1976.

[5] A. K. Varshneya. *Fundamentals of Inorganic Glasses*. Academic Press, Inc., 1994.

[6] G. W. Morey. *The Properties of Glass*. Reinhold Publishing Corporation, 1938.

[7] J. E. Shelby. *Introduction to Glass Science and Technology*. The Royal Society of Chemistry, 2nd edition, 2005.

[8] S. M. Allen and E. L. Thomas. *The Structure of Materials*. Wiley, 1999.

[9] W. H. Zachariasen. The atomic arrangement in glass. *Journal of the American Chemical Society*, 54(10):3841–3851, 1932.

[10] Technical information advanced optics: Refractive index and dispersion. Technical Report TIE-29, Schott, Germany, February 2016. [Online; accessed February 2023].

[11] C. L. Chen. *Foundations for Guided-Wave Optics*. John Wiley & Sons, Inc., 2007.

[12] J. F. Nye. *Physical Properties of Crystals; Their Representation by Tensor and Matrices*. Oxford University Press Inc., 1985.

[13] T. S. Narasimhamurty. *Photoelastic and Electro-Optic Properties of Crystals*. Plenum Press, first edition, 1981.

[14] H. Mueller. Theory of photoelasticity in amorphous solids. *Journal of Applied Physics*, 6:179–184, 1935.

[15] A. A. Maradudin and E. Burnstein. Relation between photoelasticity, electrostriction, and first-order raman effect in crystals of the diamond structure. *Physical Review*, 164(3):1081–1099, 1967.

[16] S. Go, H. Bilz, and M. Cardona. Bond charge, bond polarizability, and phonon spectra in semiconductors. *Physical Review Letters*, 34(10):580–583, 1975.

[17] N. W. Ashcroft and N. D. Mermin. *Solid State Physics*. Harcourt College Publishers, Inc., college edition, 1976.

[18] J. Galbraith, L. Chapman, J. W. Zwanziger, M. Aldridge, and J. Kieffer. Elasto-optic coefficients of borate, phosphate, and silicate glasses: Determination by brillouin spectroscopy. *The Journal of Physical Chemistry C*, pages 21802–21810, 2016.

[19] M. Guignard, L. Albrecht, and J. W. Zwanziger. Zero-stress optic glass without lead. *Chemistry of Materials*, 19(2):286–290, 2007.

[20] B. E. A. Saleh and M. C. Teich. *Fundamentals of Photonics*. John Wiley & Sons, Inc., 1991.

[21] J. Ballato and P. Dragic. Tailoring the response of stimulated brillouin scattering in fibers. *Optical Society of America*, 2017.

[22] A. Kobyakov, M. Sauer, and D. Chowdhury. Stimulated brillouin scattering in optical fibers. *Advances in Optics and Photonics*, 2:1–59, 2010.

[23] T. Schneider. *Nonlinear Optics in Telecommunications*. Springer-Verlag Berlin Heidelberg, first edition, 2004.

[24] M. J. A. Smith, B. T. Kuhlmey, C. Martijn de Sterke, C. Wolff, M. Lapine, and C. G. Poulton. Metamaterial control of stimulated brillouin scattering. *Optics Letters*, 41(10):2338–2341, 2016.

[25] T. Nelligan. Olympus industrial resources: An introduction to ultrasonic thickness gaging. https://www.olympus-ims.com/en/applications-and-solutions/introductory-ultrasonics/introduction-thickness-gaging/. Accessed: 2022-11-05.

[26] Atago, Japan. *Multi-wavelength Abbe Refractometer DR-M2/1550 DR-M4/1550 Instruction Manual*.

[27] S. J. B. Reed. *Electron Microprobe Analysis and Scanning Electron Microscopy in Geology*. Cambridge University Press, 2nd edition, 2005.

[28] J. R. Ferraro, K. Makamoto, and C. W. Brown. *Introductory Raman Spectroscopy*. Elsevier, 2nd edition, 2003.

[29] D. Tuschel. Why are the raman spectra of crystalline and amorphous solids different? *Spectroscopy*, 32:26–33, 2017.

[30] R. M. Almeida and L. F. Santos. Raman spectroscopy of glasses. In M. Affatigato, editor, *Modern Glass Characterization*, chapter 3, pages 74–103. The American Ceramic Society and John Wiley & Sons, Inc., 2015.

[31] K. J. D. Mackenzie and M. E. Smith. *Multinuclear Solid-State NMR of Inorganic Materials*, volume 6. Elsevier Science Ltd., 2002.

[32] F. A. Bovey. *Nuclear Magnetic Resonance Spectroscopy*. Academic Press, Inc., second edition, 1988.

[33] P. J. Hore. *Nuclear Magnetic Resonance*. Oxford University Press, second edition, 2015.

[34] M. H. Levitt. *Spin Dynamics Basics of Nuclear Magnetic Resonance*. John Wiley & Sons, Ltd, 2nd edition, 2008.

[35] R. Siegel, T. T. Nakashima, and R. E. Wasylishen. Signal-to-noise enhancement of nmr spectra of solids using multiple-pulse spin-echo experiments. *Concepts in Magnetic Resonance Part A*, 26A(2):62–77, 2005.

[36] K. K. Dey, J. T. Ash, N. M. Trease, and P. J. Grandinetti. Trading sensitivity for information: Carr-purcell-meiboom-gill acquisition in solid-state nmr. *The Journal of Chemical Physics*, 133(5):054501, 2010.

[37] L. A. O'Dell. The wurst kind of pulses in solid-state nmr. *Solid State Nuclear Magnetic Resonance*, 55-56(2):28–41, 2013.

[38] J. R. Taylor. *An Introduction to Error Analysis*. University Science Books, second edition, 1997.

[39] Optical glass database. http://www.cdgmgd.com/database/toWebDatabase.htm?k=Products_Data&url=database. Accessed: 2022-03-30.

[40] K. I. Hussein *et al.* The investigation of new phosphate-titanite glasses according to optical, physical, and shielding properties. *Crystals*, 12(7), 2022.

[41] H.Bach and N. Neuroth. *The Properties of Optical Glass*. Springer-Verlag Berlin Heidelberg, Germany, first, second corrected edition, 1998. Scott Glas.

[42] D. J. Griffiths. *Introduction to Electrodynamics*. Pearson Education, Inc., fourth edition, 2013.

[43] S. H. Wemple and M. DiDomenico Jr. Behavior of the electronic dielectric constant in covalent and ionic materials. *Physical Review B*, 3(4), 1971.

[44] P. Schweizer, Brackx E., and P. Jonnard. Electron probe microanalysis of light elements: Improvements in the measurement and signal extraction methods. *X-Ray Spectrometry*, 51:403–412, 2022.

[45] D. MacDonald. Data reduction guide - understanding epma analytical results. https://www.dal.ca/sites/electron-microprobe-lab/analysis.html. Accessed: 2023-02-17.

[46] C. H. Nielsen and H. Sigurdsson. Quantitative methods for electron microprobe analysis of sodium in natural and synthetic glasses. *American Mineralogist*, 66(5-6):547–552, 1981.

[47] D. W. Matson, S. K. Sharma, and J. A. Philpotts. The structure of high-silica alkali-silicate glasses. a raman spectroscopic investigation. *Journal of Non-Crystalline Solids*, 58:323–352, 1983.

[48] B. O. Mysen, D. Virgo, and F. A. Seifert. The structure of silicate melts: Implications for chemical and physical properties of natural magma. *Reviews of Geophysics and Space Physics*, 20(3):353–383, 1982.

[49] C. O'Shaughnessy, G. S. Henderson, H. W. Nesbitt, G. M Bancroft, and D. R. Neuville. Structure-property relations of caesium silicate glasses from room temperature to 1400 k: Implications from density and raman spectroscopy. *Chemical Geology*, 461:82–95, 2017.

[50] D. R. Neuville. Structure and properties in (sr, na) silicate glasses and melts. *Physics and Chemistry of Glasses*, 46(2):112–118, 2005.

[51] S. K. Sharma, J. F. Mammone, and M. F. Nicol. Raman investigation of ring configurations in vitreous silica. *Nature*, 292:140–141, 1981.

[52] P. McMillan. Structural studies of silicate glasses and melts – applications and limitations of raman spectroscopy. *American Mineralogist*, 69:622–644, 1984.

[53] G. S. Henderson and M. E. Fleet. The structure of ti silicate glasses by micro-raman spectroscopy. *The Canadian Mineralogist*, 33:399–408, 1995.

[54] A. El Jazouli, C. Parent, J. M. Dance, G. Le Flem, and P. Hagenmuller. $Na_4nb(po_4)_3$, a material with a reversible crystal-glass transformation: Structural and optical comparison. *Journal of Solid State Chemistry*, 74:377–384, 1988.

[55] A. J. Barboda *et al.* Er^{3+} doped phosphoniobate glasses and planar waveguides: structural and optical properties. *Journal of Physics: Condensed Matter*, 20:1–8, 2008.

[56] F. F. Sene, J. R. Martinelli, and L. Gomes. Synthesis and characterization of niobium phosphate glasses containing barium and potassium. *Journal of Non-Crystalline Solids*, 348:30–37, 2004.

[57] S. Chenu, Werner-Zwanziger U., C. Calahoo, and J. W. Zwanziger. Structure and properties of $napo_3$–zno–nb_2o_5–al_2o_3 glasses. *Journal of Non-Crystalline Solids*, 358:1795–1805, 2012.

[58] Y. Yu, B. Stevensson, and M. Edén. Direct experimental evidence for abundant bo_4bo_4 motifs in borosilicate glasses from double-quantum ^{11}b nmr spectroscopy. *The Journal of Physical Chemistry Letters*, 9:6372–6376, 2018.

[59] G. L. Turner, K. A. Smith, R. J. Kirkpatrick, and E. Oldfield. Boron-11 nuclear magnetic resonance spectroscopic study of borate and borosilicate minerals and a borosilicate glass[1]. *Journal of Magnetic Resonance*, 67:544–550, 1986.

[60] D. Massiot *et al.* Modelling one and two-dimensional solid-state nmr spectra. *Magnetic Resonance in Chemistry*, 40:70–76, 2002.

[61] L. Du and J. F. Stebbins. Solid-state nmr study of metastable immiscibility in alkali borosilicate glasses. *Journal of Non-Crystalline Solids*, 315:239–255, 2003.

[62] J. Machacek and O. Gedeon. Q-species in alkali-disilicate glasses. *Ceramics - Silikaty*, 47(2):45–49, 2003.

[63] A. Flambard *et al.* Solid-state nmr study of mixed network sodium-niobium phosphate glasses. *Journal of Non-Crystalline Solids*, 345&346:75–79, 2004.

[64] A. Flambard *et al.* Structure and nonlinear optical properties of sodium-niobium phosphate glasses. *Journal of Non-Crystalline Solids*, 354:3540–3547, 2008.

[65] Sutherland C. Implementation of an acousto-optic method for determining photoelastic tensor elements in glass. Master's thesis, Dalhousie University, 2021.

[66] R. W. Dixon and M. G. Cohen. A new technique for measuring magnitudes of photoelastic tensors and its application to lithium niobate. *Applied Physics Letters*, 8(8):205–207, 1966.

[67] K. Vedam. The elastic and photoelastic constants of fused quartz. *Physical Review*, 78:472–473, 1950.

[68] J. Schroeder. Brillouin scattering and pockels coefficients in silicate glasses. *Journal of Non-Crystalline Solids*, 40:549–566, 1980.

[69] K. Tada, K. Kikuchi, and Sato K. Dispersion of photoelastic coefficients in znse. *Japanese Journal of Applied Physics*, 16(5):757–760, 1977.

[70] Justine Galbraith. *Photoelastic Properties of Oxide and Non-Oxide Glasses*. PhD thesis, Dalhousie University, 2014.

Appendix A

Additional NMR Plots

The following plots were generated by Dr. Ulrike Werner-Zwanziger, solid-state NMR coordinator of the Dalhousie University NMR^3 Facility.

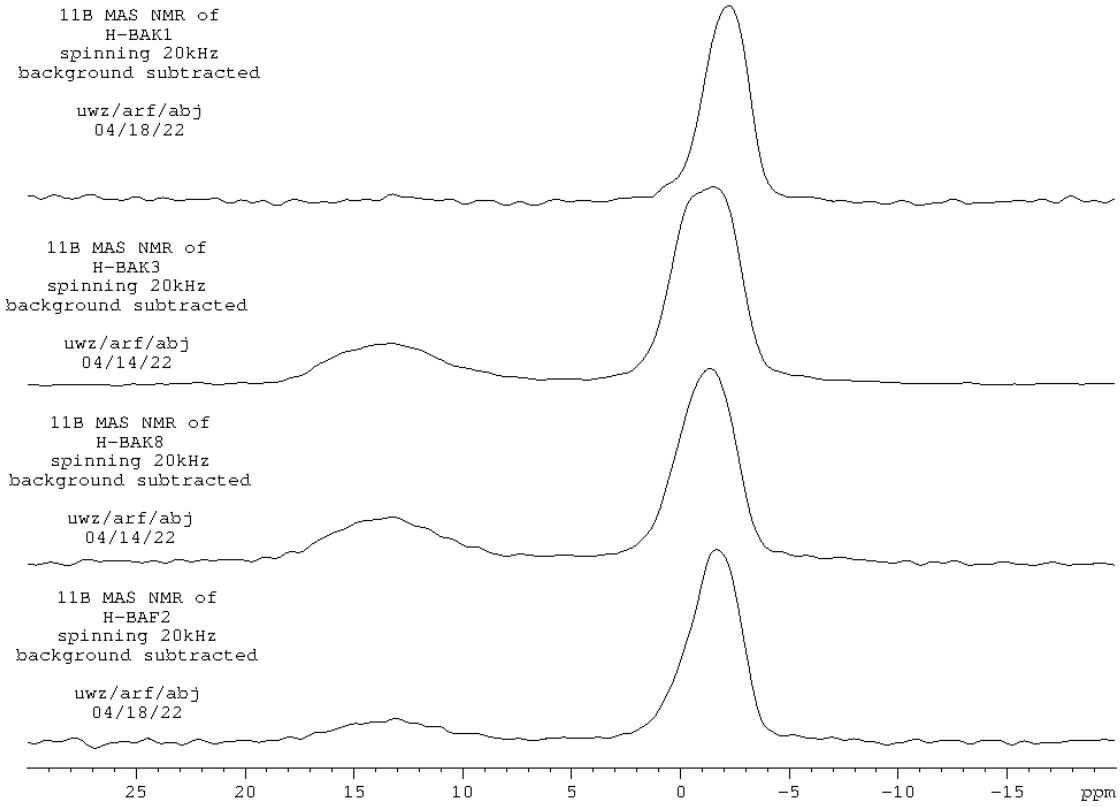

Figure A.1: Normalized ^{11}B MAS-NMR spectra of CDGM H-BaK and H-BaF samples

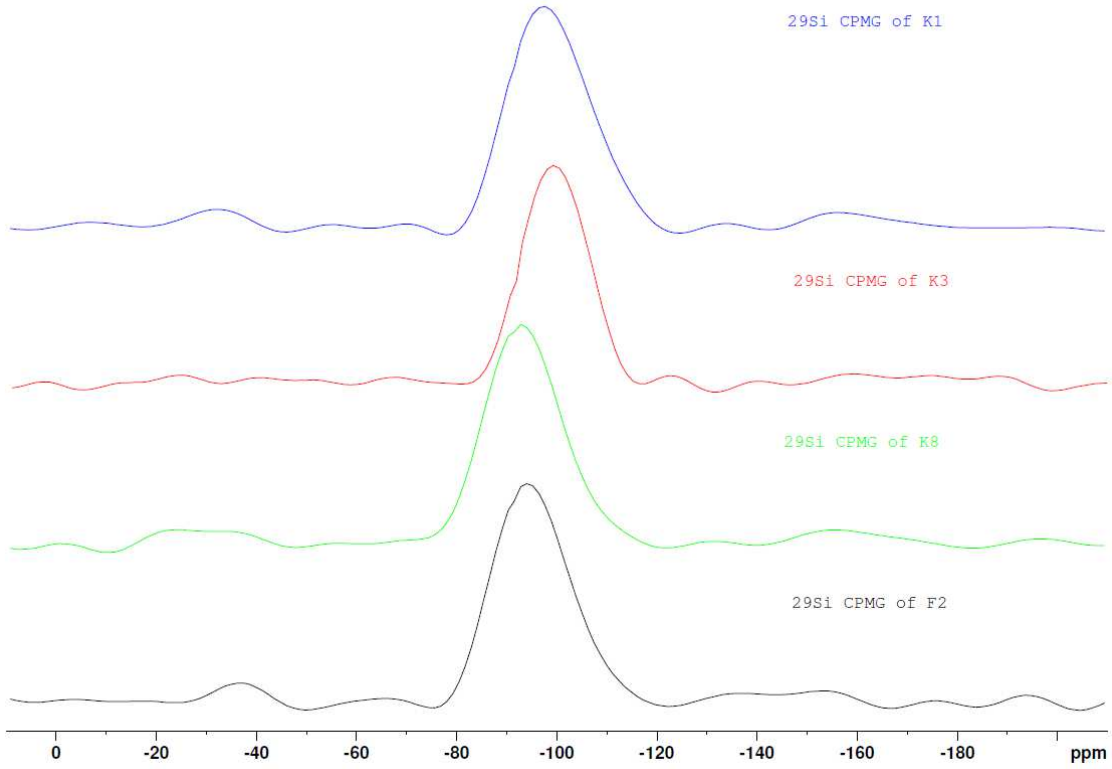

Figure A.2: ^{29}Si CPMG MAS-NMR spectra of CDGM H-BaK and H-BaF samples

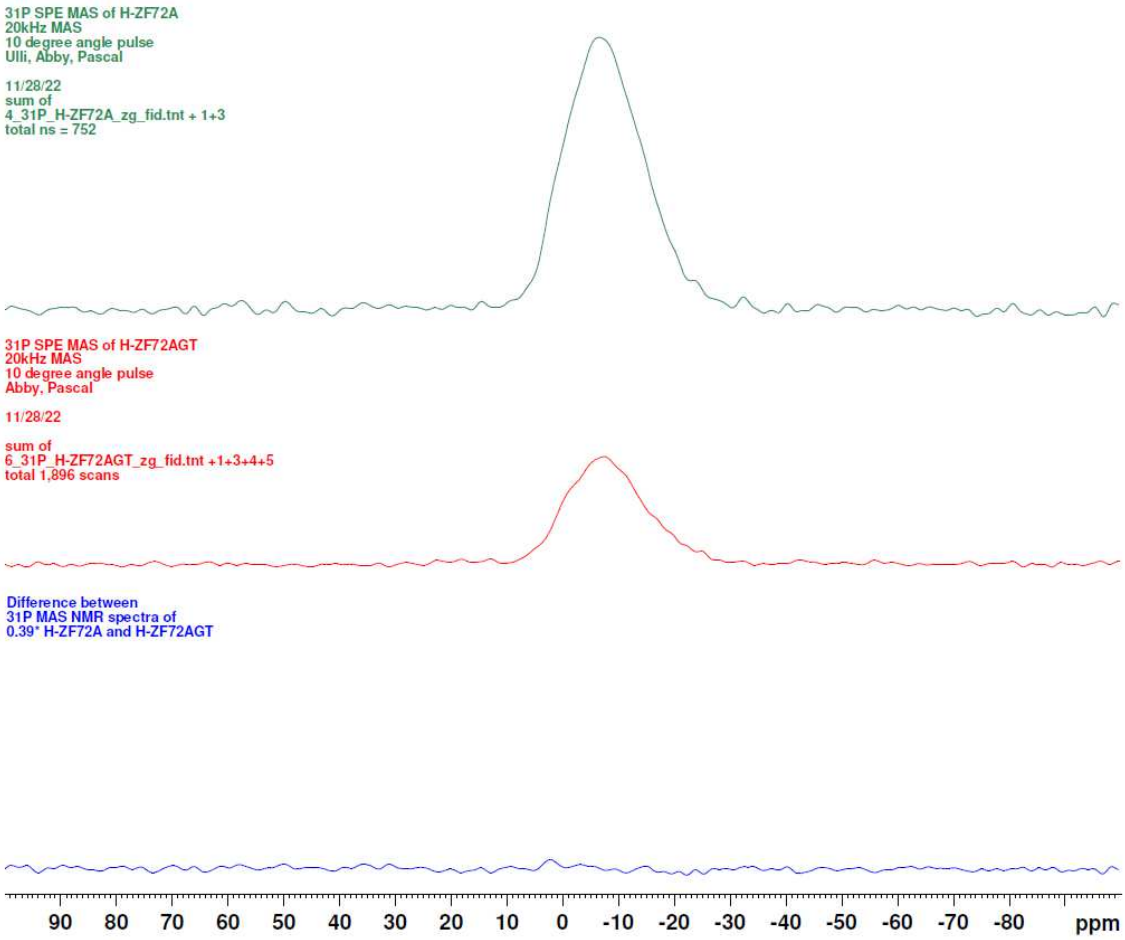

Figure A.3: ^{31}P MAS-NMR spectra of CDGM H-ZF samples showing spectral intensity difference between samples

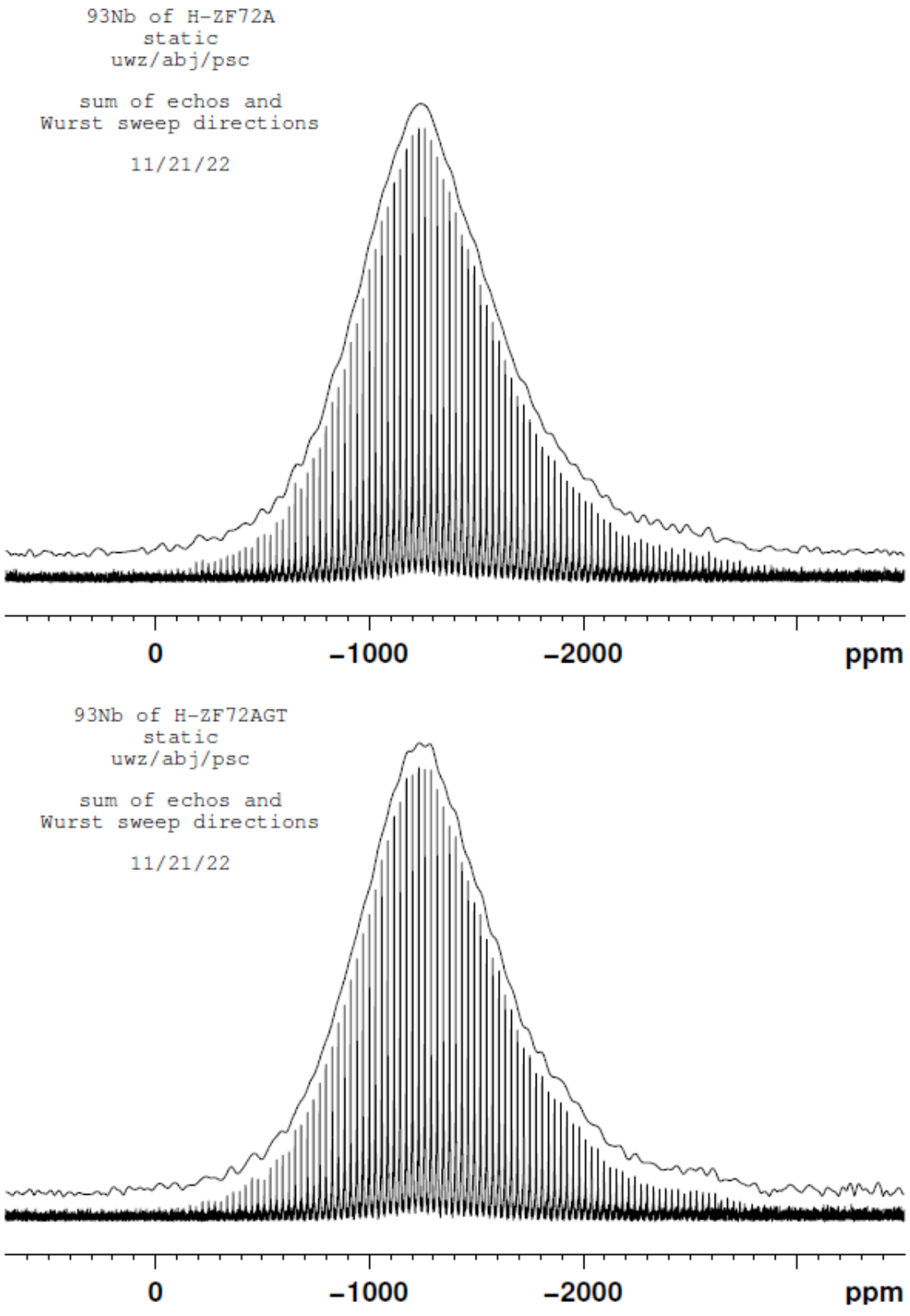

Figure A.4: ^{93}Nb WCPMG NMR spectra of CDGM H-ZF samples

Appendix B

Glass Synthesis and Acousto-Optic Results

Glass samples were synthesized by mixing stoichiometric amounts of reagents in a mortar and pestle, transferred to an alumina crucible and fired at temperatures between 1000-1500°C for up to 24 hours. The molten liquid is subsequently poured into a preheated brass mould (melt-quenching), and moved to an annealing oven to remove the internal stresses formed from nonuniform rapid cooling. A polariscope is a useful tool used to verify whether a glass has been properly annealed.

Unfortunately, the samples created in this manner were not successfully analyzed with the Dixon-Cohen setup (section 3.10) to measure their photoelastic tensor elements. As a result, bulk slabs of optical-quality commercial glasses were purchased as they were readily available and relatively economical.

Figure B.1 displays the Dixon-Cohen data recorded on a lab-synthesized PbO-P_2O_5 sample. This particular sample had minimal visible defects such as bubbles and was uniformly annealed. The data shows good transmission through the reference, yet no evidence of a back-reflected pulse from the free-end of the sample. The results through the sample substantiates the reference data, showing the initial diffracted pulse, yet no signal from the back-reflected pulse expected from the free-end of the sample. Without these particular pulses, the photoelastic tensor elements cannot be calculated. The speed of sound of this particular sample was presumed to be too low ($v_L = 3.55$ mm/μs, roughly half of v_L FQ). Perhaps the acoustic power loss through the sample is the reason for the missing diffracted pulses.

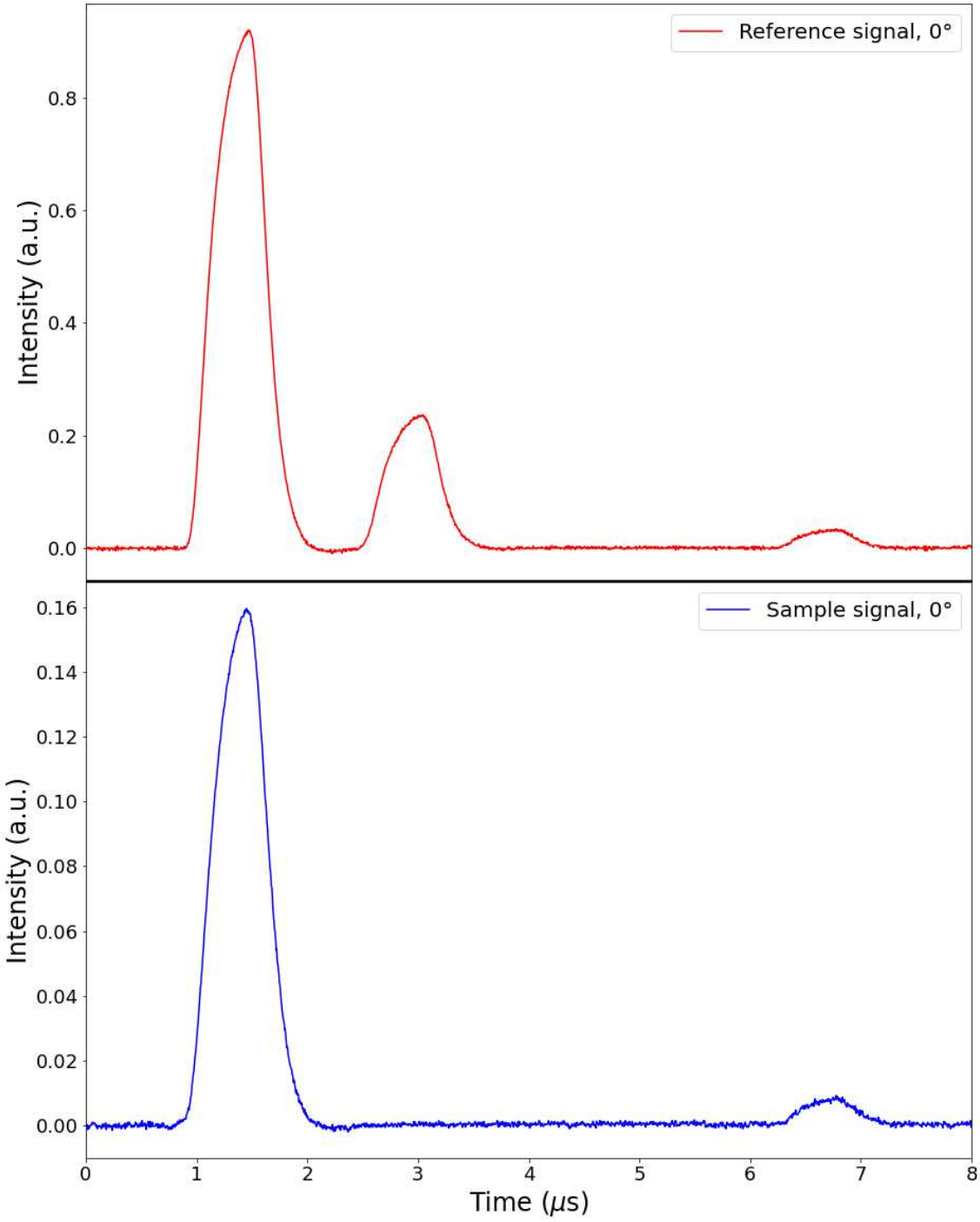

Figure B.1: DC data of a xPbO-(1-x)P_2O_5 sample through both the reference (top) and the sample (bottom)

Consequently, samples known to have higher speeds of sounds were synthesized. The attempted optical-quality samples were 50Na_2O-50P_2O_5, 20Na_2O-20B_2O_3-60SiO_2,

$20Na_2O$-$60B_2O_3$-$20SiO_2$ and $3BaO$-$3B_2O_3$-$2SiO_2$. There were several reasons these glasses did not meet the requirements for a high-quality glass.

- Fragility of samples caused them to crack immediately after synthesis
- Hydroscopic behaviour made some samples problematic during preparation
- Samples required too high melting temperatures and were too viscous when pouring into the mould resulting in globs and lots of bubbles in the sample
- Corrosive for the alumina crucibles causing significant sample contamination
- Mix of crystalline and glass phases in certain samples
- Failure to anneal uniformly

Industrial glasses are made on a much larger scale than what is capable of being synthesized in the lab.

Appendix C

Determination of p_{ij} Uncertainty

Error propagation was executed assuming the fused quartz variables of n_{FQ}, ρ_{FQ} and $v_{a,\mathrm{FQ}}$ have a negligible amount of uncertainty.

$$\delta p_{ij\mathrm{samp1}} = p_{ij\mathrm{samp1}}\sqrt{\left(\frac{1}{2}\frac{\delta\Im_{\mathrm{FQ}}}{\Im_{\mathrm{FQ}}}\right)^2 + \left(\frac{1}{2}\frac{\delta\Im_{\mathrm{samp}}}{\Im_{\mathrm{samp}}}\right)^2 + \left(\frac{1}{4}\frac{\delta I_1}{I_1}\right)^2 + \left(\frac{1}{4}\frac{\delta I_R}{I_R}\right)^2 + \\ \ldots \left(\frac{1}{4}\frac{\delta I_4}{I_4}\right)^2 + \left(\frac{1}{4}\frac{\delta I_5}{I_5}\right)^2 + \left(\frac{\delta p_{ij\mathrm{FQ}}}{p_{ij\mathrm{FQ}}}\right)^2 + \left(\frac{1}{2}\frac{\delta\rho_{\mathrm{samp}}}{\rho_{\mathrm{samp}}}\right)^2 + \left(\frac{3}{2}\frac{\delta v_{a,\mathrm{samp}}}{v_{a,\mathrm{samp}}}\right)^2 + \left(3\frac{\delta n_{\mathrm{samp}}}{n_{\mathrm{samp}}}\right)^2} \tag{C.1}$$

$$\delta p_{ij\mathrm{samp}} = \sqrt{(\delta p_{ij\mathrm{samp1}})^2 + (\delta p_{ij\mathrm{samp2}})^2 + (\delta p_{ij\mathrm{samp3}})^2 + (\delta p_{ij\mathrm{samp4}})^2 + (\delta p_{ij\mathrm{samp5}})^2} \tag{C.2}$$

The uncertainties of the unperturbed beam intensities $\Im_{\mathrm{FQ}}$ and $\Im_{\mathrm{samp}}$ were estimated using the ThorLabs power meter. The uncertainties of the recorded pulses through the reference and sample I_1, I_R, I_4 and I_5 were estimated using a python script that calculates the local maxima of data above a certain threshold. Most of the uncertainty for these particular H-ZF samples come from the I_R pulse since its intensity is so low compared to I_1. The script normally calculates a number of possible maxima for I_R, so using those values, the mean and standard deviation were calculated. An example of this can be seen in Figure C.1, where the mean and standard deviation for I_R (highlighted in green) is 0.0199 $\pm$ 0.0006. The uncertainty of $p_{ij\mathrm{FQ}}$ was determined from calculating the standard deviation of the slope from the Biegelsen and Zesch paper [4] that measured the dispersion of p_{ij} of fused quartz. The uncertainties of

ρ_{samp}, $v_{a,\text{samp}}$ and n_{samp} were determined using the method described in Sections 4.1 and 4.2.

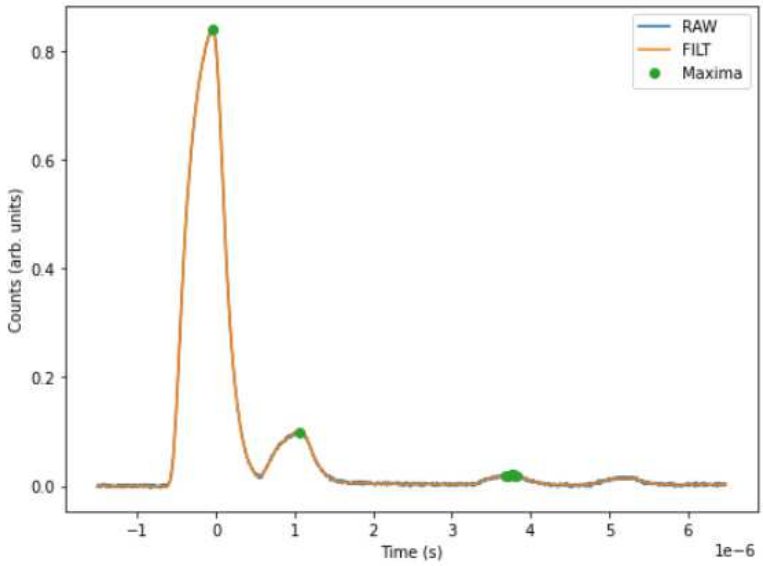

	TIME	CH1_FILT
365	-5.200000e-08	0.840907
642	1.056000e-06	0.099245
1298	3.680000e-06	0.018761
1310	3.728000e-06	0.019632
1320	3.768000e-06	0.020348
1325	3.788000e-06	0.020394
1329	3.804000e-06	0.020157
1333	3.820000e-06	0.019964

Figure C.1: Python script calculating the local maxima of a signal through the reference

The experiment was measured 5 times for each p_{11} and p_{12} for each laser wavelength. The uncertainty of p_{ij} for each trial was calculated using Equation C.1 and the final uncertainty of p_{ij} at a particular wavelength was calculated using Equation C.2.

Error propagation ensures the experimental uncertainties of all relevant components of Equation 4.5 are included in the overall uncertainty of p_{ij}. For this reason, using standard deviation may be an underestimate of the overall experimental uncertainty involved in the determination of p_{ij} and will therefore not be used.

Appendix D

CDGM Acousto-Optic Data Tables

The following tables are compiled of the average unperturbed optical beam intensities through the reference I_{ref} and through the sample I_{samp}, as well as the diffracted beam intensities through the reference I_1, I_R and through the sample I_4, I_5 at 0° and 90° polarizations and various wavelengths.

Table D.1: Average transmitted intensities through the reference and sample and diffracted beam intensities through the reference and the sample at polarizations P=0°, 90° of the **H-BaK1** sample

λ (nm)	P	I_{ref}	I_1	I_R	I_{samp}	I_4	I_5
405	0°	0.73(1)	0.259(6)	0.048(2)	0.57(2)	0.141(5)	0.070(3)
	90°	0.72(1)	0.078(2)	0.014(1)	0.57(2)	0.059(2)	0.031(2)
440	0°	1.94(5)	0.94(2)	0.16(1)	1.72(6)	0.56(5)	0.27(2)
	90°	1.89(2)	0.267(4)	0.045(2)	1.71(8)	0.22(1)	0.109(6)
543	0°	0.382(8)	0.27(1)	0.041(2)	0.34(1)	0.163(6)	0.076(5)
	90°	0.53(1)	0.125(4)	0.0183(5)	0.469(9)	0.112(3)	0.047(2)
594	0°	1.24(3)	0.88(3)	0.137(7)	1.10(5)	0.52(2)	0.25(2)
	90°	1.67(5)	0.40(2)	0.060(3)	1.43(4)	0.32(2)	0.16(1)
670	0°	1.49(4)	0.95(1)	0.16(1)	1.32(1)	0.54(1)	0.27(1)
	90°	1.49(2)	0.267(8)	0.046(2)	1.18(3)	0.188(7)	0.094(4)
785	0°	5.1(5)	3.6(2)	0.53(5)	5.3(2)	2.32(9)	1.11(2)
	90°	5.82(5)	0.93(2)	0.155(8)	5.1(2)	0.86(1)	0.42(2)
850	0°	5.4(4)	3.4(3)	0.51(5)	6.1(3)	2.5(1)	1.19(8)
	90°	5.4(2)	0.74(6)	0.12(1)	6.1(2)	0.86(7)	0.43(3)

Table D.2: Average transmitted intensities through the reference and sample and diffracted beam intensities through the reference and the sample at polarizations P=0°, 90° of the **H-BaK3** sample

λ (nm)	P	I_{ref}	I_1	I_R	I_{samp}	I_4	I_5
405	0°	0.63(4)	0.23(2)	0.031(2)	0.58(9)	0.11(2)	0.051(8)
	90°	0.62(4)	0.063(6)	0.0082(4)	0.60(4)	0.037(4)	0.0180(8)
440	0°	1.8(1)	0.90(6)	0.106(9)	1.94(4)	0.48(3)	0.19(1)
	90°	1.7(1)	0.23(2)	0.028(3)	1.85(6)	0.16(1)	0.066(3)
543	0°	0.37(2)	0.26(2)	0.029(1)	0.38(1)	0.13(1)	0.054(4)
	90°	0.51(3)	0.114(7)	0.0119(2)	0.50(1)	0.072(5)	0.029(3)
594	0°	1.13(5)	0.82(4)	0.092(1)	1.17(3)	0.42(2)	0.168(4)
	90°	1.48(7)	0.34(1)	0.036(2)	1.56(4)	0.22(2)	0.089(8)
670	0°	1.40(6)	0.92(3)	0.106(5)	1.36(5)	0.42(4)	0.181(7)
	90°	1.45(6)	0.25(2)	0.030(1)	1.27(6)	0.13(1)	0.057(3)
785	0°	5.4(4)	3.7(2)	0.39(2)	5.5(2)	1.7(1)	0.68(4)
	90°	5.3(2)	0.89(4)	0.104(5)	5.2(2)	0.56(6)	0.23(1)
850	0°	5.6(4)	3.7(1)	0.39(3)	6.1(4)	1.8(2)	0.72(6)
	90°	5.59(7)	0.70(1)	0.088(4)	6.2(2)	0.54(6)	0.25(1)

Table D.3: Average transmitted intensities through the reference and sample and diffracted beam intensities through the reference and the sample at polarizations P=0°, 90° of the **H-BaK8** sample

λ (nm)	P	I_{ref}	I_1	I_R	I_{samp}	I_4	I_5
405	0°	0.656(4)	0.238(7)	0.032(3)	0.51(7)	0.12(2)	0.052(9)
	90°	0.63(2)	0.067(2)	0.0092(5)	0.51(8)	0.047(5)	0.022(4)
440	0°	1.92(3)	0.95(3)	0.119(6)	1.88(2)	0.60(4)	0.24(1)
	90°	1.86(2)	0.26(1)	0.034(2)	1.78(4)	0.23(1)	0.092(5)
543	0°	0.38(1)	0.26(1)	0.029(2)	0.36(1)	0.158(7)	0.061(3)
	90°	0.54(2)	0.125(5)	0.014(1)	0.51(2)	0.11(1)	0.040(2)
594	0°	1.24(3)	0.89(2)	0.100(3)	1.17(4)	0.52(4)	0.20(2)
	90°	1.69(3)	0.369(9)	0.044(3)	1.35(4)	0.51(4)	0.21(2)
670	0°	1.50(2)	0.96(2)	0.113(7)	1.35(4)	0.51(4)	0.21(2)
	90°	1.48(4)	0.27(1)	0.0335(7)	1.30(6)	0.20(2)	0.08(1)
785	0°	5.6(1)	3.7(1)	0.40(2)	5.5(2)	2.1(2)	0.79(2)
	90°	5.7(2)	0.96(6)	0.12(1)	5.3(2)	0.85(6)	0.32(2)
850	0°	6.2(1)	4.0(2)	0.43(1)	6.1(1)	2.2(2)	0.91(5)
	90°	6.1(2)	0.79(2)	0.103(4)	6.2(1)	0.78(5)	0.34(2)

Table D.4: Average transmitted intensities through the reference and sample and diffracted beam intensities through the reference and the sample at polarizations P=0°, 90° of the **H-BaF2** sample

λ (nm)	P	I_{ref}	I_1	I_R	I_{samp}	I_4	I_5
405	0°	0.722(9)	0.263(6)	0.061(3)	0.62(4)	0.144(8)	0.081(8)
	90°	0.71(2)	0.071(3)	0.0165(7)	0.62(2)	0.051(1)	0.030(2)
440	0°	2.01(4)	0.97(3)	0.20(1)	1.84(4)	0.57(2)	0.30(1)
	90°	1.94(4)	0.26(1)	0.053(2)	1.84(3)	0.203(7)	0.109(6)
543	0°	0.389(5)	0.264(4)	0.049(3)	0.35(1)	0.160(7)	0.07(1)
	90°	0.54(1)	0.122(4)	0.0224(5)	0.503(6)	0.099(7)	0.049(3)
594	0°	1.28(3)	0.90(2)	0.162(9)	1.186(8)	0.541(8)	0.269(6)
	90°	1.66(4)	0.38(1)	0.070(2)	1.49(4)	0.31(1)	0.150(5)
670	0°	1.49(6)	0.94(5)	0.18(1)	1.38(7)	0.53(5)	0.29(3)
	90°	1.46(3)	0.27(1)	0.056(1)	1.24(8)	0.18(8)	0.09(1)
785	0°	5.7(3)	3.9(2)	0.69(4)	5.3(2)	2.2(1)	1.1(1)
	90°	5.60(8)	0.97(3)	0.20(1)	5.3(2)	0.78(7)	0.43(3)
850	0°	6.1(2)	3.9(2)	0.72(6)	5.9(3)	2.2(2)	1.1(1)
	90°	6.2(2)	0.77(7)	0.16(2)	6.2(3)	0.72(7)	0.42(5)

Table D.5: Average transmitted intensities through the reference and sample and diffracted beam intensities through the reference and the sample at polarizations P=0°, 90° of the **H-ZF72A** sample

λ (nm)	P	I_{ref}	I_1	I_R	I_{samp}	I_4	I_5
405	0°	0.66(3)	0.25(2)	0.0033(2)	0.24(1)	0.029(4)	0.003(1)
	90°	0.687(8)	0.073(4)	0.0012(2)	0.24(1)	0.007(1)	0.0008(4)
440	0°	2.12(6)	1.06(3)	0.014(2)	1.70(4)	0.34(7)	0.035(6)
	90°	2.07(6)	0.28(1)	0.0038(3)	1.72(3)	0.09(2)	0.010(2)
543	0°	0.42(2)	0.30(2)	0.0037(5)	0.39(2)	0.11(2)	0.013(3)
	90°	0.574(3)	0.135(3)	0.0016(3)	0.51(1)	0.053(9)	0.006(1)
594	0°	1.31(5)	0.93(2)	0.011(1)	1.24(4)	0.38(8)	0.04(1)
	90°	1.75(3)	0.425(8)	0.0051(5)	1.61(6)	0.18(5)	0.021(5)
670	0°	1.61(2)	1.05(2)	0.0133(7)	1.5(2)	0.38(7)	0.05(1)
	90°	1.63(3)	0.293(2)	0.0044(5)	1.50(4)	0.12(2)	0.015(3)
785	0°	5.8(1)	3.8(1)	0.049(3)	5.7(3)	1.6(3)	0.18(4)
	90°	5.9(2)	0.95(3)	0.014(2)	5.4(1)	0.5(1)	0.05(1)
850	0°	6.3(5)	3.8(3)	0.052(6)	6.1(6)	1.4(3)	0.20(3)
	90°	6.5(1)	1.02(9)	0.017(2)	6.3(4)	0.5(1)	0.07(1)

Table D.6: Average transmitted intensities through the reference and sample and diffracted beam intensities through the reference and the sample at polarizations P=0°, 90° of the **H-ZF72AGT** sample

λ (nm)	P	I_{ref}	I_1	I_R	I_{samp}	I_4	I_5
405	0°	0.68(1)	0.247(5)	0.0059(3)	0.157(6)	0.027(4)	0.004(1)
	90°	0.69(1)	0.069(2)	0.0019(3)	0.158(1)	0.0045(1)	0.0009(6)
440	0°	2.0(1)	1.00(3)	0.0209(6)	1.29(2)	0.27(5)	0.035(7)
	90°	2.04(2)	0.254(6)	0.0053(4)	1.23(4)	0.07(1)	0.009(2)
543	0°	0.42(2)	0.30(1)	0.0057(6)	0.37(1)	0.11(2)	0.016(3)
	90°	0.58(2)	0.126(4)	0.0023(3)	0.52(2)	0.05(1)	0.007(1)
594	0°	1.24(6)	0.91(4)	0.0173(8)	1.15(7)	0.38(8)	0.052(7)
	90°	1.70(4)	0.381(3)	0.0068(4)	1.56(7)	0.17(3)	0.024(4)
670	0°	1.54(3)	1.01(6)	0.019(1)	1.47(6)	0.40(6)	0.07(2)
	90°	1.52(1)	0.24(1)	0.0050(5)	1.39(6)	0.12(3)	0.017(2)
785	0°	5.81(5)	4.0(1)	0.074(5)	5.9(3)	1.5(1)	0.29(6)
	90°	5.5(2)	0.87(7)	0.018(2)	5.3(4)	0.39(5)	0.08(2)
850	0°	6.3(3)	4.0(1)	0.079(4)	6.3(6)	1.8(4)	0.26(6)
	90°	6.3(2)	0.80(4)	0.018(1)	5.9(8)	0.5(1)	0.07(2)